Master thesis and internship[BR]- Master's thesis : STUDY OF AN ADVANCED TANDEM BLADE DESIGN FOR INCREASING THE OPERATING RANGE OF A LOW PRESSURE COMPRESSOR[BR]- Integration internship

Auteur : Anton Dobarro, David
Promoteur(s) : Hillewaert, Koen
Faculté : Faculté des Sciences appliquées
Diplôme : Cours supplémentaires destinés aux étudiants d'échange (Erasmus, ...)
Année académique : 2024-2025
URI/URL : http://hdl.handle.net/2268.2/22986

STUDY OF AN ADVANCED TANDEM BLADE DESIGN FOR INCREASING THE OPERATING RANGE OF A LOW PRESSURE COMPRESSOR

Master's thesis presented to obtain the degree of Master of Science in Aerospace Engineering
by David Anton Dobarro

Thesis supervisors

Koen Hillewaert
Universtiy of Liège

Andrea Rocca
Cenaero

University of Liège - School of Engineering and Computer Science

Academic year 2024-2025

Abstract

In the pursuit of improving the performance of axial compressors, the present work will study several options for adjusting the final compressor stage, the Outlet Guide Vane (OGV), to varying compressor operating conditions. More specifically, the blades of the OGV, which will use a tandem configuration, shall be optimized so that the performance of the OGV is improved.

Two different strategies will be considered for the optimization. On the one hand, the working range of the OGV will be maximized while keeping the losses at a reference inlet flow angle of 50º within a certain range. On the other hand, the on-design losses shall be minimized while keeping the off-design losses within a certain margin.

The key parameters that will be used to define different configurations in this project will be the relative position of the blades and their respective geometries. The performance of the obtained geometries shall be simulated across different inlet flow angles.

The meshes developed in this work shall be created using the Gmsh software package. Numerical simulations shall be performed using a RANS model with the SU2 software. Finally, the results will be post-processed and further studied using the Paraview software.

The present work is a tool intended to be coupled with the work done by Mathias Brach, and currently continued by Thibaut Dupont, who focused on optimizing the performance of the OGV for different inlet flow angles by using a variable guide vane.

Their work focused on rotating the front blade (FB) of the OGV using certain rotation points to maximize the performance of the tandem blades at different inlet flow angles. However, their work won't be implemented on this project.

The results of this work have shown that by having an axial overlap (AO) about 2% and a percentage pitch (PP) about 93%, as well as an optimized geometry that allows a sharp turning of the flow, can significantly reduce the pressure losses across the tandem stage while maintaining an axial exit flow and an acceptable working range.

Additionally, increasing the axial gap between the blades and reducing the percentage pitch to 85 - 90% has successfully increased the working range, and more specifically, the upper bound of the working range. However, increasing the working range significantly has caused a substantial increment of the pressure losses and an impossibility to keep the exit flow as axial as possible.

The target outcome of this project is to serve as a starting point for the design of future OGVs.

Abstrait

Dans la poursuite de l'amélioration des performances des compresseurs axiaux, le présent travail étudiera plusieurs options pour ajuster le dernier étage du compresseur, l'aube directrice de sortie (OGV), aux différentes conditions de fonctionnement du compresseur. Plus spécifiquement, les aubes de l'OGV, qui utiliseront une configuration en tandem, seront optimisées afin d'améliorer les performances de l'OGV.

Deux stratégies différentes seront envisagées pour l'optimisation. D'une part, la plage de fonctionnement de l'OGV sera maximisée tout en maintenant les pertes à un angle d'écoulement d'entrée de référence de 50º dans une certaine plage. D'autre part, les pertes en régime nominal seront minimisées tout en maintenant les pertes hors régime nominal dans une certaine marge.

Les paramètres clés qui seront utilisés pour définir différentes configurations dans ce projet seront la position relative des aubes et leurs géométries respectives. Les performances des géométries obtenues seront simulées pour différents angles d'écoulement d'entrée.

Les maillages développés dans ce travail seront créés à l'aide du progiciel Gmsh. Les simulations numériques seront effectuées à l'aide d'un modèle RANS avec le logiciel SU2. Enfin, les résultats seront post-traités et étudiés plus en détail à l'aide du logiciel Paraview.

Le présent travail est un outil destiné à être couplé avec le travail réalisé par Mathias Brach, et actuellement poursuivi par Thibaut Dupont, qui s'est concentré sur l'optimisation des performances de l'OGV pour différents angles d'écoulement d'entrée en utilisant une aube directrice variable.

Leur travail s'est concentré sur la rotation de l'aube avant (FB) de l'OGV en utilisant certains points de rotation pour maximiser les performances des aubes en tandem à différents angles d'écoulement d'entrée. Cependant, leur travail ne sera pas mis en œuvre dans ce projet.

Les résultats de ce travail ont montré qu'un chevauchement axial (AO) d'environ 2 % et un pas relatif (PP) d'environ 93 %, ainsi qu'une géométrie optimisée permettant un virage prononcé de l'écoulement, peuvent réduire considérablement les pertes de pression à travers l'étage en tandem tout en maintenant un écoulement de sortie axial et une plage de fonctionnement acceptable.

De plus, l'augmentation de l'espace axial entre les aubes et la réduction du pas relatif à 85 - 90 % ont permis d'augmenter la plage de fonctionnement, et plus spécifiquement, la limite supérieure de la plage de fonctionnement. Cependant, l'augmentation significative de la plage de fonctionnement a entraîné une augmentation substantielle des pertes de pression et une impossibilité de maintenir l'écoulement de sortie aussi axial que possible.

Le résultat visé de ce projet est de servir de point de départ pour la conception de futurs OGV.

Acknowledgements

Special thanks to the whole Cenaero team who has aided me during my stage at Cenaero and particularly to Andrea Rocca, my supervisor at Cenaero, without whom this work would not have been possible.

I would also like to thank Professor Koen Hillewaert from the ULiège who has been the supervisor of this thesis. The present work has been completed thanks to his theoretical insights on turbomachinery and his aid by checking the work done.

I would like to gratefully acknowledge the foundational work of Mathias Brach and Thibaut Dupont in variable geometry OGV optimization, which directly inspired this complementary research direction [1].

Computational resources have been provided by the Consortium des Équipements de Calcul Intensif (CÉCI), funded by the Fonds de la Recherche Scientifique de Belgique (F.R.S.-FNRS) under Grant No. 2.5020.11 and by the Walloon Region.

The present research benefited from computational resources made available on Lucia, the Tier-1 supercomputer of the Walloon Region, whose infrastructure was funded by the Walloon Region under the grant agreement n°1910247.

Contents

Index of Figures

List of Tables

1 Introduction

One of the most carbon-intensive activities is air travel, which currently accounts for almost 3% of the world's carbon emissions. However, as global demand increases and the industry expands, such emissions shall increase in the following years if no measures are taken into account.

As the world is growing more aware of the importance of global warming, the aerospace sector has recognized its part in addressing environmental damage. Hence, the industry has acknowledged the need to implement sustainable practices for long-term viability [2] [3].

The following project shall study one of the ways to improve the operational efficiency of aircraft to minimize fuel consumption. Thus enhancing its reliability, efficiency and the overall performance of air flight.

In the present section an overview of the goals, reasons and methodology for the development of this work shall be provided.

1.1 Aim

The aim of this thesis is to investigate and optimize the tandem blade configuration for the Outlet Guide Vane (OGV) of a low-pressure compressor, in order to improve its operational efficiency, aerodynamic performance, and adaptability to varying inlet conditions. By conducting Computational Fluid Dynamics (CFD) simulations, this research seeks to analyze the impact of different blade geometries and positioning strategies on key performance indicators such as pressure loss reduction, flow stabilization, and incidence angle adaptability. Ultimately, the findings of this study will contribute to advancing compressor technology by expanding the operating range and enhancing aerodynamic efficiency, thus supporting the broader goal of sustainable aviation and fuel efficiency improvement.

1.2 Justification

As mentioned previously, in the last years the aerospace industry has been working on enhancing its efficiency and sustainability due to its environmental impact and to the increment of public and regulatory demand for more sustainable practices.

Aviation is one of the most carbon-intensive industries, which currently contributes to about 2-3% of global CO_2 emissions. With passenger numbers and air freight demand tending to rise, emissions would do so as well if left unaddressed. Most aircraft are powered by fossil fuels, meaning that each flight emits a substantial amount of greenhouse gases like CO_2 or nitrogen oxides, which affect global warming. Sustainable aviation is critical to reduce emissions in line with global climate goals, such as those set by the Paris Agreement, which aims to keep global warming below 2 ºC [4].

The industry is proposing various initiatives which aim to enhance the sustainability, including:

- Development of eco-friendly aviation technologies.
- Implementation of green manufacturing processes.
- Strategies for carbon footprint reduction.
- Improvements in energy efficiency and adoption of responsible supply chains.

One of the most effective strategies to reduce aviation emissions is improving fuel efficiency. Key contributors to fuel consumption include engine performance and aerodynamics. Thus, compressors play a critical role in overall propulsion efficiency. In particular, optimizing the design of the Low-Pressure Compressor (LPC) stages can significantly enhance engine performance by reducing pressure losses, improving aerodynamic stability, and extending the operating range under varying flight conditions.

A promising approach for increasing LPC efficiency is the implementation of tandem blade designs. Recent research has demonstrated that tandem blade configurations offer significant advantages over conventional single-blade designs, particularly in highly loaded axial compressors. By using two staggered blades within a single stage, tandem blades can improve aerodynamic performance by reducing losses, increasing flow turning capability, and mitigating boundary layer separation. Studies have shown that tandem configurations allow for a higher blade loading while maintaining stable operation and reduced flow separation, which makes them particularly well-suited for applications where performance across a wide range of operating conditions is required.

In the case of OGVs, which are crucial for redirecting the compressor's airflow and ensuring optimized pressure recovery, a tandem blade design can help expand the operational range of incidence angles. Traditional single-blade OGVs often suffer from efficiency losses when handling variable inlet conditions, whereas tandem configurations provide greater adaptability to changing flow angles, reducing pressure losses and enhancing compressor stability.

Furthermore, experimental and numerical studies have confirmed that tandem blades increase the maximum loading limit of axial compressors, leading to enhanced performance margins and improved stall resistance. The ability to sustain higher flow deflection with reduced aerodynamic penalties makes tandem blades a promising solution for next-generation turbomachinery [1] [5] [6] [7] [8].

By optimizing the OGV geometry in a tandem configuration, it is possible to:

- Expand the range of incidence angles, therefore reducing the sensitivity to off-design conditions.
- Increase the load that the blades can sustain, hence reducing the number of blades.

- Minimize pressure losses, thereby improving compressor performance and reducing energy consumption.
- Enhance aerodynamic stability, leading to lower mechanical stress and increased engine lifespan.

Given these advantages, this research focuses on analyzing and optimizing a tandem OGV configuration to achieve higher aerodynamic efficiency, reduced pressure losses, and an increased operating range. By leveraging CFD simulations, the study will explore different blade geometries and positioning strategies to determine an optimal design that enhances both efficiency and adaptability.

The outcomes of this research are expected to contribute to the broader goal of sustainable aviation, providing insights that can be applied to future high-performance compressor designs while aligning with the industry's push for fuel efficiency and reduced carbon emissions.

1.3 Methodology

The present study shall aim to investigate the optimization of a static tandem blade configuration for the OGV of a low-pressure compressor stage. To accomplish this goal, the work is divided into the following steps.

Initially, the study focuses on a static tandem configuration of the OGV. This baseline configuration is designed to accommodate an inlet flow angle of 50°, meaning that other flow angles would be off-design configurations.

The numerical study is conducted using the following software tools:

- Gmsh for generating structured and unstructured computational grids.
- SU2 as the CFD solver, utilizing a Reynolds-Averaged Navier-Stokes (RANS) approach to model the aerodynamic behavior of the compressor stage.
- ParaView for post-processing and visualization of simulation results.
- Python for additional scripting, automation, and data analysis.

The first study improves the initial mesh quality to ensure a more accurate aerodynamic analysis. Enhancing the computational grid allows for better resolution of key flow features and provides a robust foundation for subsequent investigations.

The next phase of the study systematically explores the effect of two strategies on the OGV's performance of different inlet incidence angles (on-design and off-design). On the one hand, the position of the front blade is translated to change the relative position of the tandem blades. On the other hand, the shape of both blades is modified.

The final step of the study is divided into the optimization of the OGV following two approaches:

- On-design performance optimization, where the on-design pressure loss is minimized, while keeping the off-design pressure losses within an acceptable range when compared to the baseline configuration.
- Working range optimization, where the working range (range where the pressure losses are within 2-3 times those of the on-design configuration) is maximized, while keeping the on-design pressure loss within an acceptable range when compared to the baseline configuration.

To perform the optimizations, a combined approach of blade translation and blade shape modification is used.

2 Turbomachinery and Turbofan Engine Fundamentals

The analysis carried out in this section shall provide a general overview of the fundamental principles and components of aircraft engines. The general structure and operation of turbofan engines, which are commonly used in commercial aviation, will be examined. This will include a detailed look at the various stages and components involved in the engine's operation, as illustrated in Figures 1 and 2. Following this general overview, the study will delve into more specialized topics relevant to the specific focus of this thesis.

2.1 Turbofan

Most commercial aircraft use turbofan engines due to their high efficiency and thrust capabilities. A turbofan engine operates on the principle of converting chemical energy from fuel into kinetic energy to propel the aircraft. The engine consists of several stages that play a role in the propulsion process. The cross-section of a typical turbofan engine is shown in Figure 1, while Figure 2 provides a simplified schematic of the processes and their interactions within the engine [9].

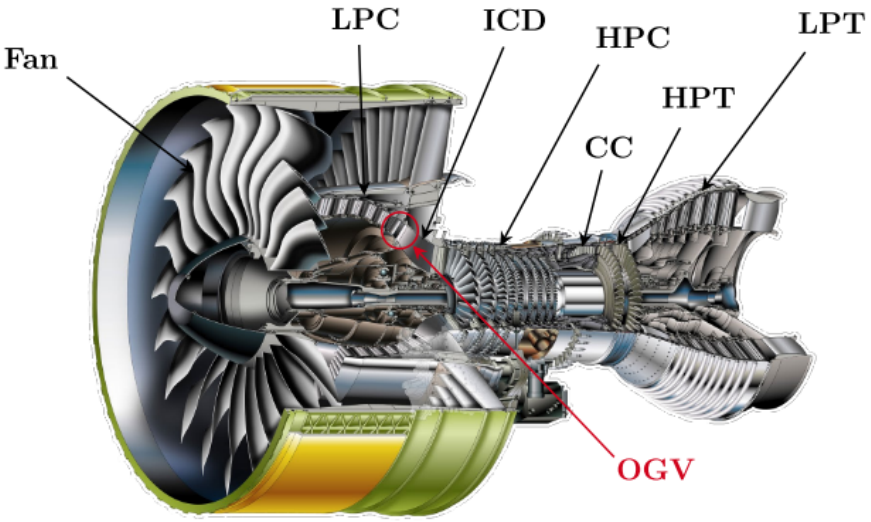

Figure 1. Turbofan engine cross-section. Source: [1]

The turbofan engine operates as follows:

1. Air is drawn into the engine through the air intake and accelerated by the fan.
2. The air on the outlet of the fan is divided into the main (core) and secondary (bypass) flows.
3. Core stream:

(a) The core air is compressed in multiple stages by the low-pressure and high-pressure compressors.

(b) The compressed air is mixed with fuel and ignited in the combustion chamber, producing high-energy gas.

(c) The high-energy gas expands through the turbines, driving the compressors and the fan.

(d) The exhaust gases exit the engine through the nozzle, producing thrust.

4. Bypass stream:

(a) The secondary flow is expanded in a secondary nozzle.

(b) The secondary flow generates most of the thrust of the turbofan.

The work cycle described previously allows turbofan engines to generate the thrust required for aircraft propulsion. Furthermore, the bypass air, which flows around the core, contributes significantly to the engine's efficiency and noise reduction, making turbofan engines the preferred choice for modern commercial aviation [10].

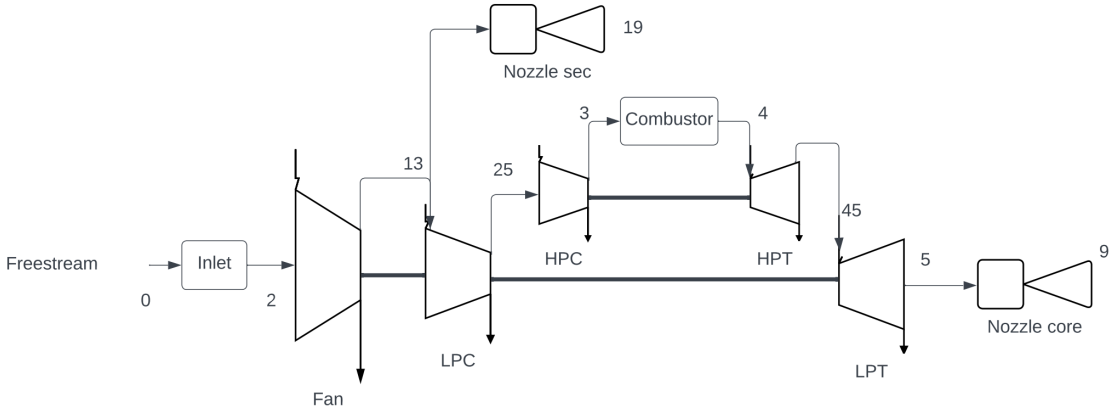

Figure 2. Turbofan engine scheme

2.1.1 Air Intake and Fan

The propulsion process begins with the intake of ambient air into the engine through the air intake. The air is then accelerated by the fan, which is the first rotating component of the engine. The fan is typically a large-diameter rotor with multiple blades that compress and accelerate the incoming air. A portion of this air, known as the bypass air, flows around the core of the engine, while the remaining air, called the core air, enters the engine's core for further compression and combustion. The ratio between the core and bypass flows is called the bypass ratio. By increasing the bypass ratio, the engine mass flow is significantly increased. Thus, the thrust is obtained by a

lower acceleration of the air passing through the engine. Therefore, a higher propulsive efficiency is achieved. The bypass air contributes significantly to the engine's thrust and efficiency, making turbofan engines particularly suitable for subsonic and transonic flight.

2.1.2 Compressor

The core air enters the compressor section, which consists of multiple stages of rotating and stationary blades. Each stage of the compressor further increases the pressure of the air. The compressor is typically divided in two sections: the low-pressure compressor (LPC) and the high-pressure compressor (HPC). The LPC compresses the air to an intermediate pressure, while the HPC further compresses it to a high pressure before it enters the combustion chamber. The compression process is essential for increasing the air's density and temperature, which enhances the efficiency of the combustion process. It is important to note, however, that as the number of compression stages increases, the pressure rise is greater, but the complexity and the cost of the engine arise, too.

2.1.3 Combustion Chamber

The high-pressure air from the compressor enters the combustion chamber, where it is mixed with fuel and ignited. The combustion process releases a large amount of thermal energy, significantly increasing the temperature and pressure of the air. This high-energy gas then expands and flows toward the turbine section. The combustion chamber is designed to ensure stable and efficient combustion while withstanding the extreme temperatures and pressures generated during the process.

2.1.4 Turbine

The high-energy gas from the combustion chamber flows into the turbine section, which consists of multiple stages of rotating and stationary blades. The turbines extract energy from the gas and convert it into mechanical power to drive the compressor and the fan. The turbine section is typically divided into two parts: the high-pressure turbine (HPT) and the low-pressure turbine (LPT). The HPT drives the high-pressure compressor, while the LPT drives the low-pressure compressor and the fan. The work produced by the turbines ensures that the compression and fan processes are sustained, creating a continuous cycle of air intake, compression, combustion, and expansion. Note that the capability of the turbine blades to withstand extreme temperatures is an important requirement.

2.1.5 Nozzle

After passing through the turbines, the exhaust gases exit the engine through the nozzle. The nozzle is designed to accelerate the exhaust gases to produce thrust. In subsonic engines, the nozzle is typically convergent, which accelerates the gases to subsonic speeds. In supersonic engines, a convergent-divergent nozzle is used to further accelerate the gases to supersonic speeds. The nozzle's design plays a critical role in optimizing the engine's thrust and efficiency.

2.1.6 Bypass Stream and Exhaust

The bypass stream that flows around the core of the engine is expanded through a nozzle too. When considering the mixing of the core and bypass streams, two configurations arise:

- Separate exhausts: In this case, the exhausts of the core and bypass streams are separated. The flows mix downstream of the engine.
- Mixed exhausts: In this case, the exhausts of the core and bypass streams are mixed in the last stage of the engine before a last expansion through a nozzle. By mixing the exhausts the overall performance of the engine improves and the exhaust noise is reduced.

2.2 Compressors

The compressor is a critical component of a turbofan engine, responsible for increasing the pressure of the incoming air before it enters the combustion chamber. This process is essential for ensuring efficient combustion and optimal engine performance. The losses are minimized by resembling an isentropic process as much as possible, in other words, with the minimum required temperature ratio for a given pressure ratio. As it has been mentioned previously, the compressor is typically divided in two sections: the low-pressure compressor (LPC) and the high-pressure compressor (HPC). The LPC is the first stage of compression and plays a key role in preparing the air for further compression in the HPC.

2.2.1 Low-Pressure Compressor (LPC)

The LPC consists of multiple stages of rotating and stationary blades. Each stage is composed of a rotor (rotating blades) and a stator (stationary blades). The rotor accelerates the air, increasing its kinetic energy, while the stator converts this kinetic energy into pressure by slowing down the air. At the compressor's inlet there is the inlet guide vane, which guides the incoming flow into the first rotor stages at the desired angle. Additionally, at the compressor's outlet there is the outlet guide vane, which converts the kinetic energy into pressure and guides the airflow into the next stage with the desired angle (usually close to 0 with respect to the axial direction). The

LPC operates at lower pressures compared to the HPC and is driven by the low-pressure turbine (LPT).

2.2.2 Axial vs. Centrifugal Compressors

Compressors can be classified into two main types based on their design and airflow direction:

- Axial Compressors: In these compressors, the air flows parallel to the axis of rotation. They consist of multiple stages of rotors and stators, each contributing to a gradual increase in pressure. Axial compressors are highly efficient and are commonly used in large and medium sized turbofan engines due to their ability to handle large volumes of air with relatively low losses.
- Centrifugal Compressors: In these compressors, the air is drawn in axially but is then accelerated radially outward by a rotating impeller. The air is then diffused in a volute or diffuser to increase its pressure. Centrifugal compressors are simpler in design and are often used in smaller engines. However, they are less efficient than axial compressors for high-volume applications.

2.2.3 Euler's Turbomachinery Equation

The energy transfer in a compressor stage can be described using Euler's Turbomachinery Equation, which relates the work done by the rotor to the change in angular momentum of the air. Euler's equation is a consequence of the steady state's energy equation applied to an annular control volume enclosing the rotor inlet and outlet [1].

The energy equation for a control volume in a turbomachine is given by:

$$d\dot{Q} - d\dot{W} = d\dot{m}\left(h_{t_i}^{\circ} - h_e^{\circ}\right) \tag{1}$$

where $d\dot{Q}$ is the heat transfer rate [W], $d\dot{W}$ is the mechanical power [W], $d\dot{m}$ is the mass flow rate [kg/s], h_i° is the total enthalpy at the inlet [J/kg] and h_e° is the total enthalpy at the exit [J/kg].

For an adiabatic process (no heat transfer, $d\dot{Q} = 0$), the equation simplifies to:

$$d\dot{W} = d\dot{m}\left(h_i^{\circ} - h_e^{\circ}\right) \tag{2}$$

The mechanical power $d\dot{W}$ can also be expressed in terms of the angular momentum change of the fluid:

$$d\dot{W} = d\dot{m}\omega\left(r_e v_e - r_i v_i\right) \tag{3}$$

[1] Consider that the notation used in the following sections will follow the same nomenclature as [10].

where ω is the angular velocity of the rotor [rad/s] r_i and r_e are the radii at the inlet and exit, respectively [m] and v_i and v_e are the tangential velocities at the inlet and exit, respectively [m/s].

Combining the two expressions for mechanical power, the Euler's Turbomachinery Equation may be obtained:

$$(h_e^\circ - h_i^\circ) = \omega\,(r_e v_e - r_i v_i) \tag{4}$$

For an ideal gas, the change in enthalpy can be expressed in terms of temperature using the specific heat at constant pressure (c_p):

$$c_p\,(T_e^\circ - T_i^\circ) = \omega\,(r_e v_e - r_i v_i) \tag{5}$$

Finally, for a purely axial engine $r \simeq r_i \simeq r_e$ which would turn Euler's equation into:

$$\Delta h^\circ = c_p\,(T_e^\circ - T_i^\circ) = \omega r\,(v_e - v_i) = U(v_e - v_i) \tag{6}$$

This equation explains the relationship between the change in enthalpy (or temperature) of the fluid and the work done by the rotor. It is a fundamental equation in the design and analysis of turbomachinery, as it provides a direct link between the fluid's thermodynamic properties and the rotor's mechanical performance.

2.2.4 Velocity Triangles in Compressor Stages

The performance of a compressor stage can be analyzed using velocity triangles, which describe the relationship between the absolute, relative, and blade velocities of the air at the inlet and outlet of the rotor and stator. The velocity triangles are essential for understanding the energy transfer and flow behavior in the compressor.

- Rotor Inlet: The absolute velocity of the air (V_1) is the vector sum of the relative velocity (V_{1R}) and the blade velocity (U). The tangential component of the absolute velocity at the inlet (v_1) can be expressed as:

$$v_1 = U - v_{1R} = U - u_1 \tan\beta_1 = u_1 \tan\alpha_1 \tag{7}$$

  where u_1 is the axial velocity at the inlet (in m/s), β_1 is the relative flow angle at the inlet (in degrees) and α_1 is the absolute flow angle at the inlet (in degrees).

- Rotor Outlet: The relative velocity (V_{2R}) changes due to the work done by the rotor, and the absolute velocity (V_2) is adjusted accordingly. The tangential component of the absolute velocity at the outlet (v_2) can be expressed as:

$$v_2 = U - v_{2R} = U - u_2 \tan\beta_2 = u_2 \tan\alpha_2 \tag{8}$$

where u_2 is the axial velocity at the outlet (in m/s), β_2 is the relative flow angle at the outlet (in degrees) and α_2 is the absolute flow angle at the outlet (in degrees).

- Stator: The stator further adjusts the absolute velocity (V_3) to ensure optimal flow conditions for the next stage.

Assuming that the middle section of the compressor is considered, the previous assumptions could be represented as seen in Figure 3.

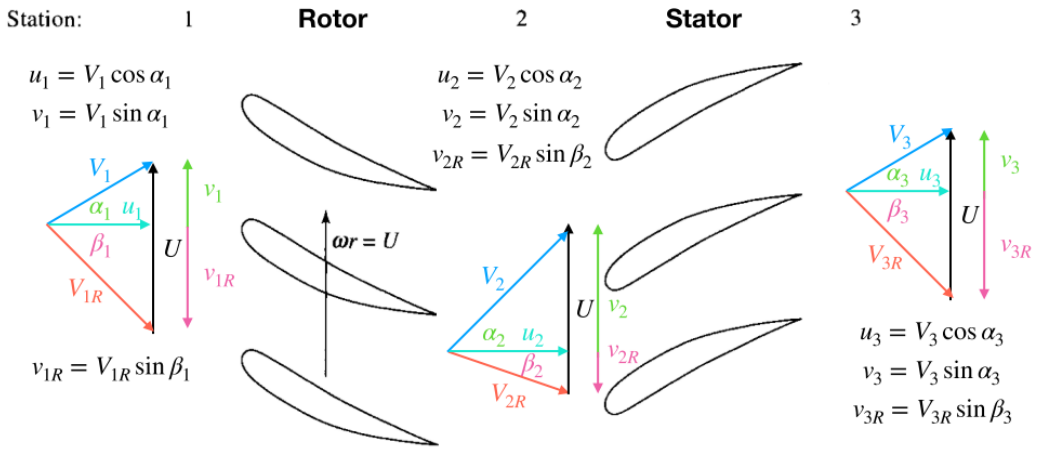

Figure 3. Velocity triangles

By recalling Euler's Equation 6:

$$\Delta h^\circ = U(v_2 - v_1) \tag{9}$$

and using Equations 7 and 8, the change in total enthalpy across the compressor stage can be expressed in terms of the flow angles:

$$\Delta h^\circ = U^2 - (u_1 \tan\beta_1 + u_2 \tan\beta_2) \tag{10}$$

2.2.5 Thermodynamic Variables Across the Compressor Stage

The evolution of thermodynamic variables at each stage is critical to comprehend the performance of the compressor. Their progression is described as:

Variable	Symbol	Rotor's Inlet	Rotor's Outlet	Stator's Outlet	Units
Static pressure	P	P_1	P_2	P_3	Pa
Static temperature	T	T_1	T_2	T_3	K
Mach number	M	M_1	M_2	M_3	-
Total pressure	P°	P_1°	P_2°	-	Pa
Total temperature	T°	T_1°	T_2°	-	K
Relative total pressure	P_R°	P_{1R}°	P_{2R}°	-	Pa
Relative total temperature	T_R°	T_{1R}°	T_{2R}°	-	K
Relative Mach number	M_R	M_{1R}	M_{2R}	-	-

Table I. Thermodynamic variables at different compressor stations

The thermodynamic variables at Station 2 can be determined using the following relationships:

- The total temperature at Station 2 (T_2°) is obtained from Euler's equation:

$$T_2^\circ = T_1^\circ + \Delta T^\circ \tag{11}$$

- The relative total pressure at Station 2 (P_{2R}°) is related to the relative total pressure at Station 1 (P_{1R}°) by the rotor recovery factor (R_{fR}):

$$P_{2R}^\circ = P_{1R}^\circ R_{fR} \tag{12}$$

  Where, assuming incompressible or low Mach number flow:

  - $R_{fR} = 1 - \phi_{cr} \frac{\gamma P_1 M_{1R}^2}{2P_{t_{1R}}}$ is the rotor's recovery factor,
  - $\phi_{cr} = \frac{P_{1R}^\circ - P_{2R}^\circ}{\rho_1 V_{1R}^2/2}$ is the pressure loss coefficient.

- The blade velocity (U) is related to the angular velocity (ω) and the radius (r):

$$U = \omega r \tag{13}$$

- The relative total temperature remains constant across the rotor ($T_{2R}^\circ = T_{1R}^\circ$) in the rotating reference frame.

- The static pressure and temperature increase across the rotor ($P_2 > P_1$ and $T_2 > T_1$).

- The relative Mach number decreases across the rotor ($M_{2R} < M_{1R}$).

The thermodynamic variables at Station 3 can be determined using the following relationships:

- The total temperature at Station 3 remains constant across the stator ($T_3^\circ = T_2^\circ$).

- The total pressure at Station 3 (P_3°) is related to the total pressure at Station 2 (P_2°) by the stator recovery factor (R_{fS}):

$$P_{2R}^\circ = P_{1R}^\circ R_{fS} \tag{14}$$

  Where, assuming incompressible or low Mach number flow:

  - $R_{fS} = 1 - \phi_{cs}\frac{\gamma P_2 M_2^2}{2P_2^\circ}$ is the stator's recovery factor.
  - $\phi_{cs} = \frac{P_2^\circ - P_3^\circ}{\rho_2 V_2^2/2}$ is the pressure loss coefficient.

- The static pressure and temperature increase across the stator ($P_3 > P_2$ and $T_3 > T_2$).

These relationships represent the conservation of energy and the changes in thermodynamic properties across the compressor stage. It may be appreciated that the static pressures and temperatures increase along the compressor's stages.

2.2.6 Efficiencies

The performance of a compressor stage is characterized by several key parameters, including the stage pressure ratio, isentropic efficiency, polytropic efficiency and the degree of reaction. These parameters provide insights into the thermodynamic and aerodynamic performance of the compressor.

The stage pressure ratio (π_{c_s}) is defined as the ratio of the total pressure at the outlet of the stage (P_3°) to the total pressure at the inlet (P_1°), meaning that this parameter quantifies the pressure rise achieved by the compressor stage:

$$\pi_{c_s} = \frac{P_3^\circ}{P_1^\circ} \tag{15}$$

The stage isentropic efficiency (η_{c_s}) measures how closely the compressor stage approaches an ideal, isentropic process. It is defined as the ratio of the ideal work required to achieve the pressure rise to the actual work input:

$$\eta_{c_s} = \frac{h_{3s}^\circ - h_1^\circ}{h_3^\circ - h_1^\circ} = \frac{\pi_{c_s}^{\frac{\gamma-1}{\gamma}} - 1}{\frac{T_3^\circ}{T_1^\circ} - 1} \tag{16}$$

where γ is the specific heat ratio (c_p/c_v), T_1° is the total temperature at the inlet and T_3° is the total temperature at the outlet.

A higher isentropic efficiency indicates that the compressor stage is performing closer to the ideal case, with minimal losses.

The stage polytropic efficiency (e_{c_s}) is another measure of compressor performance, particularly useful for multi-stage compressors. It represents the isentropic efficiency across each infinitesimal stage of the compression and is defined as:

$$e_{c_s} = \frac{\gamma - 1}{\gamma}\frac{ln(P_3^\circ/P_1^\circ)}{ln(T_3^\circ/T_1^\circ)} \tag{17}$$

The polytropic efficiency is often preferred for multi-stage compressors because it remains relatively constant across stages, unlike the isentropic efficiency, which tends to decrease with increasing pressure ratio.

2.2.7 Operating Range

Operating maps are used to characterize the operating range of a compressor, as seen in Figure 4. The pressure ratio and efficiency of a compressor are obtained as a function of the mass flow and rotation speed. The surge line represents the limit beyond which the compressor experiences unstable operations and stalled conditions. Surge occurs at low mass flows when the fluid can no longer stick to the blade surface. Additionally, it may be appreciated that as the rotation speed increases, the operating range decreases.

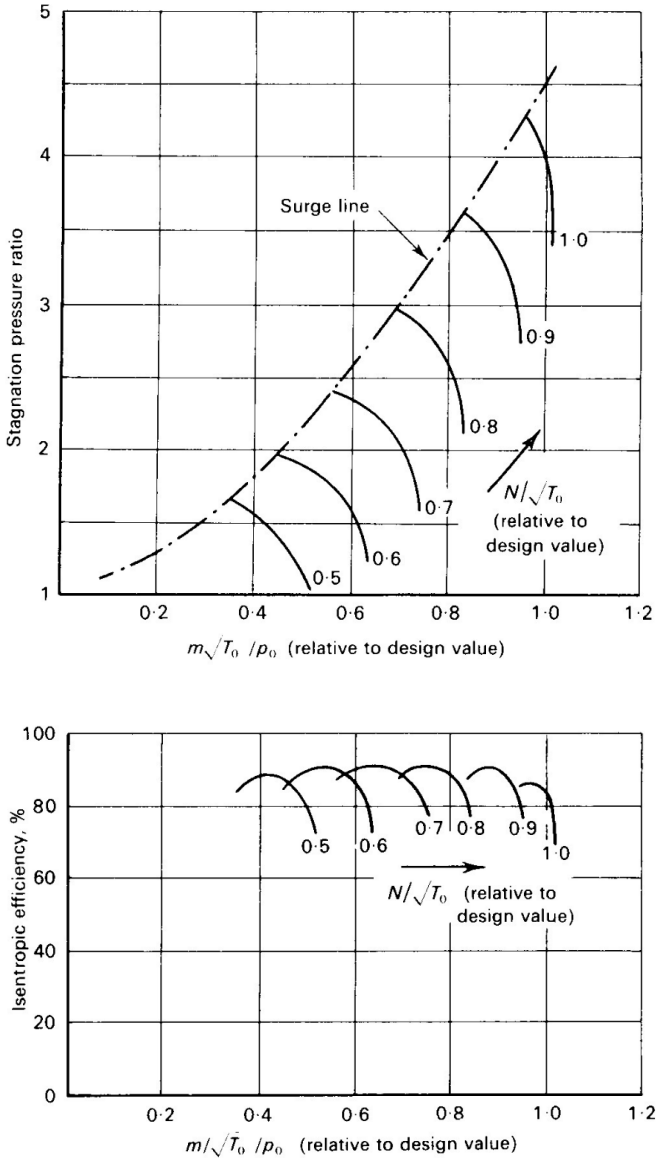

Figure 4. Characteristic maps of an axial compressor. Source: [11]

2.2.8 Stage Coefficients

The diffusion factor (D) is another important parameter in blade design, particularly for assessing the risk of flow separation on the suction side of the blade. It quantifies the deceleration of the flow along the blade surface and is defined as:

$$D = \frac{V_{max} - V_e}{V_i} = 1 - \frac{V_3}{V_2} + \frac{|v_2 - v_3|}{2\sigma V_2} \tag{18}$$

The diffusion factor is a measure of the adverse pressure gradient on the suction side of the blade. In Figure 5, the flow angle corrected loss coefficient is represented as a function of the diffusion factor. The loss coefficient beyond a diffusion factor of 0.6 shows a very rapid increase, which is why for practical applications, the diffusion factor is typically limited to 0.6 or less. Higher values of D lead to excessive deceleration of the flow, increasing the risk of flow separation and resulting in significant pressure losses.

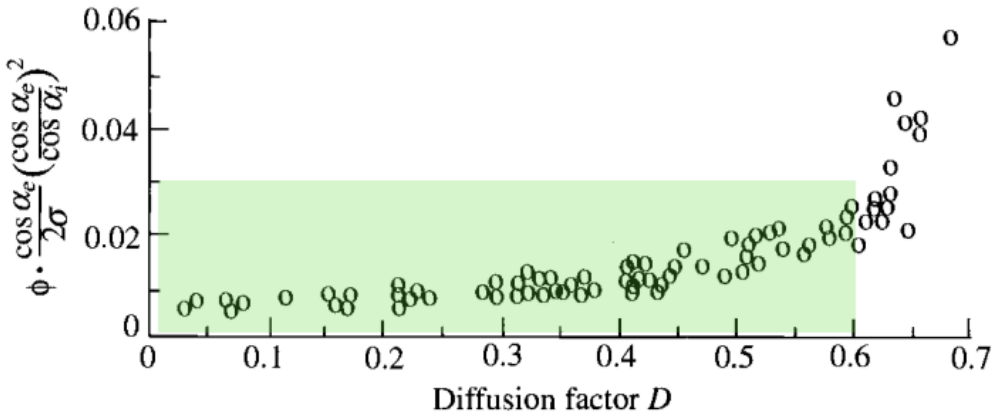

Figure 5. Diffusion factor and pressure losses. Source: [10]

The last concepts that are important to understand the effects of blade geometry are the stage loading coefficient (ψ) and the flow coefficient (φ), which provide insights into the energy transfer and flow characteristics within the blade row.

The stage loading coefficient is defined as:

$$\psi = \frac{c_p \Delta T^\circ}{U^2} \tag{19}$$

where $c_p \Delta T^\circ$ represents the change in enthalpy, and U is the tangential velocity of the blade. This coefficient indicates the work done by the blade row relative to the kinetic energy of the flow.

The flow coefficient, on the other hand, is given by:

$$\varphi = \frac{u_1}{U} = \frac{1}{\tan\alpha_1 + \tan\beta_1} \tag{20}$$

where u_1 is the axial velocity, and α_1 and β_1 are the inlet flow and blade angles, respectively. The flow coefficient helps in assessing the flow capacity and velocity triangles at the inlet.

The ratio of the stage loading coefficient to the flow coefficient provides a measure of the blade's ability to turn the flow and is expressed as:

$$\frac{\psi}{\varphi} = \tan\beta_1 - \frac{u_2}{u_1}\tan\beta_2 \tag{21}$$

This relationship highlights the importance of the blade angles and flow velocities in determining the aerodynamic performance and efficiency of the blade row.

The degree of reaction (R_c) is the last key stage coefficient in compressor design, defined as the ratio of the static enthalpy rise in the rotor to the total enthalpy rise in the stage. Mathematically, it is expressed as:

$$R_c = \frac{h_2 - h_1}{h_3^\circ - h_1^\circ} \tag{22}$$

For most compressors, the desired degree of reaction is around $R_c = 0.5$, which means that the rotor and the stator will share the burden of raising the fluid enthalpy. A degree of reaction of 0.5 ensures balanced loading on the rotor and stator, minimizing losses and improving efficiency.

By carefully designing the blade geometry and optimizing these coefficients, it is possible to achieve a balance between efficient energy transfer and minimal aerodynamic losses, ensuring optimal performance of the stage.

2.3 Outlet Guide Vane

The OGVs are a critical component in turbomachinery, particularly in compressors and turbines. They serve to straighten the flow exiting the rotor, converting the swirl component of the velocity into axial flow, which improves the efficiency of the downstream components. The design of OGVs involves careful consideration of blade geometry, solidity, and aerodynamic performance.

2.3.1 Cascade Geometry

The geometry of the OGV blades plays a crucial role in determining their aerodynamic performance. Key parameters of the blade geometry are illustrated in Figure 6:

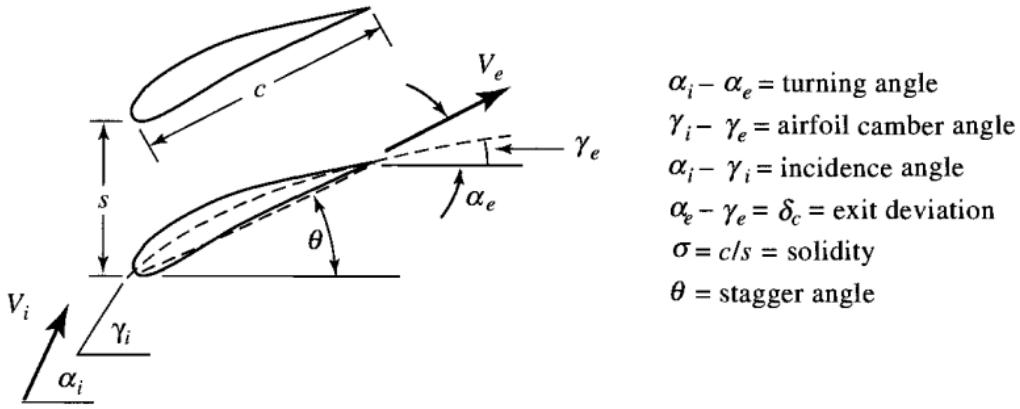

Figure 6. Blade geometry parameters. Source: [10]

The most important parameters include:

- Chord length (c): The straight-line distance between the leading and trailing edges of the blade.
- Spacing/pitch (s): The distance between adjacent blades at a given radius.
- Stagger angle (θ): The angle between the chord line and the axial direction.
- Inlet flow angle (α_i): The angle of the flow relative to the axial direction at the inlet.
- Exit flow angle (α_e): The angle of the flow relative to the axial direction at the exit.
- Inlet metal angle (γ_i): The inlet airfoil angle, tangent to the camber line.
- Exit metal angle (γ_e): The outlet airfoil angle, tangent to the camber line.

The solidity is defined as the ratio of the chord length (c) to the spacing (s):

$$\sigma = \frac{c}{s} \tag{23}$$

The spacing (s) is determined by the number of blades (n_b) and the mean radius (r_m):

$$s = \frac{2\pi r_m}{n_b} \tag{24}$$

A higher solidity generally improves the blade's ability to turn the flow but increases aerodynamic losses due to higher surface area and friction.

The exit airfoil angle (γ_e) is critical for ensuring that the flow exits the blade row with the desired direction. It can be computed using the following relationship:

$$\gamma_e = \frac{4\alpha\sqrt{\sigma} - \gamma_i}{4\sqrt{\sigma} - 1} \tag{25}$$

2.3.2 Cascade Performance

The key parameters that are used to quantify the performance of the operating point of the OGV and will be presented in this section are:

- Global Parameters
  - Pressure loss coefficient.
  - Working range.
  - Pressure rise.
  - Deviation.
  - Diffusion factor.
- Operating Parameters
  - Incidence.
  - Inlet Mach number.
  - Inlet Reynolds number.
- Flow Analysis
  - Isentropic Mach number distribution.
  - Flow fields.

Global parameters

The pressure loss coefficient quantifies the total pressure loss across the blade row relative to the dynamic pressure at the inlet and, as stated previously, is defined as [10]:

$$\phi = \frac{P_i^\circ - P_e^\circ}{P_i^\circ - P_i} \tag{26}$$

Observe that, as before, if incompressible or low Mach numbers flow is considered, the denominator of the previous equation becomes: $\frac{1}{2}\rho V_1^2$.

The pressure loss coefficient provides insight into the efficiency of the blade row, with lower values indicating better performance.

The pressure coefficient is used as a parameter to quantify the efficiency of the compressor as well. It is defined as:

$$\pi = \frac{P_e}{P_i} \tag{27}$$

In compressors, reducing the mass flow rate increases the pressure rise. However, this progression does not extend infinitely. Beyond a certain point where the pressure rise reaches a maximum, a further reduction in mass flow leads to a lower pressure rise, the flow behavior

changes and the compressor enters into either a stall or a surge condition. These two phenomena shall be further explained below.

The performance of the blades is highly dependent on the incidence angle, which is the angle between the incoming flow and the blade's chord line. Figure 7 represents the polar of the stage, where the pressure loss coefficient is plotted against different inlet flow angles. Two important parameters are highlighted in this Figure. On the one hand, the reference inlet flow angle is set to be where the pressure loss coefficient reaches a minimum. On the other hand, the operating range of the compressor, which has been highlighted as the shaded area, may be defined as the range of inlet flow angles within which the blade operates efficiently. Outside this range, some undesirable phenomena may occur:

- Flow separation: At high positive incidence angles, the flow may separate from the suction side of the blade, leading to increased pressure losses and reduced efficiency.
- Choke: At high negative incidence angles, the flow may choke, resulting in a sudden drop in performance due to shock waves or excessive diffusion.
- Stall: A local aerodynamic instability typically affecting one or several blades, caused by excessive angles of incidence or inlet flow distortions. It results in flow separation and loss of lift on the blade, which reduces performance and may induce vibrations, though the compressor can still operate. Stall is linked to the intrinsic geometry of the compressor and does not involve a complete breakdown of the flow.
- Surge: A global instability characterized by a complete breakdown of the flow through the compressor, potentially resulting in reverse flow. It occurs at low mass flow rates and high pressure ratios, and can lead to loud noise, severe vibrations, and mechanical damage. Surge significantly reduces compressor performance and may occur during rapid throttle changes or when operating outside the stable region of the compressor map.

For the present project, the working range has been defined by setting a reference inlet flow angle for the baseline configuration of 50º. Since stall usually appears at high incidence inlet flow angles when the pressure losses are about two times those of the reference inlet flow angle, in this work the working range has been arbitrarily defined as the region of inlet flow angles where the losses are within two times those of the reference inlet flow angle.

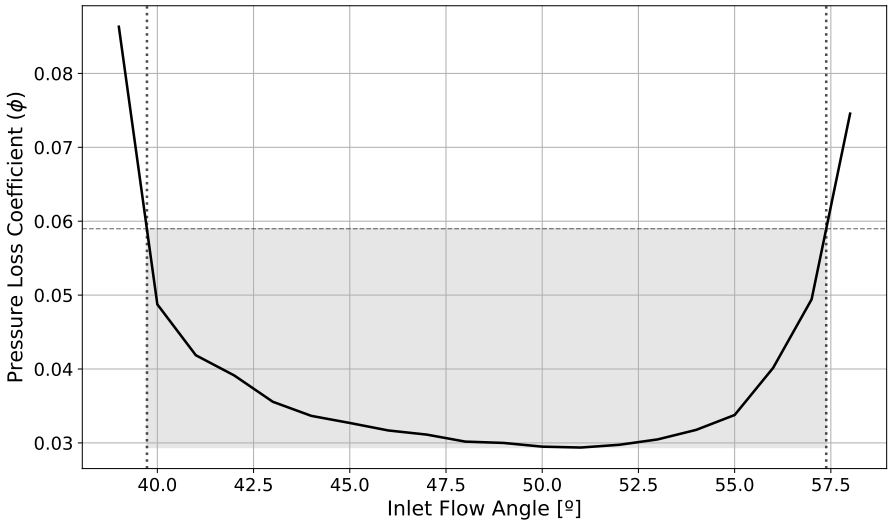

Figure 7. Pressure loss coefficient polar

The deviation angle is defined as the difference between the blade camber angle and the flow angle at the exit. Recall that it may be defined as:

$$\delta_c = \alpha_e - \gamma_e \tag{28}$$

Where δ_c is the deviation angle, α_e is the exit flow angle and γ_e is the airfoil metal angle at the outlet, tangent to the camber line. Recall that in the case of OGVs, the deviation angle must be high enough to ensure an axial flow at the outlet. Tandem blades are of special interest since they offer higher turning capabilities. A second boundary layer is generated on the rear blade surface and the turning can be achieved with smaller separation occurring [5].

As mentioned previously, the dimensionless diffusion factor is used to quantify the risk of flow separation in turbomachinery applications. It helps to predict boundary layer separation and to assess blade loading characteristics. It may be computed as [12]:

$$DF = 1 - \frac{\cos\gamma_i}{\cos\gamma_e} + \frac{\cos\gamma_i}{2 \cdot \sigma} \cdot (\tan\gamma_i - \tan\gamma_e) \tag{29}$$

Operating parameters

The three parameters that are used to differentiate across different operating point configurations are:

- Incidence: As it has been mentioned previously, the incidence angle is the angle between the incoming flow and the blade's chord line.
- Inlet Mach number: It is the ratio of the of the true airspeed of the flow to the speed of sound of air at a given operating point.

- Inlet Reynolds number: The Reynolds number quantifies the relative importance of inertial to viscous forces in the flow field. As will be seen in future sections, it is defined as:

$$Re = \frac{\rho u L}{\mu} \tag{30}$$

Where ρ denotes fluid density, u the characteristic velocity, L the relevant length scale and μ the dynamic viscosity.

Flow analysis

The first method that is used to study the flow is to analyze the distribution of the isentropic Mach number (M_{is}), which is a measure of the ideal surface Mach number that the blade would have without losses nor friction on the walls [13]. It is defined as:

$$M_{is} = \sqrt{\frac{2}{\gamma - 1}\left(\left(\frac{P^{\circ}_{in}}{P}\right)^{\frac{\gamma-1}{\gamma}} - 1\right)} \tag{31}$$

where P°_{in} is the total pressure of the inlet, P is the local static pressure and γ is the ratio of specific heats (for air $\gamma = 1$).

The isentropic Mach number is an important parameter for assessing the aerodynamic loading and potential for shock waves in the blade passage.

The other method used to study the flow is to analyze the distribution of the flow fields across the stage. For this project, the following flow fields will be studied:

- Mach number distribution.
- Static pressure distribution.
- Turbulent kinetic energy distribution.
- Ratio of turbulent to laminar viscosity distribution.

2.3.3 Tandem Blades

Tandem blades are a specialized configuration in turbomachinery where two airfoils are placed in close proximity within the same blade row. This design is particularly advantageous in high-loading applications, as it allows for better flow control, reduced losses, and improved aerodynamic performance compared to conventional single airfoils. The tandem configuration splits the aerodynamic load between two blades, enabling more efficient flow turning and reducing the risk of flow separation and stall.

The tandem blade configuration offers several key benefits:

- Improved Flow Turning: The first airfoil initiates the flow turning, while the second airfoil further guides the flow, reducing the likelihood of boundary layer separation. This results in smoother flow transitions and better overall turning efficiency.

- Reduced Loading on Individual Blades: By distributing the aerodynamic load between two blades, the tandem configuration minimizes the risk of flow separation and stall, particularly in high-loading conditions.
- Rear Blade Shielding: The rear blade is always shielded from incidence changes thanks to the boundary layer of the front blade. Thus, allowing to put most of the aerodynamic load on it.
- Enhanced Efficiency: The tandem design optimizes pressure distribution across the blades, reducing losses and improving overall efficiency. This is especially beneficial in applications that require a high pressure rise or flow deflection.

Despite their advantages, tandem blades also present some challenges:

- Increased Complexity: The design and manufacturing of tandem blades are more complex than single airfoils, requiring precise control over blade positioning and geometry.
- Aerodynamic Interaction: The close proximity of the two airfoils can lead to complex aerodynamic interactions, which must be carefully analyzed to avoid performance degradation. Proper optimization is essential to minimize adverse effects.

The primary effect of a tandem configuration is the interaction between the circulation of the front blade (FB) and the rear blade (RB). The rear blade influences the flow around the front blade, increasing the velocity on the suction side and decreasing it on the pressure side. This increases the loading on the front blade while reducing the demand for pressure recovery at its trailing edge, which helps prevent boundary layer separation. Additionally, the boundary layer experiences less growth, resulting in a higher wake velocity and reduced wake instability. The circulation generated by the front blade also reduces the velocity spike at the leading edge of the rear blade, further enhancing performance.

The relative positioning of the front and rear blades is critical for optimizing performance. Studies have shown that the axial overlap (AO) and percentage pitch (PP) significantly influence tandem blade performance. For subsonic conditions, an optimal configuration is typically around 0% AO and 90% PP. In transonic applications, a pitchwise shift of 15% to 30% of the pitch, combined with an axial overlap of up to 5% of the axial chord, has been found to enhance deflection and pressure rise while reducing losses. For high-loading conditions, tandem configurations allow for better redistribution of blade loading, with increased incidence angles shifting more load to the front blade and decreased incidence angles increasing the load on the rear blade [5] [6] [7] [8].

Tandem blades are highly application-specific, and their design requires careful consideration of operating conditions. Figure 8 illustrates the key geometric parameters in tandem blade configurations, highlighting the importance of axial overlap (AO) and percentage pitch (PP) in determining the relative position of the blades.

Those key parameters are related as follows:

$$PP = \frac{t}{s} \tag{32}$$

$$AO = \frac{\Delta x}{c_{ax}} \tag{33}$$

Where s is the pitch (separation between blades in cascade configuration), t is the vertical distance between the upper RB's LE and the lower FB's TE, Δx is the horizontal distance between the FB's TE and the RB's LE of the tandem configuration and $c_a x$ is the horizontal distance between the FB's LE and the RB's TE of the tandem configuration.

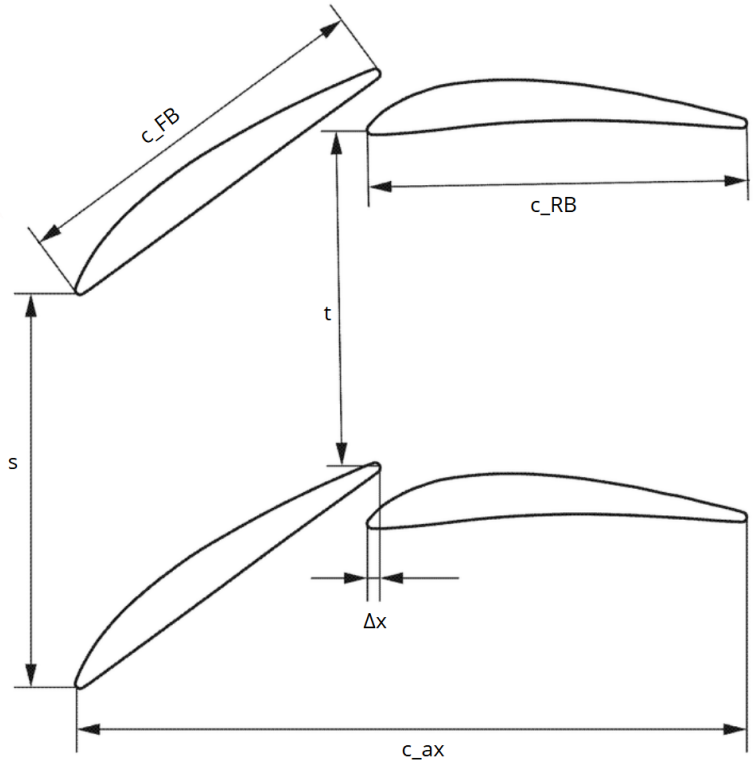

Figure 8. Defining parameters in tandem blade geometry.

Overall, tandem blades offer significant aerodynamic advantages in turbomachinery, particularly in high-loading applications. By carefully optimizing their configuration and addressing the associated challenges, tandem blades can achieve superior performance, making them a valuable tool in modern turbomachinery design.

2.3.4 Airfoil Parametrization for Optimization

As it has been mentioned previously, the goal of this work is to optimize the relative position of the tandem blades as well as their geometry from a baseline configuration. Thus, a method to characterize and modify the geometry of the blades is required.

The airfoil section shapes may be defined by the classical airfoil parametrization using the camber line angle and thickness distribution. Figure 9 illustrates each of the airfoil parameters. However, non-dimensional distributions for the camber line angles and the thickness are used. This kind of parametrization needs additionally a specification of the metal angles, the maximum thickness and the thickness at the leading and trailing edge.

Unlike the AO and the PP, which may be defined independently of the baseline geometry, the shape of an airfoil section shall be parametrized by considering the baseline airfoil configuration and altering the following parameters:

- Stagger angle modification (in degrees). Specified in counterclockwise direction.
- Chord length scaling.
- Thickness scaling.
- Shift of the maximum thickness point, normalized to the skeleton curve length.
- Metal angle modification at LE (in degrees). Specified in counterclockwise direction.
- Metal angle modification at TE (in degrees). Specified in counterclockwise direction.

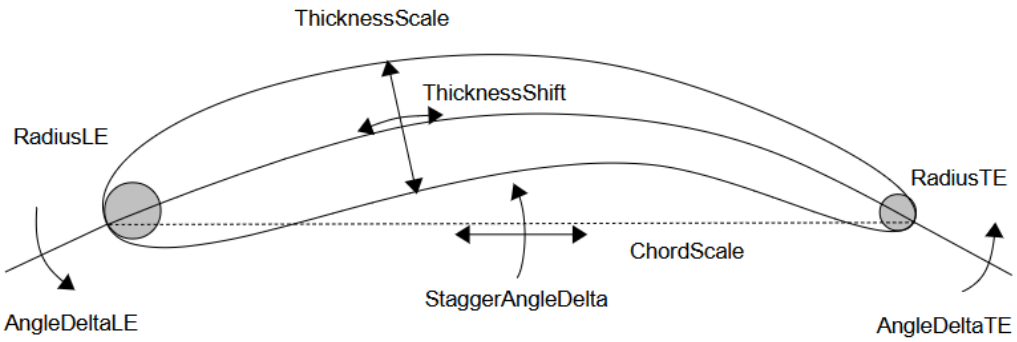

Figure 9. Defining parameters in airfoil geometry.

3 Flow Mechanics

In this section, an overview of the fundamentals of Computational Fluid Dynamics (CFD) shall be presented to understand how they affect the development of this project [14]. CFD aims to solve numerically, i.e., using a computer, the governing laws of motion of fluids. CFD is used as a means to perform virtual prototyping, simulation, and analysis of real-life configurations. Thanks to it, the number of real experiments required in the industry to validate the models has greatly decreased over the years. Its downside is that CFD can be very computationally demanding, while computational resources are limited. Thus, the accuracy of the results is often constrained by the available resources. There is a trade-off between the accuracy of the models used and their computational cost.

The governing laws of motion of fluids are described by the Navier-Stokes equations, which are a set of nonlinear partial differential equations that express the conservation of mass, momentum, and energy. In their general form, the Navier-Stokes equations can be written as:

$$\frac{\partial}{\partial t}\begin{bmatrix}\rho\\ \rho\mathbf{v}\\ \rho E\end{bmatrix} + \nabla\cdot\begin{bmatrix}\rho\mathbf{v}\\ \rho\mathbf{v}\times\mathbf{v} + p\mathbf{I} - \boldsymbol{\tau}\\ \rho\mathbf{v}H - \boldsymbol{\tau}\cdot\mathbf{v} - k\nabla T\end{bmatrix} = \begin{bmatrix}0\\ \rho\mathbf{f_e}\\ \rho\mathbf{f_e}\cdot\mathbf{v} + q_H\end{bmatrix} \tag{34}$$

These equations govern the motion of fluids, describing how the velocity, pressure, temperature, and density of the fluid evolve over time and space. However, when phenomena such as turbulence appear, the computational cost to solve the Navier-Stokes equations directly becomes excessive. Turbulence is characterized by chaotic, three-dimensional, and unsteady flow structures that span a wide range of length and time scales. Resolving all these scales directly, as in Direct Numerical Simulation (DNS), requires an enormous amount of computational resources, making it impractical for most engineering applications.

To address this challenge, lower-order models have been developed to approximate the effects of turbulence without resolving all the scales explicitly. These models introduce simplifications and assumptions to reduce the computational cost while still capturing the essential features of the flow.

3.1 Numerical Approaches

The most commonly used models in CFD include:

- DNS: DNS resolves all scales of turbulence without any modeling, providing the most accurate representation of the flow. However, it is computationally prohibitive for most practical applications due to the extremely fine grid and time-step requirements.
- LES: LES resolves the large, energy-containing eddies directly while modeling the smaller, subgrid-scale eddies. This approach provides a better representation of unsteady flow

features compared to RANS but at a higher computational cost. LES is often used for flows where unsteady effects are important, such as in aerodynamics and combustion.

- DES: DES is a hybrid approach that combines RANS for attached boundary layers with LES for separated regions. This allows for a balance between accuracy and computational cost, making it suitable for flows with both attached and separated regions, such as in aerospace applications.

- RANS: The RANS approach involves time-averaging the Navier-Stokes equations, resulting in equations that describe the mean flow properties. The effects of turbulence are modeled using a turbulence closure model, such as the k-ϵ or k-ω models. RANS is computationally efficient and widely used for industrial applications, but it may struggle to accurately capture unsteady or highly complex phenomena through the flow and the forces that act on the body.

For this project, the Reynolds-Averaged Navier-Stokes (RANS) model has been chosen due to its balance between computational efficiency and accuracy. Given that the study focuses on analyzing the flow around tandem blades across multiple configurations while performing an optimization study, the RANS model offers several advantages.

First, RANS provides time-averaged solutions, effectively capturing the overall behavior of the flow without requiring excessive computational resources. This is particularly beneficial when conducting parametric studies, where multiple simulations must be performed to explore different design configurations. Second, while LES or DNS would offer higher accuracy in capturing transient flow structures, their prohibitive computational cost makes them impractical for optimization studies involving many design iterations. Finally, the ability of RANS models to predict mean aerodynamic forces, pressure distributions, and overall performance metrics makes them well-suited for analyzing tandem blade aerodynamics and optimizing their design.

3.1.1 Reynolds-Averaged Navier-Stokes (RANS)

The RANS model is based on the time-averaged form of the Navier-Stokes equations, which are derived by decomposing the flow variables into their mean and fluctuating components. For a given flow variable ϕ, this decomposition is expressed as:

$$\phi = \tilde{\phi} + \phi'' \tag{35}$$

where $\tilde{\phi} = \frac{\overline{\rho\phi}}{\overline{\rho}}$ is the time-averaged value and ϕ'' is the fluctuating component.

Applying this decomposition to the Navier-Stokes equations and taking the time average yields the RANS equations:

$$\partial_t \overline{\rho} + \partial_j \overline{\rho}\, \tilde{u}_j = 0 \tag{36}$$

$$\partial_t \overline{\rho}\, \tilde{u}_i + \partial_j \overline{\rho}\, \tilde{u}_j \tilde{u}_i + \partial_i \overline{p} = \partial_j \bar{\tau}_{ji} - \partial_j \widetilde{u''_j u''_i} \tag{37}$$

$$\partial_t \overline{\rho}\tilde{E} + \partial_j \overline{\rho}\,\tilde{H}\,\tilde{u}_j = \partial_j \bar{\tau}_{ji}\tilde{u}_i - \partial_j \overline{\rho}\,\widetilde{u_j'' u_i''} - \partial_j \bar{q}_j \tag{38}$$

The term $-\overline{\rho}\,\widetilde{u_j'' u_i''}$ is known as the Reynolds stress tensor, which represents the effect of turbulence on the mean flow. To close the system of equations, a turbulence model is required to approximate the Reynolds stresses. Common turbulence models used in RANS include:

- k-ϵ **Model**: A two-equation model that solves for the turbulent kinetic energy (k) and its dissipation rate (ϵ). It is widely used for industrial applications due to its robustness and computational efficiency.
- k-ω **Model**: A two-equation model that solves for the turbulent kinetic energy (k) and the specific dissipation rate (ω). It is well-suited for wall-bounded flows and low-Reynolds number applications.
- **Spalart-Allmaras (SA) Model**: A one-equation model that solves a transport equation for the modified turbulent viscosity. It is particularly effective for aerodynamic flows and boundary layer problems.
- **Shear Stress Transport (SST) Model**: A hybrid model that combines the strengths of the k-ϵ and k-ω models. It uses the k-ω formulation near the wall to accurately capture boundary layer effects and switches to the k-ϵ model in the free-stream region to avoid sensitivity to inlet turbulence conditions. This makes the SST model highly accurate for a wide range of flow scenarios, including adverse pressure gradients and separated flows.

In this project, the SST turbulence model has been employed due to its ability to provide reliable predictions for both near-wall and free-stream regions, making it particularly suitable for the flow conditions under investigation. The RANS approach, combined with the SST model, offers a computationally efficient way to simulate turbulent flows by focusing on the mean flow properties while modeling the effects of turbulence. This balance between accuracy and computational cost is essential for engineering applications, where practical solutions are often required within reasonable timeframes.

3.2 Shear Stress Transport (SST) Turbulence Model

The Shear Stress Transport (SST) turbulence model, developed by Menter [15], is a widely used hybrid model that combines the strengths of the k-ω and k-ϵ turbulence models. It is designed to provide accurate predictions for both near-wall and free-stream regions, making it suitable for a broad range of flow conditions, including those with adverse pressure gradients and flow separation.

3.2.1 Formulation

The SST model is based on two transport equations: one for the turbulent kinetic energy k and another for the specific dissipation rate ω. The key feature of the SST model is its blending function, which smoothly transitions between the k-ω model near the wall and the k-ϵ model in the free-stream region. This blending ensures accurate resolution of boundary layer effects while maintaining robustness in regions away from the wall.

The transport equations for k and ω are given by:

$$\frac{\partial(\rho k)}{\partial t} + \frac{\partial(\rho u_j k)}{\partial x_j} = P_k - \beta^* \rho \omega k + \frac{\partial}{\partial x_j}\left[(\mu + \sigma_k \mu_t)\frac{\partial k}{\partial x_j}\right], \tag{39}$$

$$\frac{\partial(\rho \omega)}{\partial t} + \frac{\partial(\rho u_j \omega)}{\partial x_j} = \alpha \frac{\omega}{k} P_k - \beta \rho \omega^2 + \frac{\partial}{\partial x_j}\left[(\mu + \sigma_\omega \mu_t)\frac{\partial \omega}{\partial x_j}\right] + 2(1 - F_1)\frac{\rho \sigma_{\omega 2}}{\omega}\frac{\partial k}{\partial x_j}\frac{\partial \omega}{\partial x_j}, \tag{40}$$

where P_k is the production term for turbulent kinetic energy, μ_t is the turbulent viscosity, F_1 is the blending function that activates the k-ω model near the wall and the k-ϵ model in the free stream and α, β, β^*, σ_k, and σ_ω are model coefficients.

The blending function F_1 is defined as:

$$F_1 = \tanh\left(\arg_1^4\right), \tag{41}$$

where:

$$\arg_1 = \min\left[\max\left(\frac{\sqrt{k}}{\beta^* \omega y}, \frac{500\nu}{y^2 \omega}\right), \frac{4\rho \sigma_{\omega 2} k}{CD_{k\omega} y^2}\right], \tag{42}$$

y is the distance to the closest wall and $CD_{k\omega}$ is the cross-diffusion term given by:

$$CD_{k\omega} = \max\left(\frac{2\rho \sigma_{\omega 2}}{\omega}\frac{\partial k}{\partial x_j}\frac{\partial \omega}{\partial x_j}, 10^{-10}\right). \tag{43}$$

To close the Reynolds-averaged Navier-Stokes (RANS) equations, the SST model employs the Boussinesq approximation, which relates the Reynolds stresses to the mean velocity gradients via an eddy viscosity. The Reynolds stress tensor is modeled as:

$$-\overline{\rho}\widetilde{u_i'' u_j''} \simeq \mu_t(\nabla \tilde{u} + \nabla \tilde{u}^T - \frac{2}{3}\nabla \cdot \tilde{u} I) \tag{44}$$

where μ_t is the turbulent (or eddy) viscosity, $\tilde{u}$ is the mean velocity vector, I is the identity tensor, and $\nabla \tilde{u}$ is the velocity gradient tensor.

The turbulent eddy viscosity μ_t in the SST model is computed using:

$$\mu_t = \frac{\rho a_1 k}{\omega}, \tag{45}$$

With a limiter to ensure that turbulent shear stress does not exceed a specified fraction of the turbulent kinetic energy:

$$\mu_t = \frac{\rho a_1 k}{\max(a_1 \omega, S F_2)}, \tag{46}$$

where a_1 is a model constant, S is the magnitude of the strain-rate tensor, and F_2 is another blending function similar to F_1, ensuring a smooth transition between models across the boundary layer. The blending function F_2 is computed as:

$$F_2 = \tanh\left(\arg_2^2\right), \tag{47}$$

where:

$$\arg_2 = \max\left(\frac{\sqrt{k}}{\beta^* \omega y}, \frac{500\nu}{y^2 \omega}\right) \tag{48}$$

The SST model offers several advantages:

- Accuracy in Near-Wall Regions: The use of the k-ω formulation near the wall ensures precise resolution of boundary layer effects, including viscous sublayers and adverse pressure gradients.
- Robustness in Free-Stream Regions: The transition to the k-ϵ model in the free stream avoids the sensitivity of the k-ω model to inlet turbulence conditions.
- Versatility: The SST model is applicable to a wide range of flow scenarios, including aerodynamic flows, turbomachinery, and industrial applications.

3.3 Boundary Layer Analysis

The boundary layer represents a fundamental concept in fluid dynamics that describes the thin region of fluid immediately adjacent to solid surfaces where viscous effects dominate the flow behavior. When a fluid flows past an object (or conversely, when an object moves through a fluid) the interaction between fluid molecules and the surface creates complex force distributions that depend on the fluid's viscosity and compressibility. Near the surface, fluid molecules adhere to the solid boundary due to viscous forces, while successive layers experience gradual deceleration effects until reaching the free stream velocity. This velocity transition zone, known as the boundary layer, typically extends only a few millimeters to centimeters from the surface but has a huge influence on the overall system performance [16].

Its characteristics influence aerodynamic performance, particularly in turbomachinery applications where boundary layer development affects efficiency losses, heat transfer rates, and flow separation phenomena.

3.3.1 Inner and Outer Flow Characteristics

The flow field around immersed bodies presents different behaviors between the inner boundary layer region and the outer inviscid flow. The outer flow, which is found beyond the boundary layer thickness (δ), is characterized by negligible viscous effects. It behaves as an ideal inviscid fluid where only pressure forces influence fluid motion. In this region, the pressure acting through the center of fluid elements produces pure translational motion without rotational components, maintaining zero angular momentum for initially irrotational flows. This irrotational property allows the outer flow to be accurately modeled using potential flow theory, significantly simplifying aerodynamic analyses while providing reasonable approximations for pressure distributions over streamlined bodies.

On the other hand, the inner flow within the boundary layer exhibits complex viscous-dominated behavior with three distinct regimes:

1. Laminar Region: The flow remains smooth and orderly with minimal temporal variations, characterized by steady parabolic velocity profiles. In this regime, viscous forces dominate completely, creating stable streamlines that vary only slowly with time.

2. Transition Region: This region is where laminar flow begins to break down, leading to the appearance of intermittent turbulent spots within an otherwise smooth flow. The transition process initiates when the Reynolds number exceeds a critical value ($Re_x \approx 0.5 \times 10^6$ for smooth surfaces), with the exact threshold depending on surface roughness, pressure gradients, and free-stream turbulence intensity. The flow exhibits rapid fluctuations in shear stress during this phase.

3. Turbulent Region: Characterized by chaotic, three-dimensional motions with random velocity fluctuations typically reaching ±20% of the mean flow value. Despite the apparent randomness, time-averaged turbulence velocity components are null. Thus, the flow may be described as a steady or slowly varying mean flow. Additionally, this regime also has a thin laminar sublayer close to the body surface.

The velocity profile across these regions evolves from zero at the wall (no-slip condition) to the free-stream velocity U_∞ at the boundary layer edge. Figure 10 shows the boundary layer evolution through a flat plate. It may be noted that the thickness of the turbulent region is considerably larger than that of the laminar one.

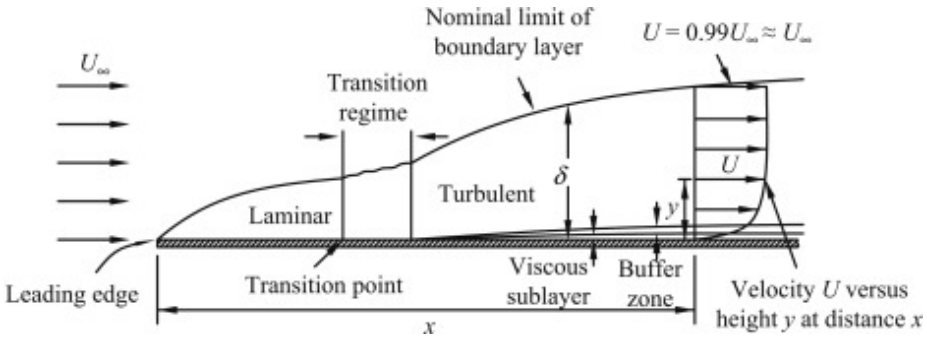

Figure 10. Boundary layer progression. Source: [17]

The interaction between inner and outer flows creates several critical phenomena such as:

- Displacement effects modifying the effective body shape perceived by the outer flow.
- Pressure gradient transmission across the boundary layer.
- Flow separation when adverse gradients overcome the boundary layer's momentum.
- Vorticity generation confined to the viscous regions.

Understanding this inner-outer flow coupling is essential for predicting aerodynamic performance, particularly in applications involving flow control, drag reduction, and separation prevention. The boundary layer's transition from laminar to turbulent states, while increasing local skin friction, often improves overall system performance by delaying flow separation.

3.3.2 Reynolds Number

The Reynolds number, defined in Equation 49, quantifies the relative importance of inertial to viscous forces in the flow field [18].

$$Re = \frac{\rho u L}{\mu} = \frac{uL}{\nu} \tag{49}$$

where ρ denotes fluid density, u the characteristic velocity, L the relevant length scale, μ dynamic viscosity, and ν kinematic viscosity.

The Reynolds number is used to characterize the flow in the boundary layer, since it can determine:

- The transition between laminar and turbulent flow regimes.
- Boundary layer development characteristics.
- Separation susceptibility and drag properties.

In compressor blade applications, typical chord-based Reynolds numbers range from 5×10^5 to 2×10^6, often placing the flow in transitional or slightly turbulent regimes. This requires careful consideration of transition models in CFD simulations to accurately capture the onset of turbulence and its subsequent development along blade surfaces.

3.3.3 Skin Friction

The frictional drag generated by viscous shear stresses acting on a body's surface represents a fundamental component of total drag in fluid flows. As illustrated in Figure 10, the surface shear stress τ_w arises from the velocity gradient at the wall and is quantified by:

$$\tau_w = \mu \left(\frac{\partial u}{\partial y} \right)_{y=0} \tag{50}$$

where μ is the dynamic viscosity and $(\partial u/\partial y)_{y=0}$ represents the velocity gradient normal to the surface. This shear stress is conventionally expressed through the local skin friction coefficient:

$$C_f = \frac{\tau_w}{\frac{1}{2}\rho U_\infty^2} \tag{51}$$

The boundary layer regime profoundly impacts skin friction characteristics:

- Laminar boundary layers exhibit relatively gentle velocity gradients at the wall, resulting in lower C_f values.
- Turbulent boundary layers develop steeper near-wall gradients (Figure 10), generating significantly higher skin friction despite their superior resistance to flow separation.

For engineering calculations, the skin friction coefficient and boundary layer thickness can be estimated using the following formulations:

- Laminar Flow (Blasius Solution):

$$C_f = \frac{1.328}{\sqrt{Re_x}} \tag{52}$$

$$\delta = \frac{4.91x}{\sqrt{Re_x}} \tag{53}$$

- Turbulent Flow (1/7 Power Law Velocity distribution):

$$C_f = \frac{0.072}{Re_x^{1/5}} \tag{54}$$

$$\delta = \frac{0.37x}{Re_x^{1/5}} \tag{55}$$

The transition between laminar and turbulent behavior occurs typically in the range $10^5 < Re_x < 10^6$, with the exact threshold depending on:

- Surface roughness (increases with roughness height).
- Free-stream turbulence intensity (promotes earlier transition).
- Pressure gradient (favorable gradients delay transition).
- Body curvature (affects stability characteristics).

3.3.4 Wall Function Analysis

Turbulent flows are fundamental in CFD simulations and are particularly sensitive to wall boundary conditions, where viscosity-dominated regions exhibit strong solution gradients.

The dimensionless wall distance y^+ serves as the fundamental parameter governing near-wall mesh resolution requirements in wall-bounded turbulent flows as can be seen in Figure 11 [19]:

$$y^+ = \frac{yu_\tau}{\nu} = \frac{y\sqrt{\tau_w/\rho}}{\nu} \tag{56}$$

where y is the wall-normal distance, u_τ the friction velocity ($u_\tau \equiv \sqrt{\tau_w/\rho}$), τ_w the wall shear stress, and ν the kinematic viscosity. The y^+ value represents a local Reynolds number that determines the relative importance of viscous and turbulent processes in the near-wall region as may be seen from Figure 12.

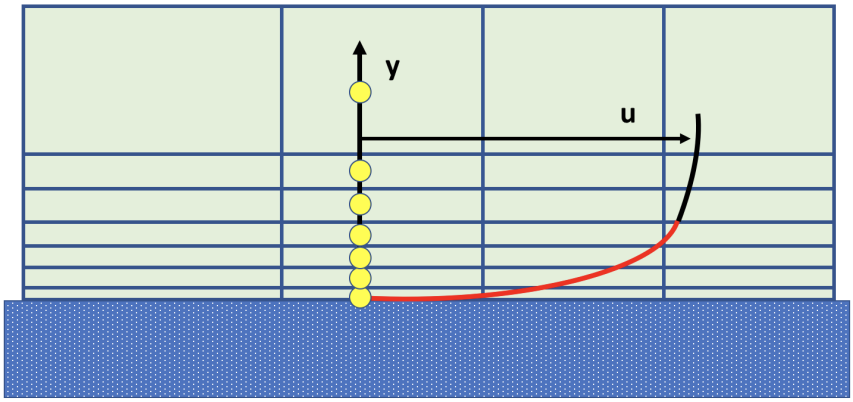

Figure 11. Viscous sublayer resolved by progression of cell size. Source: [19]

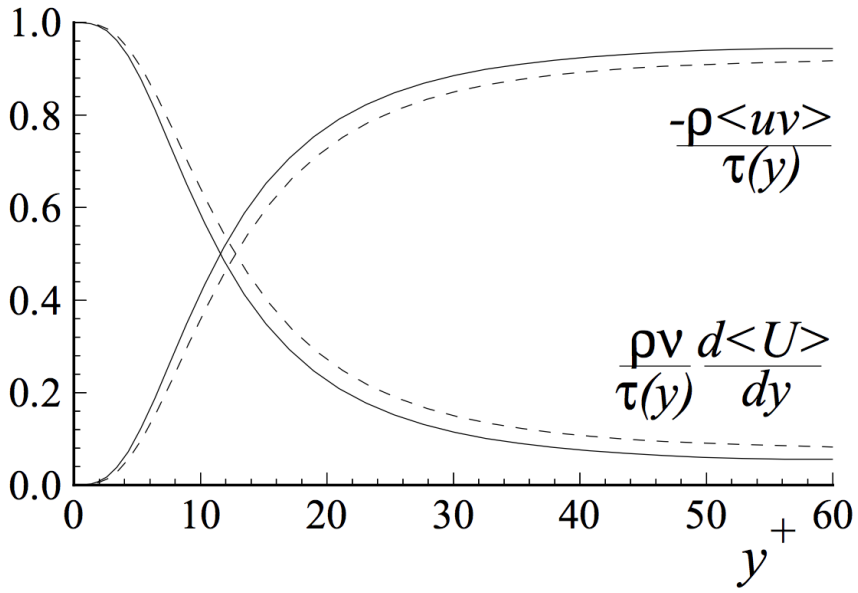

Figure 12. Contribution of viscous and Reynolds stresses to total stress. Source: [19]

Additionally, the dimensionless velocity is defined as:

$$u^+ = \frac{u}{u_\tau} \tag{57}$$

This parameter provides a way to compare velocities across different flow regions.

Accurate near-wall modeling is critical for predicting wall-bounded turbulent flows. Two primary approaches exist for handling the near-wall region:

- Low-Reynolds Number Modeling:
  - Resolves flow down to the wall with $y^+ \approx 1$ at first grid point.
  - Uses modified turbulence models (e.g., k-w SST) suitable for viscous sublayer.
  - Requires dense meshing (15-20 cells within $y^+ < 30$) but provides accurate wall shear predictions.
  - Essential for turbomachinery blade optimization and aerodynamic force calculations.
  - Approach that has been implemented in this project.
- Wall Function Approach:
  - Applies logarithmic law boundary conditions ($30 < y^+ < 300$).
  - Reduces computational cost but sacrifices viscous sublayer accuracy.
  - Model-specific implementations (different for k-ϵ vs k-ω).

Turbulent flows present different regions near walls with different physical behaviors. A similar classification to that which has been previously performed using the Reynolds number may be performed by using y^+:

- Viscous Sublayer ($y^+ < 5$): Dominated by viscous effects where $\tau_{\text{total}} \approx \tau_{\text{viscous}}$ and $u^+ = y^+$.
- Buffer Layer ($5 < y^+ < 30$): Transition region with comparable viscous and turbulent stresses.
- Logarithmic Layer ($30 < y^+ < 300$): Turbulence-dominated region following the log-law velocity profile where $u^+ = \frac{1}{\kappa} ln(y^+) + B$. Where κ is the Karman constant and B = 5.2.
- Outer Layer ($y^+ > 300$): Inertia-dominated region with negligible viscous effects.

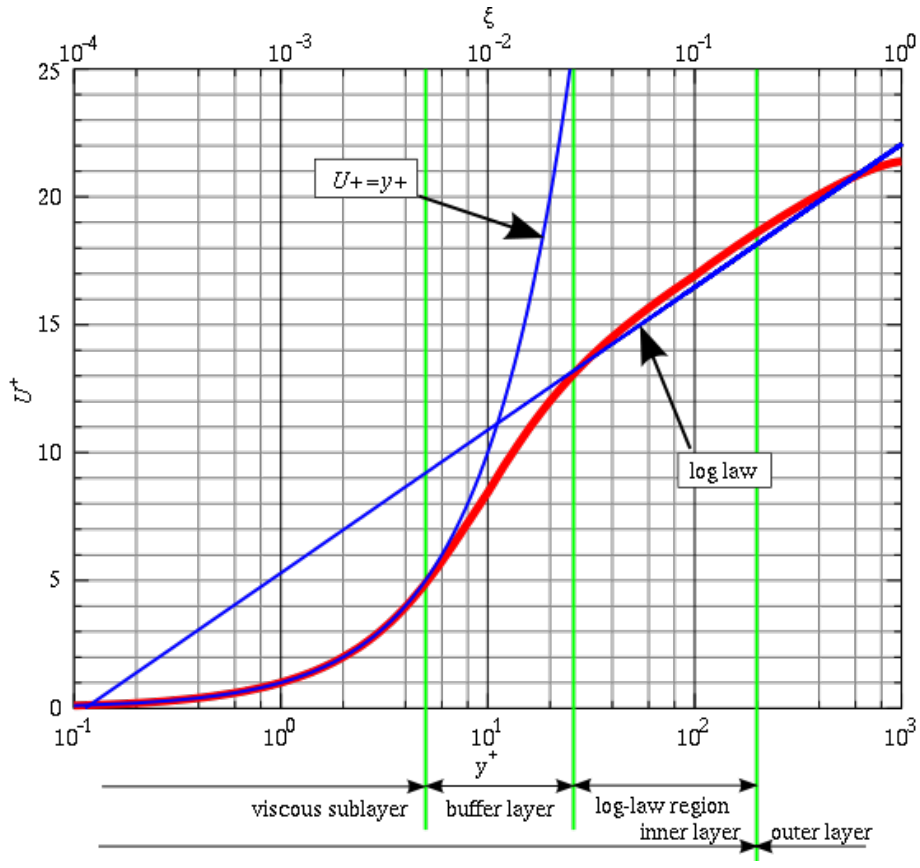

Figure 13. The Law of the Wall, relationship between u^+ and y^+ across different regions. Source: [19]

3.4 Wake and Boundary Layer Separation

Boundary layer separation occurs when the viscous flow detaches from the surface due to adverse pressure gradients, creating characteristic wake structures [20].

The process begins at the leading edge stagnation point where the flow divides, accelerating over the airfoil surface with a favorable pressure gradient (decreasing pressure) until reaching the

point of maximum thickness. Beyond this point, the flow decelerates under an adverse pressure gradient (rising pressure), causing the boundary layer to thicken and eventually separate when the near-wall flow reverses direction. This separation creates a low-pressure wake region containing large-scale vortices that extract energy from the main flow. This turbulent boundary layer resists separation better than the laminar one.

The consequences and characteristics of boundary layer separation include:

- Energy losses: Significant kinetic energy becomes is dissipated in the wake region, extracted from the main flow.
- Flow disturbances: Creates recirculation zones and turbulence downstream of separation points which, in turn, increases losses.
- Geometric sensitivity: Potential for abrupt stall at critical angles of attack.

The complex wake structure seen in Figure 14 shows how boundary layer separation creates complex flow disturbances downstream of the separation point.

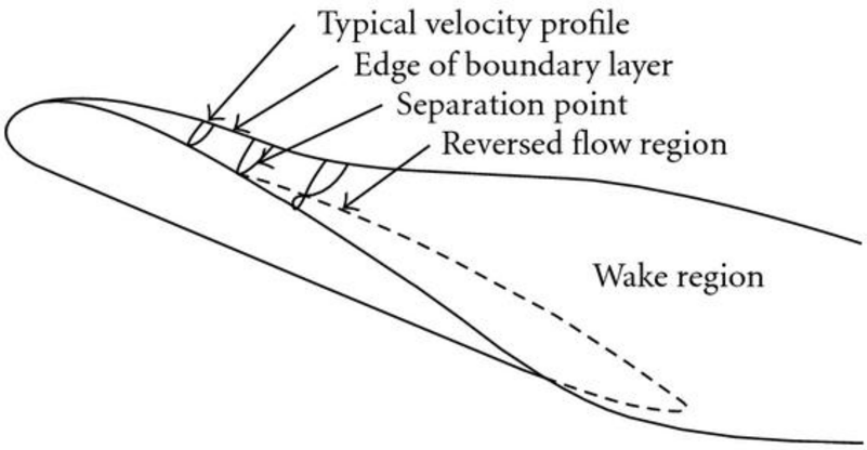

Figure 14. Wake formation behind an airfoil showing boundary layer separation. Source: [21]

4 Working Environment

In this section, an overview of the computational resources employed in this research will be provided. Most of the used tools are open-source solutions that ensure the reproducibility and accessibility of the research methodology.

4.1 Cenaero

All research presented in this thesis has been conducted in collaboration with Cenaero, a private non-profit applied research center specializing in numerical simulation methods for technological innovation. Internationally recognized for its expertise, Cenaero supports industrial partners across multiple domains including aeronautical design, spacecraft engineering, advanced manufacturing processes, and smart city development [22].

The center provides expertise in several technical areas, such as:

- High-performance composites and materials science.
- Multidisciplinary optimization and uncertainty quantification.
- Advanced computational fluid dynamics (including hypersonic flows and ablative materials).
- Turbomachinery design and thermo-fluid systems.
- Metallic manufacturing process modeling.

Cenaero maintains a robust HPC infrastructure comprising 14,000 computing cores dedicated to both fundamental and applied industrial research. The organization holds EN 9100:2018 and ISO 9001:2015 certifications, ensuring quality standards in its research and engineering services.

4.1.1 Minamo

As part of its software portfolio, Cenaero develops *Minamo*, a specialized platform for design space exploration and machine learning-based optimization. This tool complements Cenaero's other computational platforms including:

- *Argo*: Massively parallel multi-physics simulation environment for fluid-related computations using Direct Numerical Simulations (DNS) and Large Eddie Simulations (LES).
- *Morfeo*: Manufacturing process simulation and crack propagation analysis system.

Minamo employs a Surrogate-Based Optimization (SBO) approach, a methodology that uses surrogate modeling techniques to efficiently identify local or global optima. SBO is particularly well-suited for engineering applications involving computationally expensive simulations, such

as Computational Fluid Dynamics (CFD) or Computational Structural Dynamics (CSD). By approximating the behavior of these high-fidelity models, surrogate models enable faster optimization by filtering numerical noise, facilitating parallel computation and supporting the integration of multidisciplinary simulations [23].

The Minamo platform integrates with Cenaero's HPC infrastructure, enabling efficient parameter studies and optimization workflows that support the research methodologies employed in this thesis.

4.2 LUCIA

The LUCIA supercomputer honors the memory of Lucia De Brouckère, renowned chemist and former professor at the Faculty of Sciences of the Université Libre de Bruxelles [22].

4.2.1 Infrastructure Overview

Funded by the Walloon Region and hosted within Charleroi's A6K ecosystem, LUCIA is based on HPE Apollo systems supplied by Axians (a VINCI Energies subsidiary). The system comprises three specialized partitions:

- A 300-node CPU partition for general computation.
- A 50-node GPU partition for accelerated computing.
- A heterogeneous partition supporting specialized workloads (AI, visualization, and large-memory applications).

All partitions are interconnected via a high-performance Infiniband HDR network. With a combined peak performance of approximately 4 PetaFLOPS across CPU and GPU partitions, LUCIA achieved the 245th position in the November 2022 Top500 ranking based on its GPU performance metrics.

The infrastructure features:

- 10 Gbps connection to Belnet (Belgian research network).
- High-speed access to GÉANT (European research network).
- Standard internet connectivity.

4.2.2 SSH

The High Performance Computing (HPC) system LUCIA employs a Secure Shell (SSH) protocol for secure remote access, with all user connections initially established through dedicated login nodes.

Connection to LUCIA follows a two-stage process: users must first authenticate through the SSH gateway, then proceed to the login nodes. These login nodes serve as the operational interface, enabling users to compile applications, submit batch jobs via the SLURM workload manager, and interact with allocated computational resources.

The SSH gateway functions as a secure jump host, primarily serving Cenaero personnel and industry users. This gateway maintains an independent authentication system and filesystem, requiring users to synchronize credential updates (including password changes and SSH key modifications) across both the gateway and LUCIA's login nodes. Storage allocation on the gateway follows a quota system with:

- 10GB soft limit with warning notifications.
- 40GB hard limit for absolute restriction.
- 7-day grace period for quota compliance.

LUCIA's login infrastructure comprises two redundant nodes accessible through the unified hostname `frontal.lucia.cenaero.be`, which employs DNS round-robin for automatic load balancing. This dual-node architecture ensures high availability while maintaining consistent user experience across access points [22].

4.2.3 Job Submission

The LUCIA cluster uses Slurm Workload Manager (version 23.02) for job scheduling and resource management. Users can submit parallel SU2 simulations using MPI through several dedicated partitions. The ones that have been used in this work are:

- Batch partition: Designed for production runs and Minamo optimization jobs (260 nodes available, 128 CPUs/node, 240GB memory/node)
- Medium partition: Suitable for larger memory requirements (30 nodes, 128 CPUs/node, 492GB memory/node).
- Debug partition: Reserved for testing and debugging (10 nodes, 128 CPUs/node, 240GB memory/node).

The memory allocations of the partitions are optimized at 1920MB per CPU for batch/debug partitions and 3936MB per CPU for the medium partition.

4.3 Programming Languages

The computational work in this thesis was implemented using the following programming languages and scripting environments:

- Python (primary implementation language).
- Bash shell scripting (system operations and job control).

4.3.1 Python

Python served as the primary programming language for this research due to its extensive scientific computing ecosystem. As an interpreted, high-level language, Python enabled rapid development and testing of numerical algorithms while maintaining code readability. Key Python packages utilized include:

- NumPy and SciPy for numerical computations.
- Matplotlib for data visualization.
- Pandas for data analysis and processing.

The language's open-source nature and cross-platform compatibility facilitated its integration with LUCIA's HPC environment [24].

4.3.2 Bash

As LUCIA operates on a Linux architecture, Bash shell scripting was employed for:

- Automated job submission via SLURM.
- Filesystem operations and data management.
- Workflow automation and pipeline control.

Bash provided critical low-level system control and batch processing capabilities that complemented Python's high-level functionality [25].

4.4 CFD Solvers

The computational fluid dynamics (CFD) simulations in this thesis were performed using open-source solvers, selected for their capabilities in handling turbomachinery applications.

SU2 was chosen as the primary CFD solver for this research due to its:

- Streamlined workflow for turbomachinery applications.
- Flexible mesh requirements (2D/3D capability).
- Open-source architecture enabling code transparency.

Originally developed at Stanford University, SU2 has evolved into a comprehensive open-source C++/Python framework for solving partial differential equations (PDEs) and PDE-constrained optimization problems on unstructured meshes. The solver's specialized design for computational fluid dynamics and aerodynamic shape optimization includes native support for MPI-parallel computations, enabling efficient scaling across LUCIA's HPC infrastructure. SU2's proven industry applications in aeronautical, automotive, and renewable energy sectors, combined with its robust parallel computing capabilities, further validated its selection for this research [26].

4.5 Grid Generation

While SU2 includes a native mesh generation package optimized for simplicity and readability, the complex geometries investigated in this thesis require more advanced grid generation capabilities.

For the development of this work, the Gmsh software which is compatible with SU2 has been used for grid generation purposes.

Gmsh serves as the primary mesh generation tool for this research, offering a comprehensive open-source solution for 2D/3D finite element meshing with integrated CAD capabilities. This versatile tool combines four core functional modules:

- Geometry construction.
- Mesh generation.
- Solver integration.
- Post-processing visualization.

Key features that make Gmsh particularly suitable for the computational workflow that has been used in this thesis include:

- Multi-interface control through GUI, command line and its native .geo scripting language.
- Direct mesh export capability compatible with SU2.
- Advanced anisotropic mesh refinement for boundary layer and wake resolution.

The software's scripting capabilities proved particularly valuable, enabling batch generation of optimized meshes across multiple geometric configurations while maintaining consistent quality metrics. These features, combined with the software's active development community and documented success in aerospace applications, make it ideally suited for high-fidelity CFD investigations [27].

4.6 Visualization

To post-process the solution files from SU2, a data visualization tool is required.

It is important to note that SU2 currently supports ASCII and binary output formats which may be read by ParaView and Tecplot, respectively. However, while the former is freely available under an open-source license, the latter is a commercially licensed software. Additionally, Paraview's native support for parallel processing and HPC environments makes it particularly suitable for use with LUCIA's computational infrastructure. Hence, it has been selected as the software used for this project to visualize and post-process the solution files from SU2 [28].

ParaView has emerged as the leading open-source visualization tool for scientific computing, offering a powerful combination of interactive exploration and batch-processing capabilities. Developed as part of the VTK (Visualization Toolkit) project, it provides several key features essential for this research:

- Multi-view Data Exploration: Simultaneous visualization of multiple data components with customizable views, including specialized plugins for turbomachinery-specific representations.
- Advanced Filtering: Extensive built-in filters complemented by programmable filters through Python scripting, enabling custom data transformations key to CFD analysis.

The software's scripting interface proved particularly valuable for this research, allowing:

- Automated processing of large simulation datasets.
- Custom quantitative analysis pipelines.
- Batch generation of standardized visualization outputs.

ParaView's HPC capabilities deserve special mention, as its MPI-parallel architecture enables:

- Distributed processing of multiple datasets across LUCIA's nodes.
- Efficient client-server operation for remote visualization.

For turbomachinery applications specifically, ParaView provides:

- Specialized streamlines and pathlines for flow analysis.
- Advanced scalar and vector field visualization.
- Blade-to-blade view generation capabilities.

The software's active development under the Exascale Computing Project ensures continued performance improvements, making it well-suited for current and future high-fidelity CFD investigations [28]. Its combination of interactive and programmable features, coupled with robust parallel processing capabilities, made ParaView the optimal choice for visualizing and analyzing the complex flow fields generated in this research.

5 Computational Setup

In this section, the steps of the first phase where the project is prepared shall be discussed. More specifically, the process employed to improve the quality of the mesh and the CFD numerical settings will be further detailed. Additionally, some defining parameters of the baseline configuration geometry shall be presented.

5.1 Baseline Configuration Parameterization

Parameter	Symbol	Front Blade	Rear Blade	Tandem Blade	Units
Axial chord	C_{ax}	$0.451837 \cdot C_{axT}$	$0.516905 \cdot C_{axT}$	0.029400	m
Chord	C_{tot}	$0.533643 \cdot C_T$	$0.487900 \cdot C_T$	0.031611	m
Spacing	s	-	-	0.017136	m
Solidity	σ	-	-	1.844071	-
Axial Overlap	AO	-	-	-3.1276436	%
Percentage Pitch	PP	-	-	91.749457	%
Exit Flow Angle	α_e	-	-	0.38	deg
Pressure Loss Coefficient	ϕ	-	-	0.0295	-
Working range	$\Delta\alpha$	-	-	17.65	deg

Table II. Tandem blade configuration parameters

5.2 Mesh Refinement

Mesh quality represents a fundamental aspect of CFD simulations, particularly in regions that exhibit strong flow gradients such as boundary layers and wake regions. Proper mesh refinement directly impacts the accuracy and reliability of numerical solutions [29].

In CFD modeling, the computational domain is discretized into small cells or elements that constitute the mesh. Each cell represents a discrete volume where the governing flow equations are solved locally, enabling the computation of time-dependent flow properties (velocity, pressure, temperature) throughout the domain.

The mesh generation process involves several critical considerations:

- Geometric representation: The segmented airway surface defines the boundary conditions, while the internal volume requires careful discretizations.
- Cell topology: Selection between structured, unstructured, or hybrid mesh approaches based on geometric complexity.

- Resolution requirements: Varying cell density according to local flow physics (boundary layers, separation regions).
- Quality metrics: Ensuring proper aspect ratio, skewness, and orthogonality for numerical stability.

5.2.1 Optimal Number of Cells

The determination of an optimal cell count represents a critical phase in the computational analysis, requiring a balance between solution accuracy and computational efficiency. Beginning with an initial coarse mesh (designated M0) comprising approximately 8,000 cells, the preliminary simulations revealed several limitations in the mesh quality, particularly in regions of high flow gradients. The initial mesh presented abrupt cell size transitions and insufficient resolution in aerodynamically sensitive areas, including the boundary layer along blade surfaces, the gap between the blades and the wake regions downstream of the trailing edges. These deficiencies proved that a systematic refinement procedure of the mesh was required.

The first refinement strategy employed an iterative approach where each subsequent mesh (M_{n+1}) contained approximately double the cell count of its predecessor ($N_{n+1} \approx 2N_n$). Flow properties were monitored at a strategically selected position x = 1.51 m downstream of the rear blade's trailing edge, as can be seen in Figure 15, chosen for its ideal compromise between capturing blade-influenced flow characteristics and allowing sufficient wake development. This location serves both computational and potential experimental validation purposes, as it provides representative flow conditions while avoiding immediate disturbances near the blade surfaces. Note that all future flow properties of the study will be analyzed at this point (such as pressure losses, exit flow angles, etc). The convergence between successive mesh refinements was quantified using the Root Mean Square Error (RMSE) metric, calculated according to:

$$\varepsilon_{\text{RMS}} = \sqrt{\frac{1}{n}\sum_{i=1}^{n}\left(\frac{x_i^{(n-1)} - x_i^{(n)}}{x_i^{(n-1)}}\right)^2} \tag{58}$$

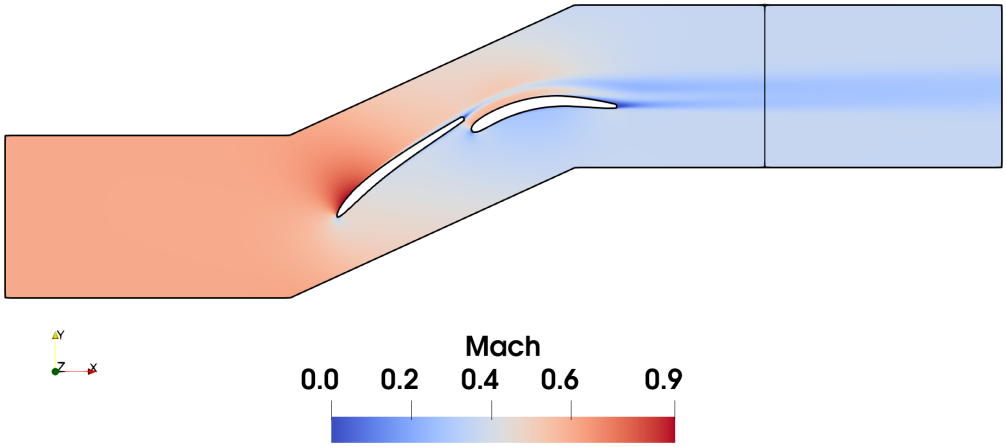

Figure 15. Location where flow properties have been studied

The following conclusions may be obtained from Figure 16 and Table III:

- Initial meshes (M1-M3) showed RMSE values exceeding 1%, indicating significant solution dependence on grid resolution.
- Subsequent refinement to M5 provided only marginal improvement (less than 1%), justifying the selection of M4 as the optimal configuration.

Mesh	**Element Type**	**Number of cells**	**RMSE [%]**
Mesh 1	Quads	7790	-
	Triangles	102	
Mesh 2	Quads	13395	2.056767
	Triangles	18	
Mesh 3	Quads	22560	1.676424
	Triangles	4	
Mesh 4	Quads	37872	1.300260
	Triangles	4	
Mesh 5	Quads	66337	0.946246
	Triangles	12	

Table III. Mesh characteristics and convergence metrics for grid independence study

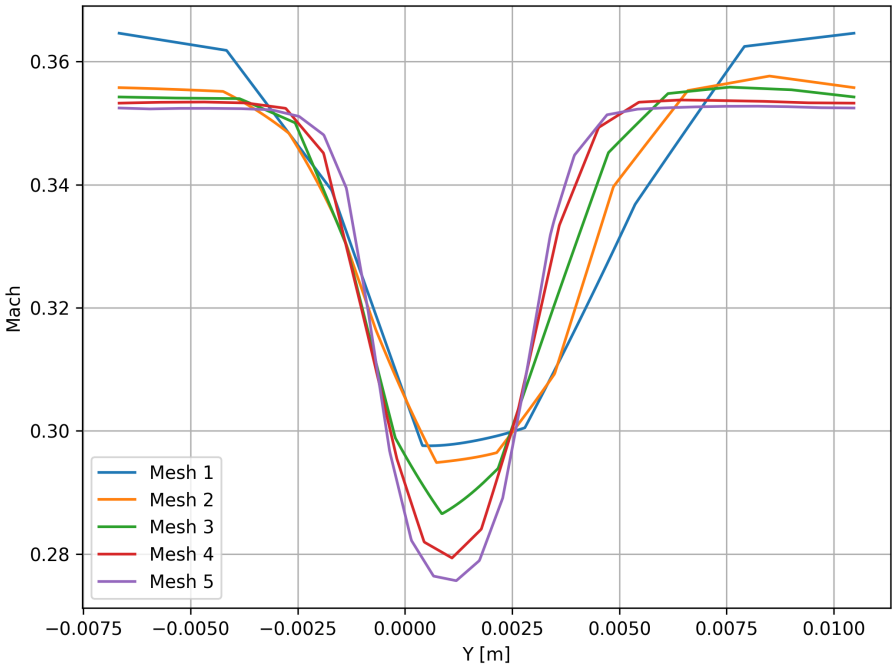

Figure 16. Mach number distribution across different mesh refinements

The obtained mesh is presented in Figure 17. It may be observed that the quality of the mesh at critical locations such as the boundary layer, the wake and the gap between the blades is still not good enough. Hence, it requires further improvement.

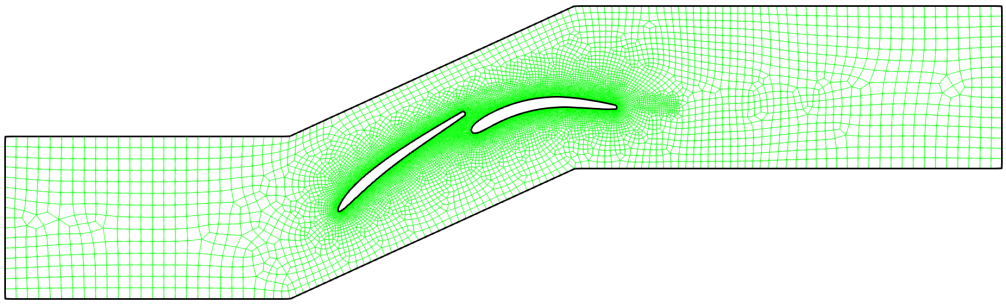

Figure 17. Obtained mesh after optimizing the number of cells

5.2.2 Boundary Layer and Wake Refinement

Proper resolution of the boundary layer is critical for accurate flow simulations. As it has been previously explained, achieving $y^+ \approx 1$ is ideal for resolving the viscous sublayer, with $y^+ < 5$ being the maximum acceptable value for high-fidelity simulations.

To obtain the desired values, the cells within the boundary layer and in the wake have been refined. In Figure 18, the final values of y^+ for the refined mesh are presented. It may be seen that most of the points have a $y^+ \approx 1$ being $y^+ \approx 2.6$ the highest one. Thus, validating the refinement of the mesh.

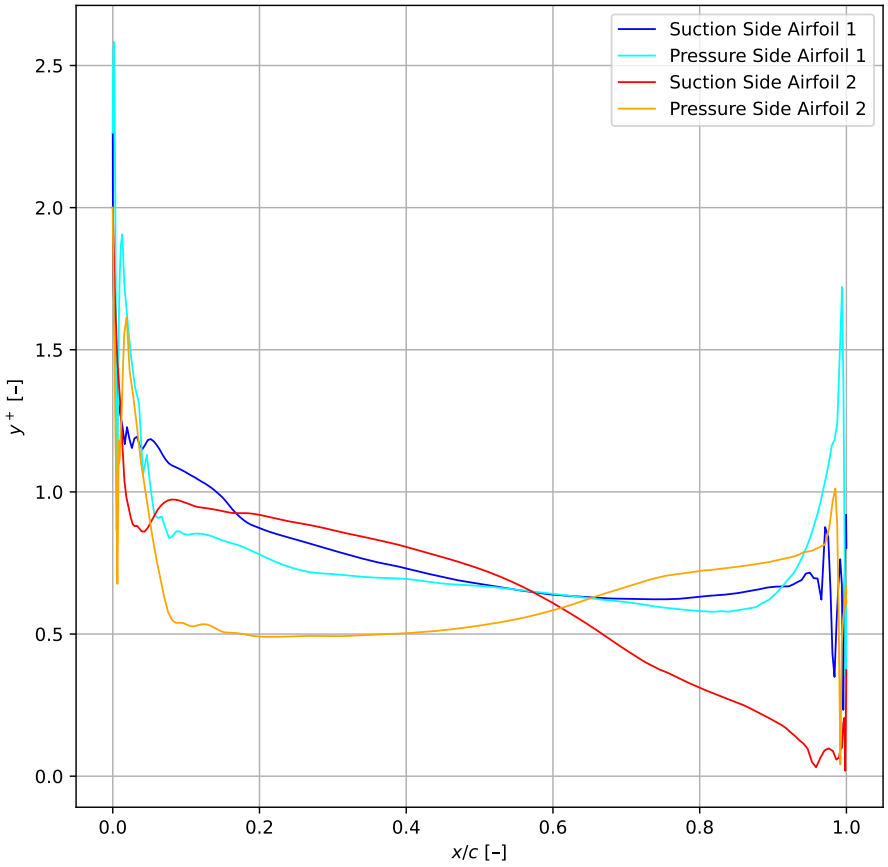

Figure 18. y^+ distribution across the tandem blades.

5.3 Final Mesh

The final mesh is presented in Figure 19. In Figure 20 a closeup view of the critical locations of the mesh is presented. It may be observed that the mesh at these locations is sufficiently refined.

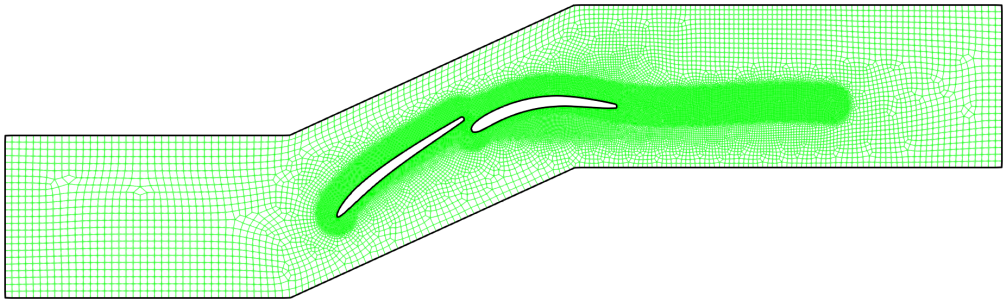

Figure 19. Final mesh

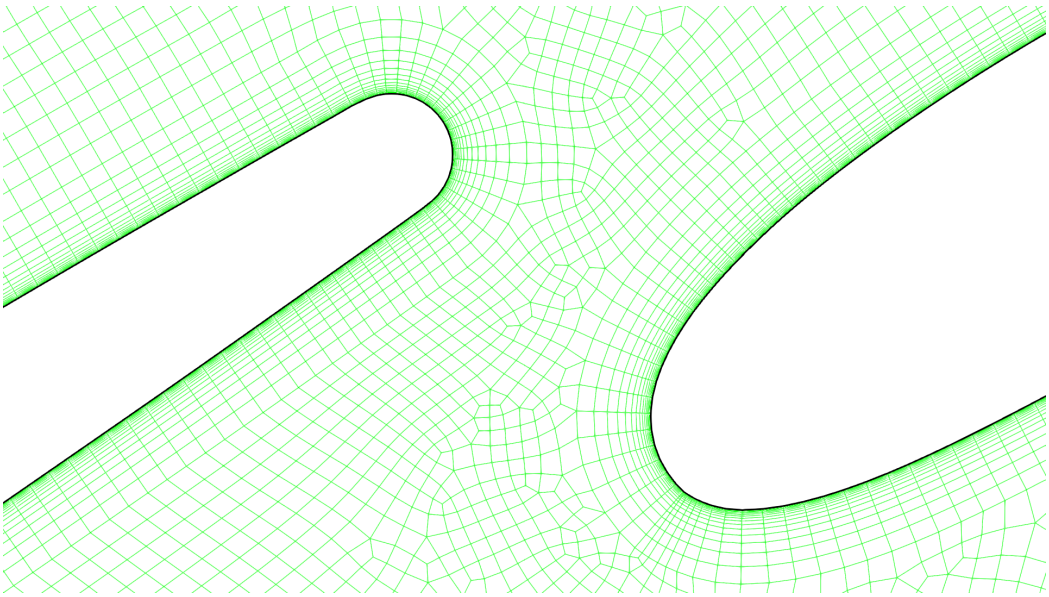

(a) Gap zoom

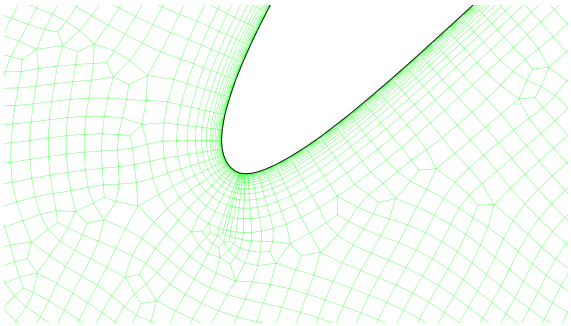

(b) Front Blade's Leading Edge zoom

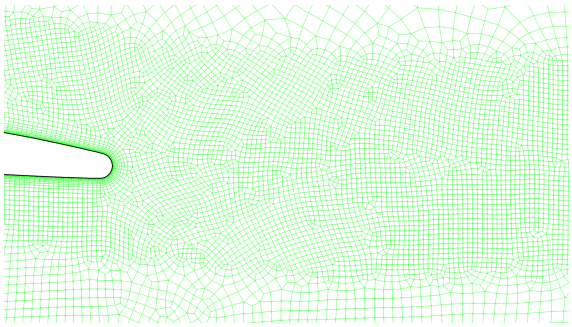

(c) Wake zoom

Figure 20. Zoomed mesh regions

The last step to determine the quality of the mesh has been to check some of its metrics. In Figure 21, the orthogonality of the mesh is presented. The orthogonality measures the angle deviation between adjacent cell faces from the ideal 90° configuration. Poor orthogonality may introduce discretization errors. In order not to have divergence, orthogonality should be higher than 10º and ideally of 20º [30]. Since the lowest values are in the order of 50º, the mesh is deemed acceptable.

In Figure 22, the aspect ratio of the mesh is shown. The aspect ratio represents the ratio of a cell's longest length to the shortest length usually, values of aspect ratio close to 1 are desired. However, higher values inside the boundary layer are accepted. It may be seen that most of the mesh has aspect ratios close to 1 outside the boundary layer. As expected, aspect ratios inside the boundary layer are higher, which in the current mesh can reach values up to 180.

Finally, the skewness is represented in Figure 23. The skewness represents the normalized distance between a line that connects two adjacent cell centroids and the distance from that line to the shared face's center. Hence, it should be kept as low as possible. For 2D, a skewness below 0.5 represents good quality. Since the skewness of the mesh is below 0.5 for most points and is close to 0 in both the boundary layer and the wake, it has been deemed that the quality of the mesh is acceptable.

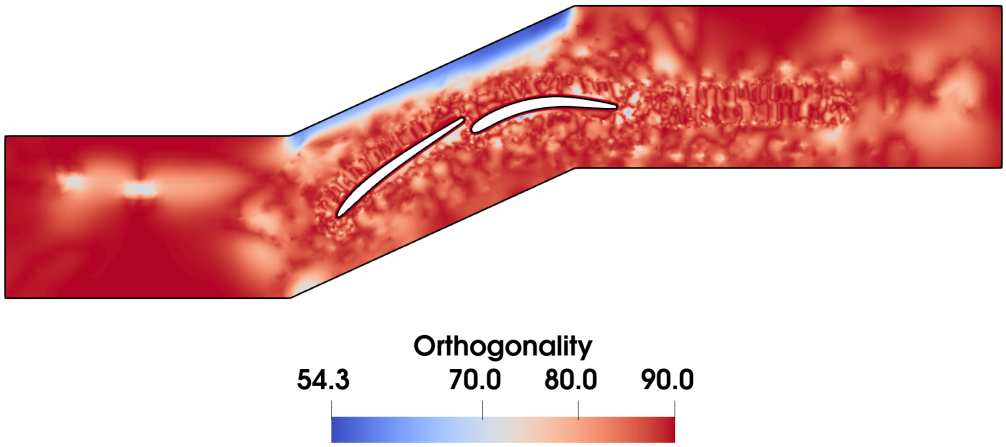

Figure 21. Orthogonality of the final mesh

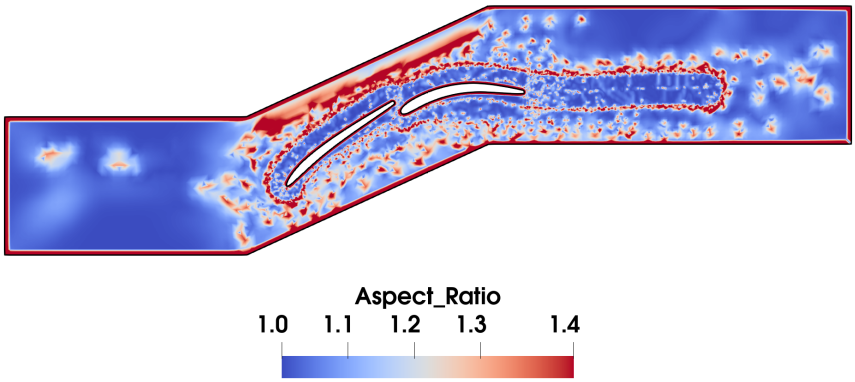

(a) Aspect ratio outside of the boundary layer

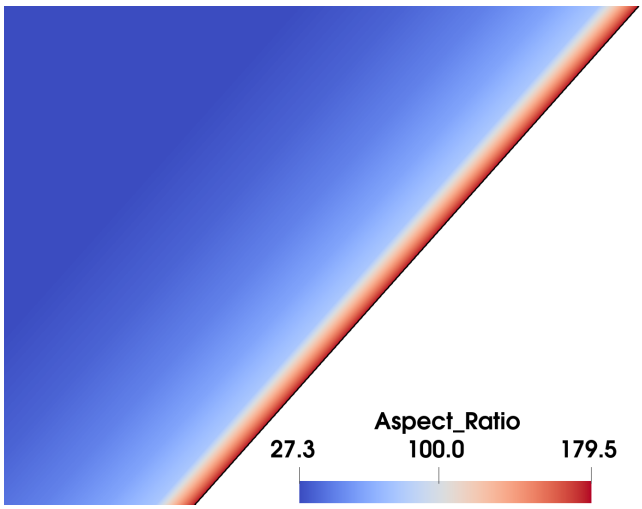

(b) Aspect ratio inside of the boundary layer

Figure 22. Aspect ratio of the final mesh

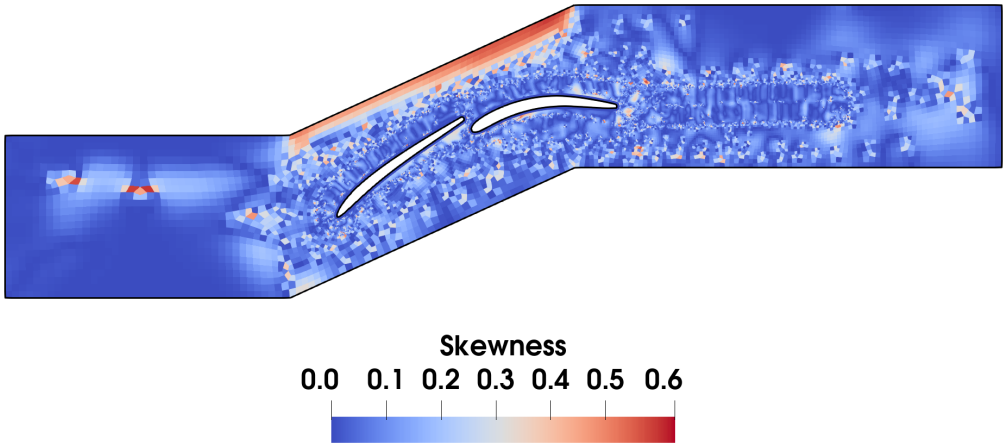

Figure 23. Skewness of the final mesh

5.4 CFD Settings

This section presents the setup that has been used to run the simulations.

The main CFD settings that have been set are described in Table IV:

Setting	Parameter	Value
Solver	Type	RANS
Turbulence	Model	SST
Viscosity	Model	Sutherland's Law
Flow	Reynolds Number	650,000
	Mach Number (inlet)	0.6
	Inlet Flow Angle	50°
Numerics	Gradient Scheme	Weighted Least Squares
	Flow Convective Scheme	ROE
	Turbulent Convective Scheme	Scalar Upwind
	CFL factor-down	0.1
	CFL factor-up	1.5
	CFL minimum value	1.0
	CFL maximum value	100
Convergence	Monitoring Field	Relative RMS density
	Residual Threshold	10^{-4}
	Max Iterations	10,000

Table IV. Main CFD settings for the simulation

5.4.1 Boundary Conditions

The boundary conditions set in Table V are defined using total properties at the inlet, specifying the flow direction along with total temperature and pressure. The outlet boundary is characterized solely by static pressure. Periodic conditions are applied to the upper and lower boundaries, ensuring flow continuity between the pressure and suction sides. A constant total temperature of 303 K at the inlet is maintained across all simulations.

The inlet Reynolds number is set to 650,000. Recall that the Reynolds number is defined in Equation 49 as:

$$Re = \frac{\rho u L}{\mu}$$

where the characteristic length has been set to be the total axial chord of the tandem blade since it would be the total chord for testing an equivalent single-blade configuration. However, since the configuration is a tandem blade, the boundary layer is reset at the front blade, so its chord could have been selected as well.

Additionally, the Mach number at the inlet is set to 0.6 for all simulations. To achieve the target inlet Mach number, the ratio between inlet total pressure and outlet static pressure is adjusted for each test case. This presents a significant challenge, as the actual Mach number of each configuration can only be determined after solving the flow field, requiring an iterative adjustment process whenever the geometry or inflow angle is modified.

Parameter	**Value**
Inlet Reynolds Number	650,000
Inlet Mach Number	0.6
Inlet Flow Angle	50°

Table V. Boundary conditions

5.5 Automatic Search Process of the Inlet Mach Number

The numerical implementation requires an iterative procedure to achieve the target inlet Mach number of $M = 0.6$ within a $\pm 1\%$ tolerance band ($0.594 \leq M \leq 0.606$).

1. The numerical procedure begins by setting the outlet pressure equal to the baseline value and running a first simulation.

2. After obtaining the initial solutions, the inlet Mach number M is evaluated for each case.

3. For cases where M falls outside the target range of 0.594 to 0.606, the outlet pressure is adjusted using the following modification rule:

$$P_{\text{out,new}} = \begin{cases} P_{\text{initial}} \cdot \left(1 + \left(\frac{M-0.6}{0.6}\right)^2\right) & \text{if } M > 0.606 \text{ (above target)} \\ P_{\text{initial}} \cdot \left(1 - \left(\frac{M-0.6}{0.6}\right)^2\right) & \text{if } M < 0.594 \text{ (below target)} \end{cases} \tag{59}$$

4. The previous steps are repeated with the updated pressure values.

5. If the new inlet Mach number is still outside of the target range, a secant method with adaptive relaxation is employed for precise convergence [31]. Beginning with the two initial points $(p^{(0)}, M^{(0)})$ and $(p^{(1)}, M^{(1)})$, the pressure update at each iteration $n+1$ follows:

$$P^{(n+1)} = P^{(n)} - \underbrace{\frac{P^{(n)} - P^{(n-1)}}{M^{(n)} - M^{(n-1)}}}_{\text{Secant slope}} M_{\text{res}}^{(n)} \tag{60}$$

   where $M_{\text{res}} = M_{\text{actual}} - M_{\text{target}}$ represents the Mach number residual at the inlet. This approach exhibits superlinear convergence with order $\phi \approx 1.618$ (the golden ratio), offering superior convergence characteristics compared to basic fixed-point iteration while avoiding the derivative calculations required by Newton-Raphson methods.

   For enhanced stability, the algorithm incorporates three key features:

   - A relaxation factor that reduces the step size when successive iterations sweep the solution.
   - Pressure bounds verification to prevent nonphysical states.
   - Automated termination and logging if the solution diverges or violates operational constraints.
   - Convergence check to ensure the quality of the output results.

   The relaxation mechanism proves particularly valuable when the local slope becomes excessively shallow, preventing the large pressure jumps that could otherwise trigger flow separation or divergence issues.

5.6 Averaging Procedure

As can be seen from Figure 16, the distribution of the flow parameters along the y-axis at any given location is not uniform. Since the curve is obtained from the Gmsh mesh, which is more refined near the wake region, a simple arithmetic averaging would overemphasize these regions, leading to results that do not accurately represent the underlying physics of the flow.

Four flow parameters are required in 2D to completely describe the flow conditions. Two surface averaging methods for non-uniform internal flows have been considered in this project:

- Mass flow averaging: Assumes near-incompressibility of the flow but does not work with conserved quantities. This method, which is the one that has been implemented in this work, has a simpler implementation and is commonly used in industry standards.

  By computing the surface average of the following quantities:

  - $\overline{\rho v_a}$
  - $\overline{\rho v_a P^\circ}$
  - $\overline{\rho v_a T^\circ}$
  - $\overline{\rho v_a^2}$
  - $\overline{\rho v_a v_u}$
  - $\overline{P}$

  where ρ is the density, v_a the axial velocity, v_u the radial velocity, P the static pressure, P^o the total pressure and T^o the total temperature.

  The average flow quantities are then derived as follows:

  - $P^\circ = \frac{\overline{\rho v_a P^\circ}}{\overline{\rho v_a}}$
  - $T^\circ = \frac{\overline{\rho v_a T^\circ}}{\overline{\rho v_a}}$
  - $v_a = \frac{\overline{\rho v_a^2}}{\overline{\rho v_a}}$
  - $v_u = \frac{\overline{\rho v_a v_u}}{\overline{\rho v_a}}$

  From these averaged parameters, the remaining flow quantities can be computed. However, since the static pressures have had a separate averaging, this procedure is not fully consistent.

- Flux averaging: This method captures the physics of the flow more accurately, but tends to overestimate entropy and losses, resulting in a pessimistic performance prediction. It operates on conserved quantities and requires an iterative procedure. This approach consists of integrating the fluxes and finding a uniform flow state with an identical overall flux [32].

  The surface averages of the following quantities are computed:

  - $\overline{\rho v_a}$
  - $\overline{\rho v_a^2} + \overline{P}$
  - $\overline{\rho v_a v_u}$
  - $\overline{\rho v_a h^\circ}$

where h^o is the total enthalpy.

Unlike mass flow averaging, this approach requires an iterative computation:

1. Make an initial guess for the average axial velocity.
2. Compute the average pressure.
3. Solve for the remaining flow quantities until a new axial velocity is obtained.
4. Iterate until the axial velocity converges within a specified tolerance.

6 Results

In this section, the results obtained in this work will be presented. First, an analysis of the impact of the defining parameters of the geometry on the performance of the tandem blade shall be performed. Once the impact of the governing parameters is understood, the optimization results obtained using Minamo will be presented.

6.1 Relative Position

The first study analyses the impact of altering the relative position of the tandem blades on the overall performance. It is difficult to analyze the results of this study by itself. However, it has been the foundational work for the rest of the optimization workflow. Thus, the results will be presented below.

Two approaches to quantify the performance have been considered:

- Pressure losses.
- Working range.

For the first approach, the pressure losses for the reference inlet flow angle (IFA) of 50º have been minimized. For the second approach, the working range has been defined as the range where the losses are within two times those of the reference inlet flow angle. The losses at the reference IFA have been constrained so that they should not surpass those of the baseline configuration +20%.

Recall that the losses at any given inlet flow angle are defined in Equation 26 as:

$$\phi = \frac{P_i^\circ - P_e^\circ}{P_i^\circ - P_i}$$

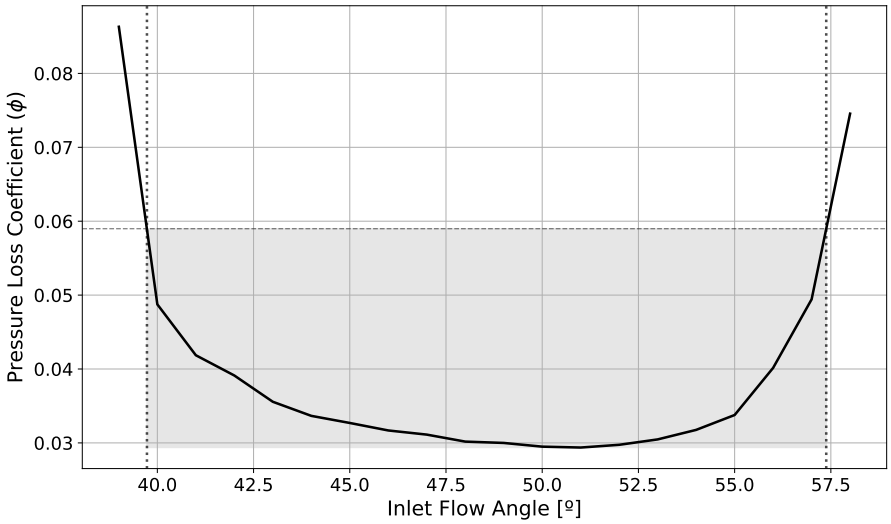

Figure 24. Loss coefficient polar of the baseline configuration

In this first study, the AO, the x position of the RB's TE and the total axial chord of the tandem blade were fixed. The PP has been the only modified parameter. In other words, the solidity of the tandem blade has been fixed. In both cases, the exit flow angle has been monitored to check that it was within $\pm 1^{\circ}$ for the reference IFA.

For the study, PPs between 0.85 and 0.95 have been selected. Figure 25 shows the variations in the geometry across the selected range.

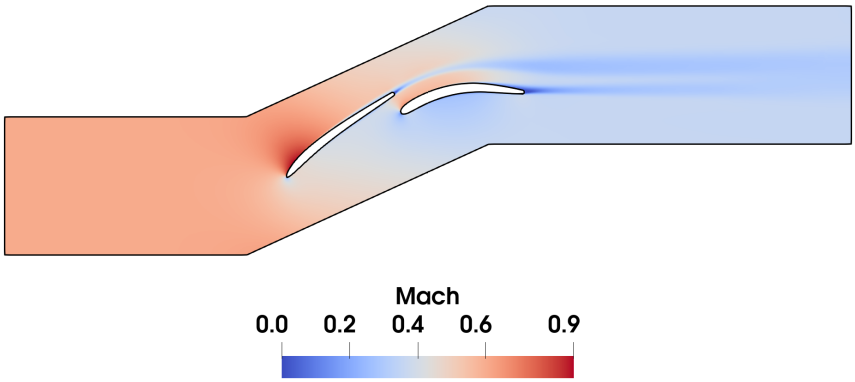

(a) Geometry at Percentage Pitch (PP) = 0.85

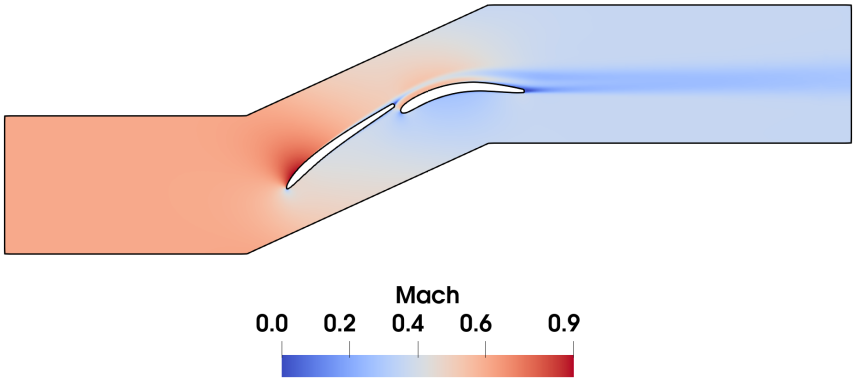

(b) Geometry at Percentage Pitch (PP) = 0.95

Figure 25. Influence of PP on the geometry of the tandem blade

Figure 26 shows the results of the study.

- On-design (50º) ϕ is reduced when going towards higher PPs.
- The exit flow angle increases when going towards higher PPs.
- The working range increases as PP decreases.

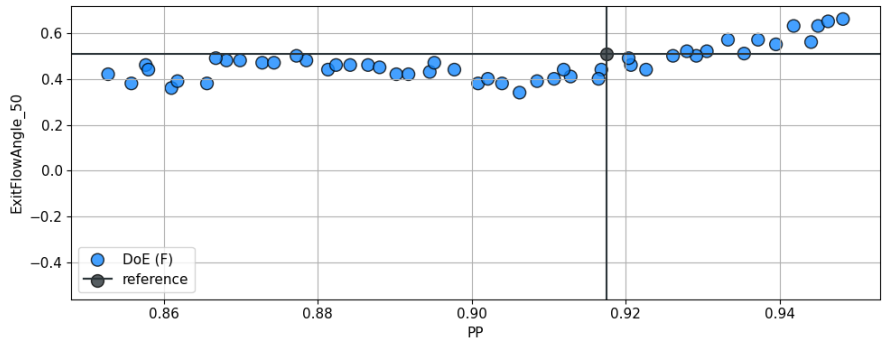

(a) Exit Flow Angle [°] in terms of PP for IFA of 50°

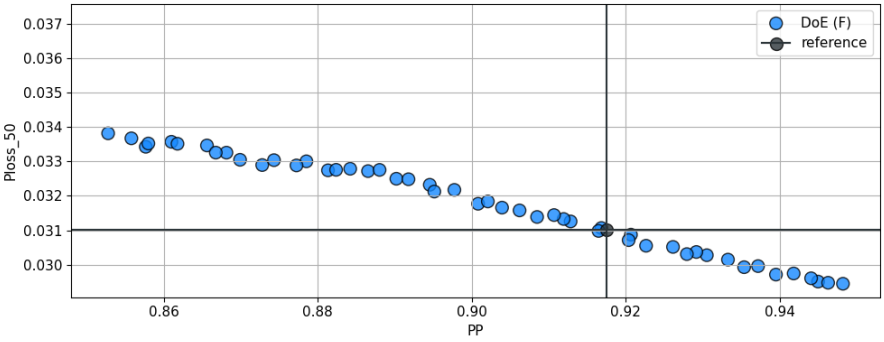

(b) ϕ in terms of PP for IFA of 50°

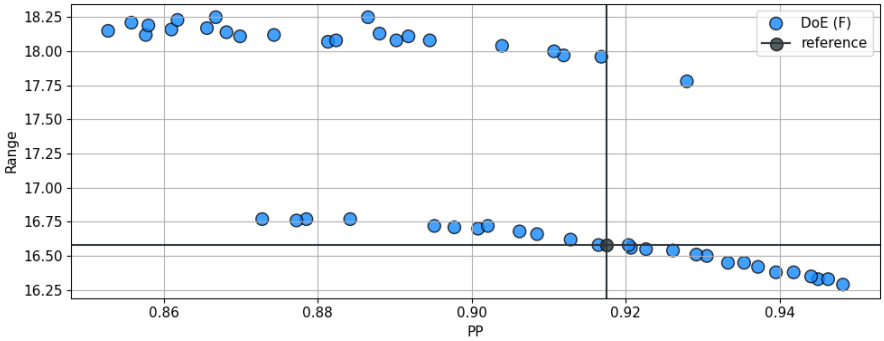

(c) Range in terms of PP

Figure 26. Effect of percentage pitch on flow physics

Preliminary results show that higher PPs tend to improve the performance of the tandem blades. However, this comes at the cost of having a less axial flow. Thus, a trade-off must be done. From the previous results, it may be inferred that it is likely that the optimal PP will be found around PP = 0.85 - 0.95.

On the other hand, lower PPs tend to output a higher working range. It may be appreciated from Figure 26c that the working range is highly fluctuating in terms of PP. This is because

the configurations with positive incidence (inlet flow angle > 50º) are prone not to reach the convergence criteria set in the SU2 simulations or to diverge. In these cases, the working range can't be computed in its entirety because the available point with the highest pressure loss in the positive incidence side won't reach the target ϕ of two times that of the on-design. This effectively reduces the working range, which further increases the complexity of the problem.

A convergence analysis has been performed and it has been concluded that this problem is likely due to the fixed CFL number parameterization in the SU2 configuration file, which had initially been fixed to a maximum number of 500. The CFL number is one of the main parameters that control the convergence rate of the scheme. If it's not defined correctly, two main problems may arise:

- Too large CFL number: In this case, the residual of the monitored field starts oscillating and never converges, until the maximum number of iterations is reached and the simulation stops without convergence.
- Too low CFL number: In this case, the convergence rate is so slow that the maximum number of iterations is reached before convergence and the simulation stops.

It has been found empirically that by setting a maximum CFL number of 100, the obtained results were more consistent across different configurations. However, this fixed value has not been well suited for all problems, causing the lack of some potentially good results. Additionally, some configurations/conditions lead to unsteady flow which causes the simulation not to converge regardless of the implemented CFL strategy.

Another issue that has been found is that some configurations diverged at some inlet flow angles. This problem is likely due to the automatic mesh processing, which hasn't been optimized across all configurations. Some quality checks have been implemented in the optimization workflow to ensure consistent results, but still, this hasn't been enough for some configurations.

The main quality checks for the mesh generation are listed below:

- Check that the blades do not crash so that the mesh may be generated correctly.
- Perform a simulation with SU2 with a single iteration to check that the mesh has been correctly generated.
- In the event of a successful mesh, it has been checked that the minimum orthogonality was above 10º.

The previous quality checks along with the convergence criteria for the SU2 simulations described in Table IV have ensured quality results across different configurations.

6.2 Blade Shape Modification

The second study analyzes the impact of altering the shape of each blade independently and how it affects the overall performance using the same performance criteria as the previous study.

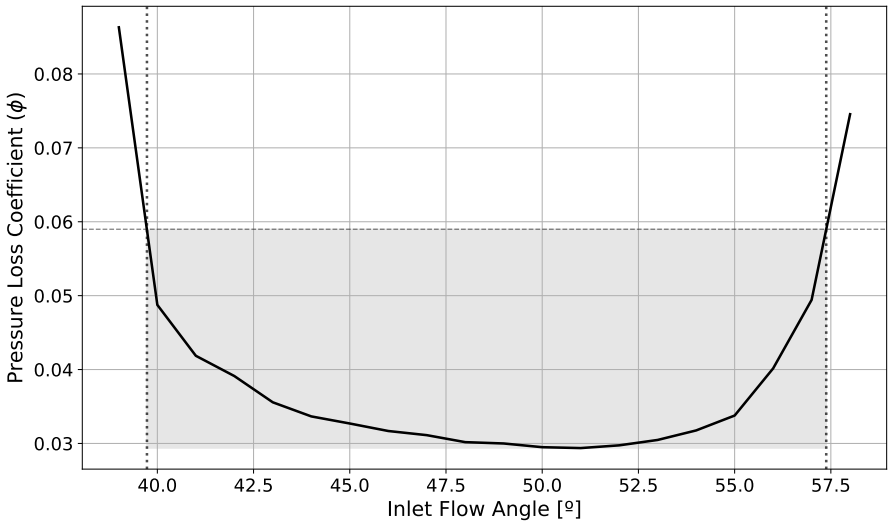

Figure 27. Loss coefficient polar of the baseline configuration

In this second study, the PP has been fixed to that of the original configuration. The AO has been an output of the considered configuration. The geometry of each blade has been modified using the 6 parameters that define it using the camberline and thickness distribution. The impact that these parameters have on the geometry is displayed in the following Figures, where the modifications of the FB's shape may be observed. The modifications of the RB's shape may be checked in Appendix 9.2 as well as the results of the study.

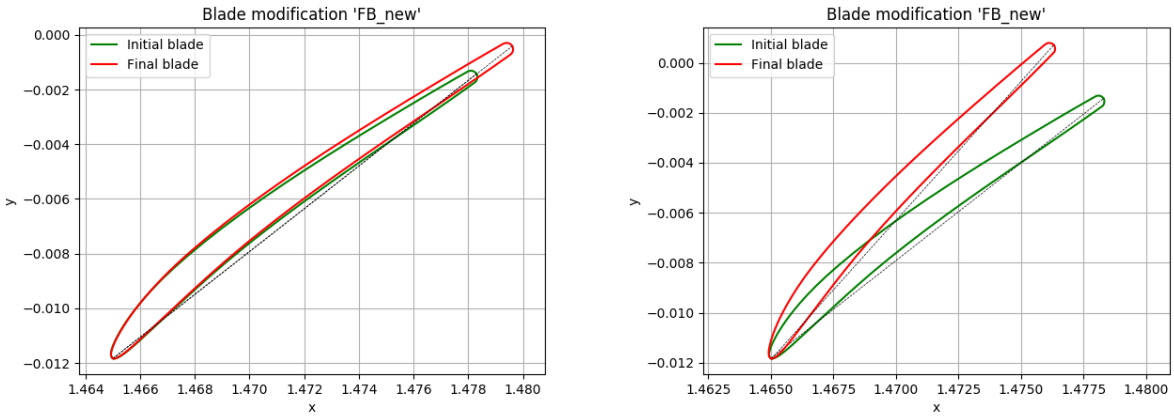

(a) FB comparison with +10% Chord Length

(b) FB comparison with +10º Stagger Angle

Figure 28. Front blade shape modifications [1]

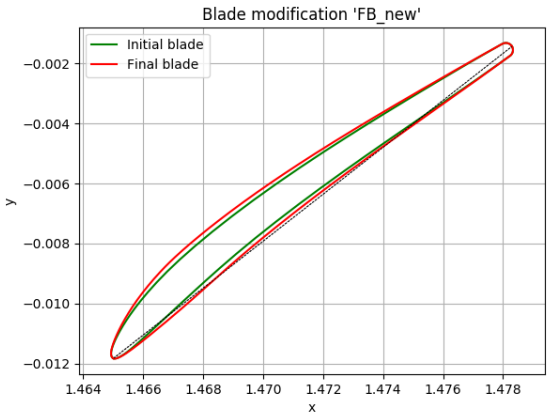

(a) FB comparison with +30% Thickness

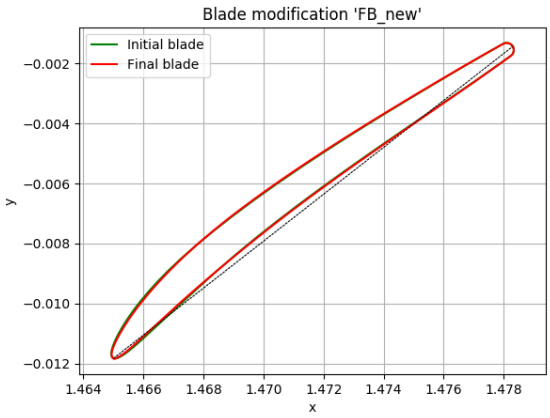

(b) FB comparison with +10% Thickness Shift

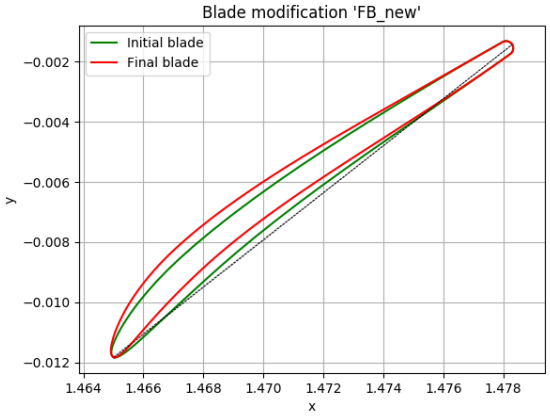

(c) FB comparison with +10º Metal Angle at LE

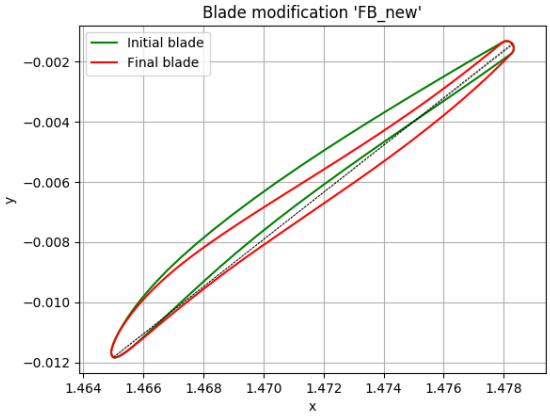

(d) FB comparison with +10º Metal Angle at TE

Figure 29. Front blade shape modifications [2]

In Figure 30, the influence of each of the defining parameters of the geometry on the flow physics is represented. Note that the thickness scale and the thickness shift do not have a major influence on any of the monitored parameters, thus they are deemed unnecessary for the optimization process.

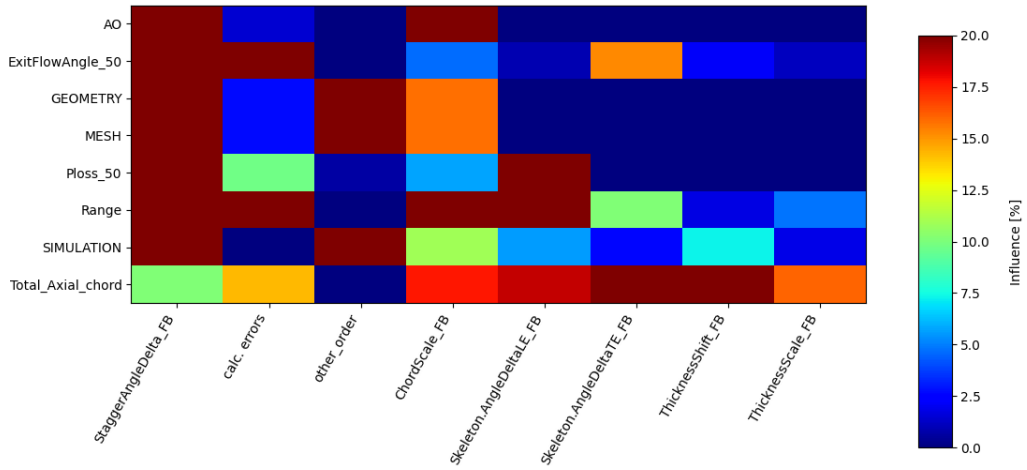

Figure 30. Global Sensitivity Analysis (GSA) on front blade

The analysis performed on the FB and the RB (see the study in Appendix 9.2) has shown that the following parameters did not have a major impact on the output, thus they have been deemed unnecessary for performing the optimization:

- Thickness shift of both blades.
- Thickness scaling of both blades.

6.3 Performance Optimization

The first approach that has been considered for optimizing the OGV is to improve the on-design performance of the tandem blades. In other words, the goal of this optimization was to reduce the pressure losses for the reference inlet flow angle of 50º, while keeping the off-design pressure losses within an acceptable margin when compared to the baseline configuration.

6.3.1 Optimization Considerations

The optimization process incorporated several key constraints and considerations:

- Primary Objective: Minimize pressure losses at the design point (50° inlet flow angle).
- Off-Design Performance: Limit loss increase to +20% compared to baseline at off-design conditions.
- Geometric Constraints:
  - Fixed total axial chord length (space limitations and blade loading considerations).
  - Fixed trailing edge position of the rear blade at x=1.51 (maintains consistent downstream spacing).
  - Controlled exit flow angle variation: ±0.5° tolerance and ±1° critical tolerance.

The off-design analysis focused on two operating points:

- 45° inlet flow angle (-5° from design).
- 55° inlet flow angle (+5° from design).

In Figure 31, the polar of the baseline configuration is represented. This optimization aims to reduce the losses at the reference inlet flow angle (minimum point) while keeping the working range (shaded area) within a certain margin.

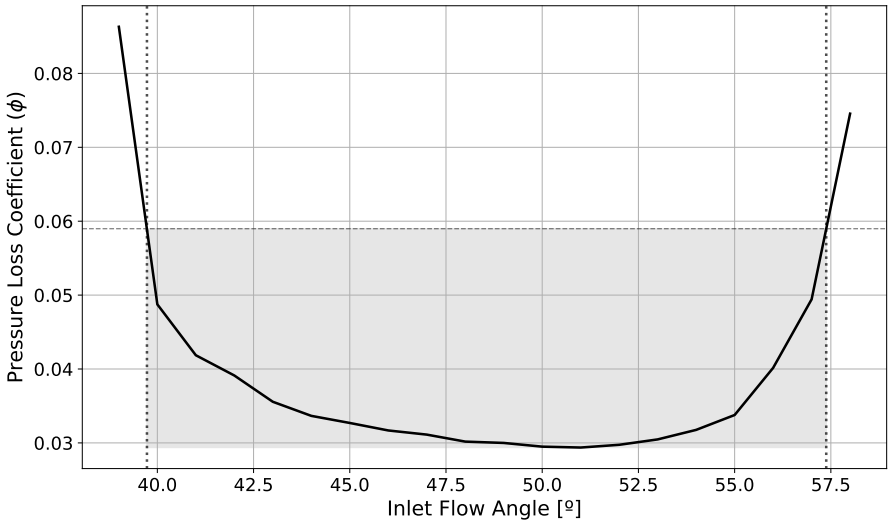

Figure 31. Objective loss coefficient polar

All three configurations (design point plus both off-design conditions) were evaluated in parallel to speed up the numerical processing.

6.3.2 Performance Comparison

In this section, an overview of the main quantities that describe the performance of the OGV shall be presented.

The specifications of the optimized geometry are summarized in Table VI. The impact of these parameters on the final geometry may be observed in Figure 32. It may be noticed that the optimized tandem blade configuration has a sharper turning of the flow. Furthermore, the axial gap between the blades has been slightly reduced while the radial spacing has increased.

Variable	Symbol	Value	Units
Axial Overlap	AO	-2.58	%
Percentage Pitch	PP	93.24	%
Total axial chord	$C_{x,\text{total}}$	0.0294	m
Chord scaling (Front Blade)	$\text{ChordScale}_{\text{FB}}$	1.0392	–
Stagger angle delta (Front Blade)	$\Delta\beta_{\text{FB}}$	-1.587	º
LE angle delta (Front Blade)	$\Delta\theta_{\text{LE,FB}}$	2.5	º
TE angle delta (Front Blade)	$\Delta\theta_{\text{TE,FB}}$	-1.095	º
Chord scaling (Rear Blade)	$\text{ChordScale}_{\text{RB}}$	0.9567	–
Stagger angle delta (Rear Blade)	$\Delta\beta_{\text{RB}}$	-0.864	º
LE angle delta (Rear Blade)	$\Delta\theta_{\text{LE,RB}}$	-0.896	º
TE angle delta (Rear Blade)	$\Delta\theta_{\text{TE,RB}}$	1.067	º

Table VI. Geometric and design parameters used in the blade configuration

The performance optimization has successfully reduced the pressure losses by about 11%. This, however, has come at the cost of a slight reduction to the working range. Additionally, the absolute value of the exit flow angle has been further reduced, ensuring axial flow on-design, which is a critical operating point for the OGV. As before, the bounds for the working range have been defined as the region where the losses are within two times those of the reference inlet flow angle of 50º.

Parameter	**Baseline**	**Optimized**	**Difference [%]**	**Units**
Pressure Loss Coefficient (ϕ) at 50º	0.0295	0.0262	11.19	-
Exit Flow Angle	0.38	0.24	36.84	º
Lower bound	39.73	40.28	5.36	º
Upper bound	57.38	56.86	7.05	º
Range	17.65	16.58	6.07	º

Table VII. Comparison of aerodynamic parameters between baseline and optimized configurations. Differences in lower and upper bounds are normalized with respect to their distance from 50º inlet flow angle.

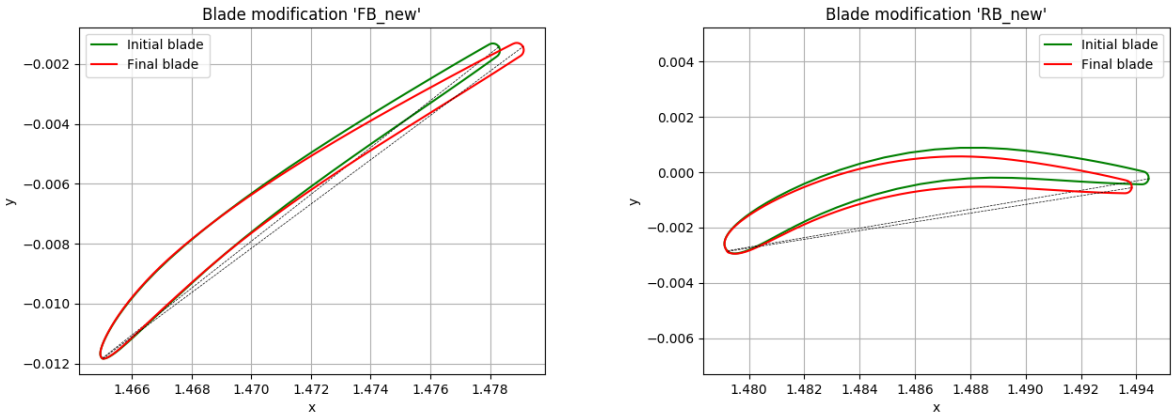

(a) FB comparison

(b) RB comparison

Figure 32. Comparison between the geometries of the baseline and optimized configurations

In Figure 33, the polars of the baseline and optimized configurations are represented. It may be noticed that the overall tendency of both cases is fairly similar. However, the pressure losses at the outer sections of the polar of the optimized configuration tend to increase more rapidly than those of the baseline one. As expected, this behavior is the cause for the slight reduction of the working range. The shaded region of the plot corresponds to the working ranges of both configurations, respectively.

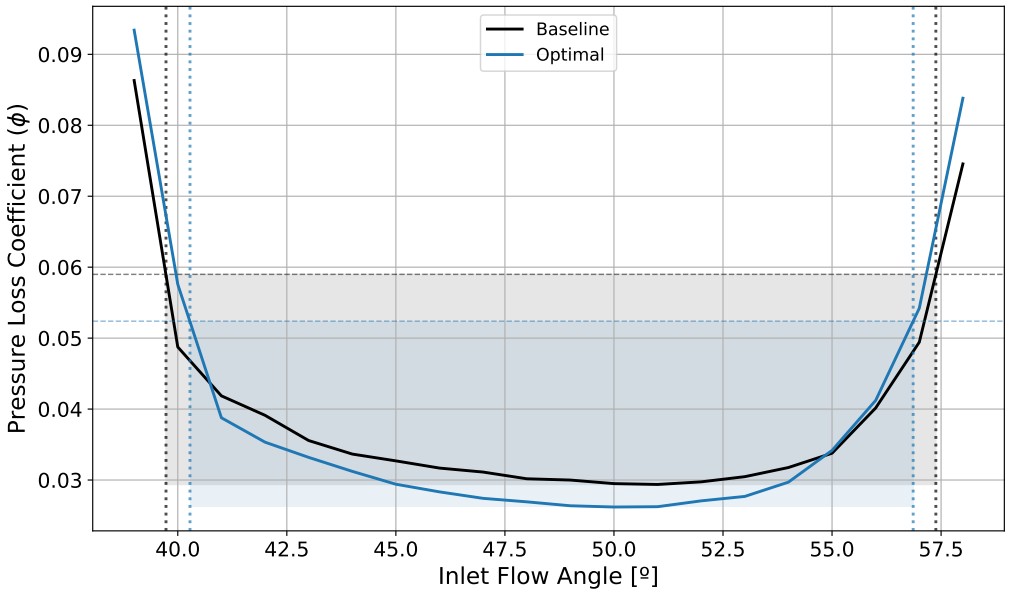

Figure 33. Comparison between the polars of the baseline and optimized configurations

In Figure 34, the pressure rise evolution of the baseline and optimized configurations are represented. Since the goal of compressors is to achieve high compression ratios, and tandem configurations are particularly interesting for high loadings, high work coefficients and low flow coefficients near surge limit, the right section of the graph becomes particularly interesting. However, unlike negative incidence, which presents a rather smooth curve, the shape of the curve at high inlet flow angles presents a maximum, which indicates stalled conditions. Reducing the mass flow by increasing the inlet flow angle beyond this point, results in a diminished pressure rise. Additionally, it may be appreciated that the overall pressure ratio of both configurations are similar.

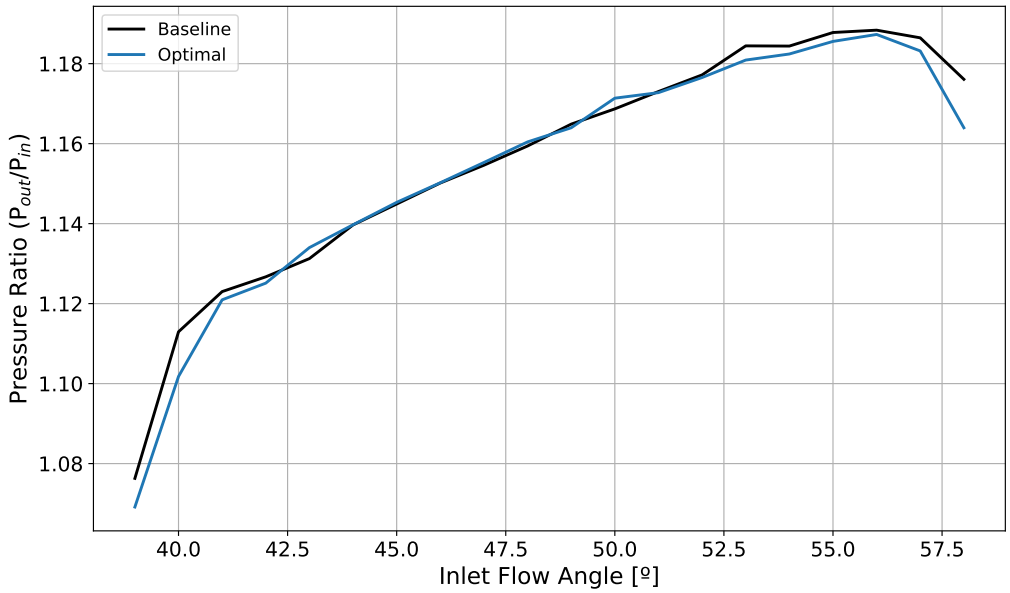

Figure 34. Comparison between the pressure ratio evolution of the baseline and optimized configurations

Finally, in Figure 35, the exit flow angle is represented in terms of the inlet flow angle. Both configurations keep an axial flow within $\pm 1^{\circ}$ for most of their working range. However, in the outer sections, the turning capabilities of the tandem blades are not enough to keep an axial flow.

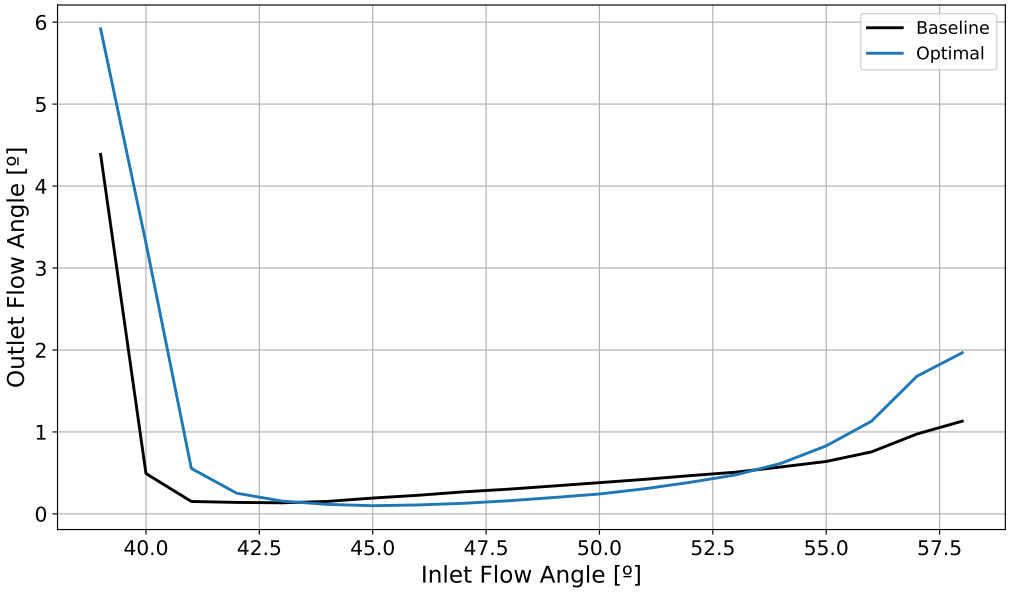

Figure 35. Comparison between the exit flow angle evolution of the baseline and optimized configurations

6.3.3 Blade Analysis

In this section, an analysis on the flow quantities on the surface of the blades is presented. In Figure 36, it may be appreciated that, as expected, the pressure coefficient of both suction sides

is lower than their pressure side, respectively.

The pressure distributions are fairly similar for both configurations. Moreover, the loading of the FB for inlet flow angles above 50º is higher than that of the RB. The inverse happens at low inlet flow angles.

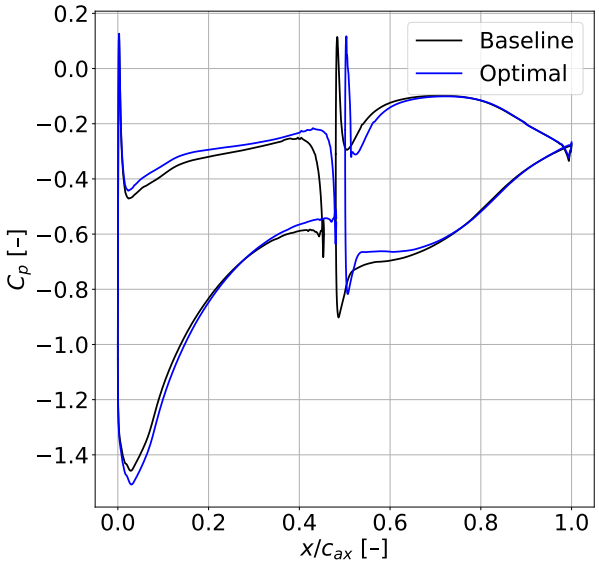

(a) Inlet flow angle of 50º

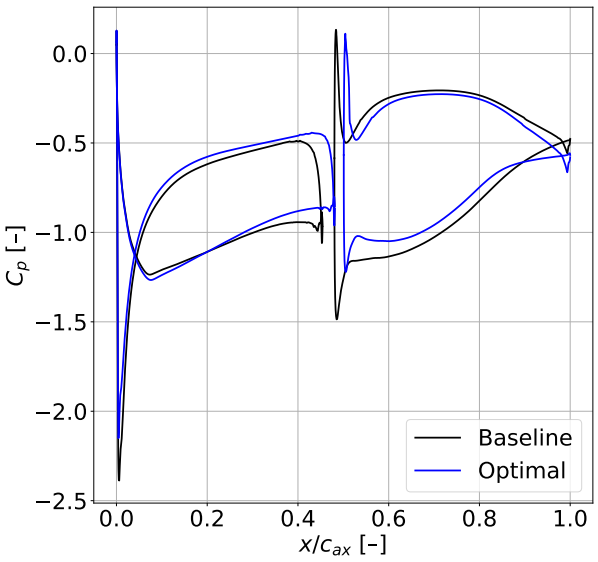

(b) Inlet flow angle of 40º

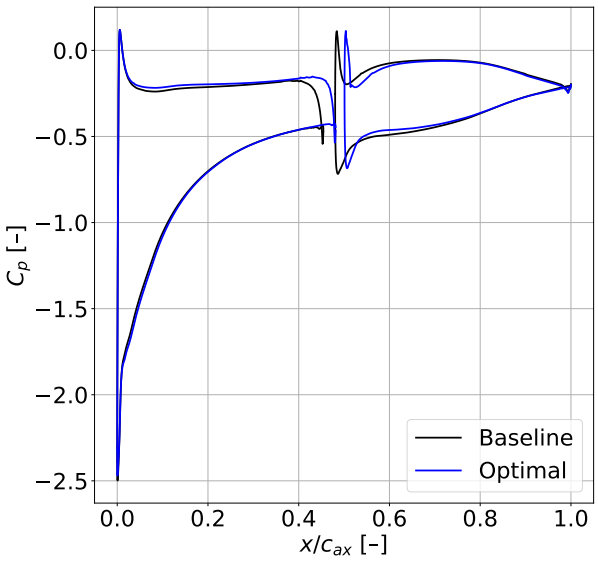

(c) Inlet flow angle of 56º

Figure 36. Comparison between the pressure coefficient distributions of the baseline and optimized configurations

6.3.4 Flow Visualization

In Figure 37, the Mach number distributions along the flow have been represented for several inlet flow angles. It may be appreciated that there is a significant difference between the Mach number upstream and downstream of the flow, which indicates a large deceleration of the flow throughout the stage. Additionally, the wake of the optimized configuration at 50º is thinner than that of the baseline. However, the wake of the off-design configurations is more severe. Moreover, for high inlet flow angles, the flow detaches from the front blade regardless of the configuration.

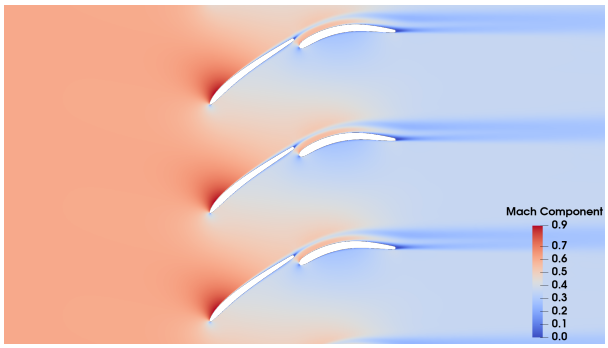

(a) Baseline at inlet flow angle of 50º

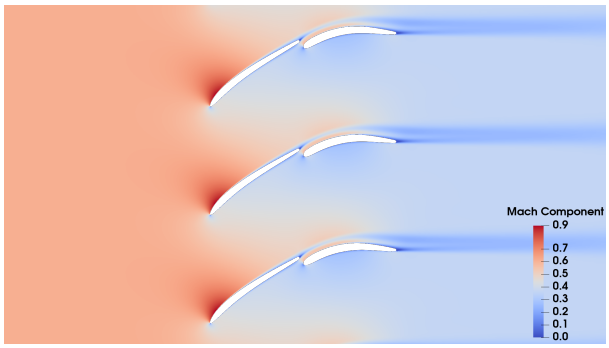

(b) Optimized at inlet flow angle of 50º

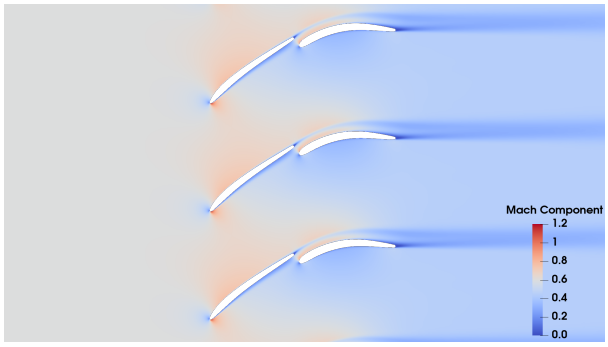

(c) Baseline at inlet flow angle of 40º

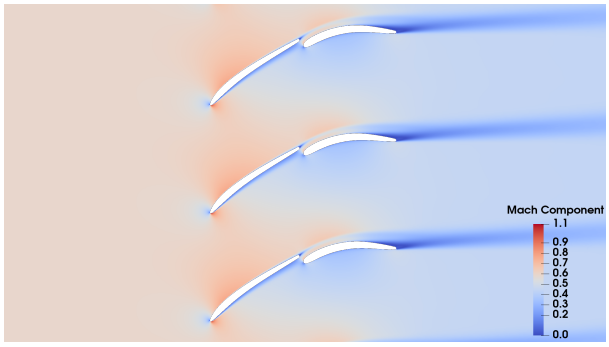

(d) Optimized at inlet flow angle of 40º

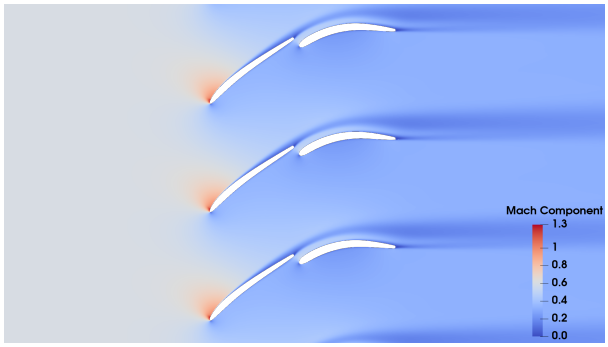

(e) Baseline at inlet flow angle of 56º

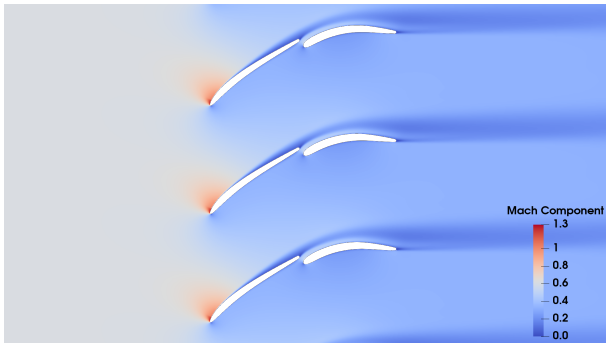

(f) Optimized at inlet flow angle of 56º

Figure 37. Comparison between the Mach distributions of the flow of the baseline and the optimized configurations at on-design, high and low inlet flow angles

In Figure 38, the pressure distributions over the flow are represented for both configurations. In this case, the pressure downstream is far greater than upstream. It is interesting to note that while the tandem blade compresses the flow, as expected, there is a significant drop on the pressure on the LE of the FB.

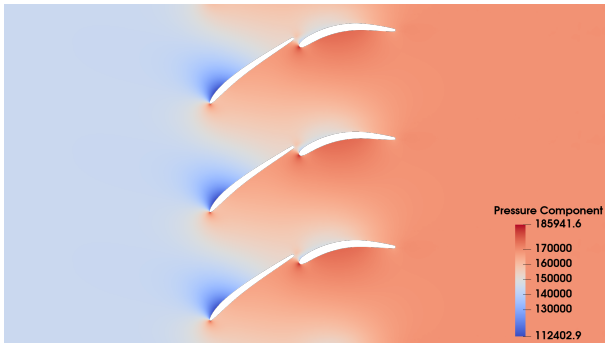

(a) Baseline at inlet flow angle of 50º

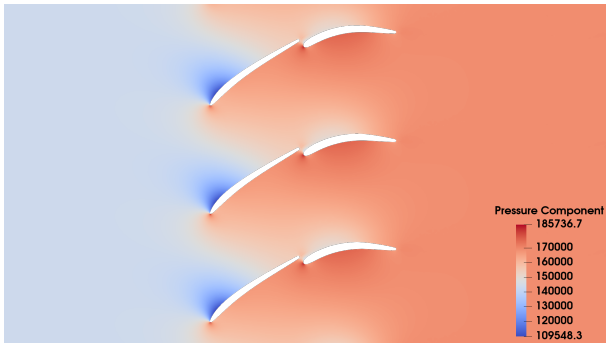

(b) Optimized at inlet flow angle of 50º

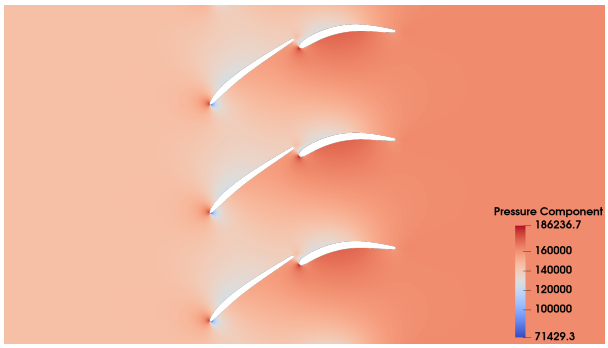

(c) Baseline at inlet flow angle of 40º

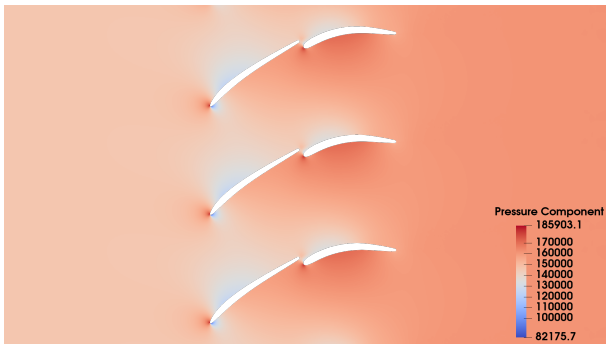

(d) Optimized at inlet flow angle of 40º

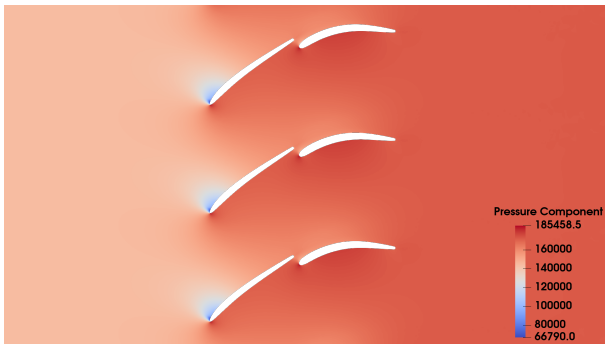

(e) Baseline at inlet flow angle of 56º

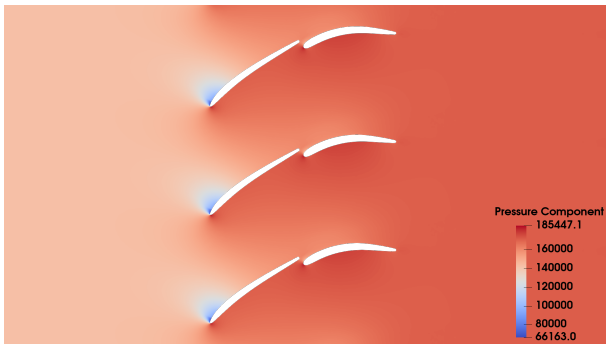

(f) Optimized at inlet flow angle of 56º

Figure 38. Comparison between the pressure distributions of the flow of the baseline and the optimized configurations at on-design, high and low inlet flow angles

In Figure 39, the evolution of flow quantities along streamlines over the flow for both configurations is represented. Both configurations present a similar behavior. Additionally, a clearer understanding of the pressure rise over the flow is presented. As it has been mentioned previously, the optimized configuration has achieved a more axial flow at the exit, which is a critical aspect for the OGV.

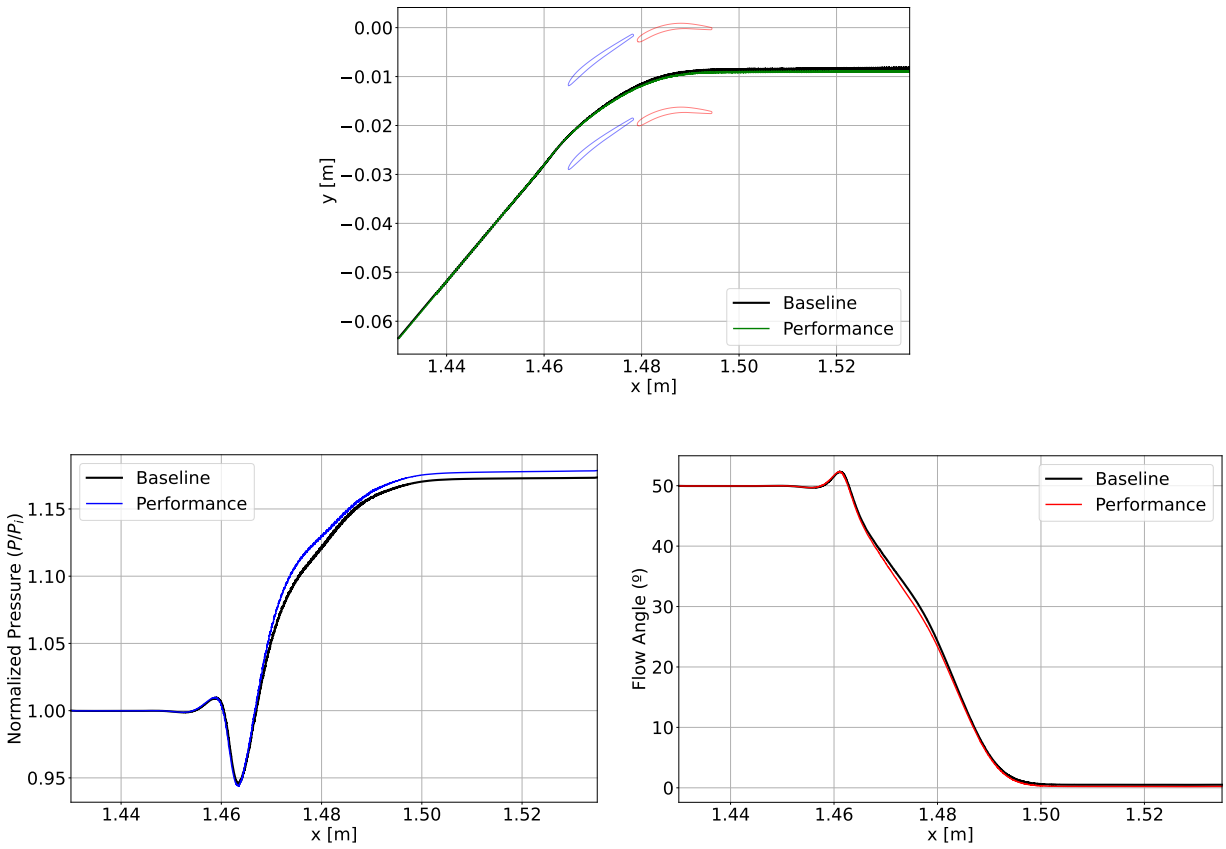

Figure 39. Comparison of the flow quantities represented over streamlines at inlet flow angle of 50º

6.3.5 Wake Analysis

In Figure 40 the pressure loss distribution at the MP2 point is presented. Similar conclusions to the previous Figures can be drawn. The optimized configuration presents a thinner and smoother, but more severe wake. However, this is enough to reduce the overall pressure losses of the flow for the reference inlet flow angle while keeping the off-design losses within an acceptable margin.

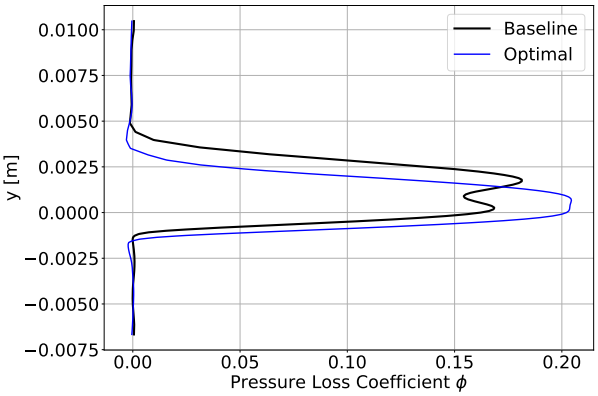

(a) Inlet flow angle of 50º

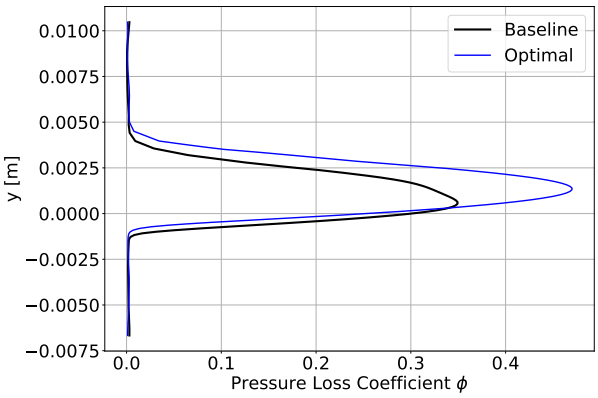

(b) Inlet flow angle of 40º

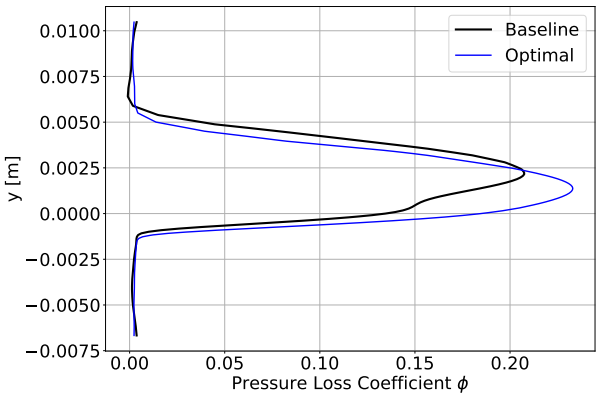

(c) Inlet flow angle of 56º

Figure 40. Comparison between the pressure loss distributions at x = 1.51 of the flow of the baseline and optimized configurations

In Figure 41, the exit flow angle distributions at the MP2 point are represented. A high fluctuation of the flow angle is presented in the wake region, meaning that the wake is highly turbulent.

While the flow is kept within the $\pm 1^{\circ}$ range for the baseline configuration across all inlet flow angles, this is only true at the reference inlet flow angle for the optimized configuration.

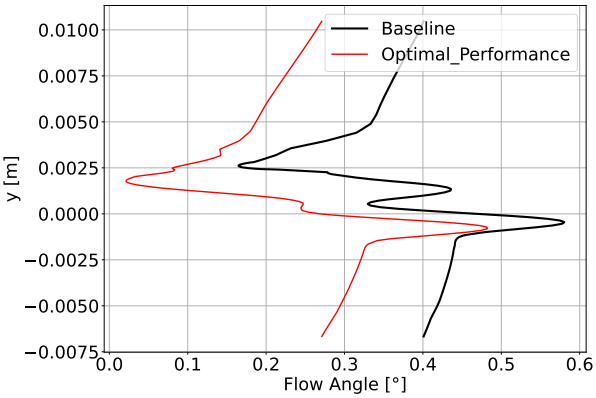

(a) Inlet flow angle of 50º

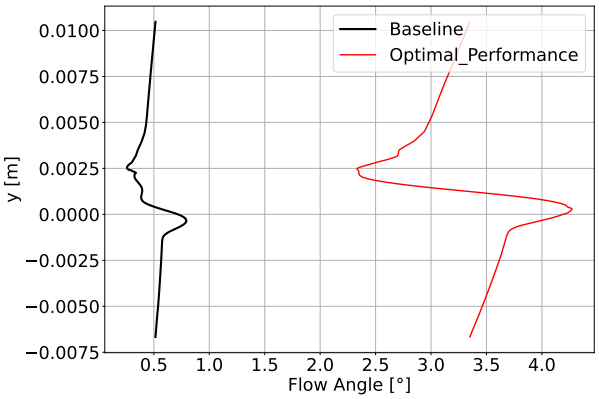

(b) Inlet flow angle of 40º

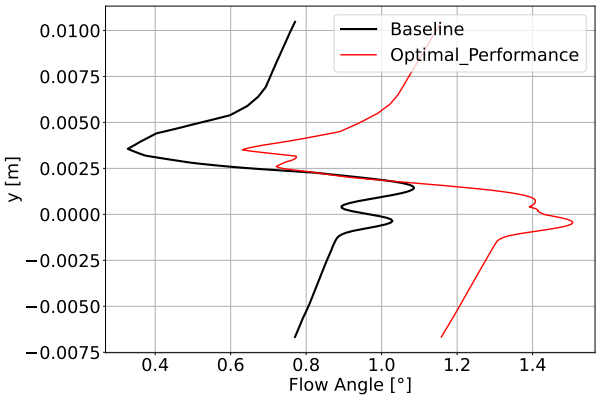

(c) Inlet flow angle of 56º

Figure 41. Comparison between the exit flow angle distributions at x = 1.51 of the baseline and optimized configurations

6.3.6 Turbulence Analysis

In Figure 42 the turbulent kinetic energy of both configurations is presented. The optimized configuration presents a slightly reduced turbulent region. Additionally, the rear blade of the baseline configuration at 50º presents a highly turbulent zone very close to the TE that is not present for the optimized configuration.

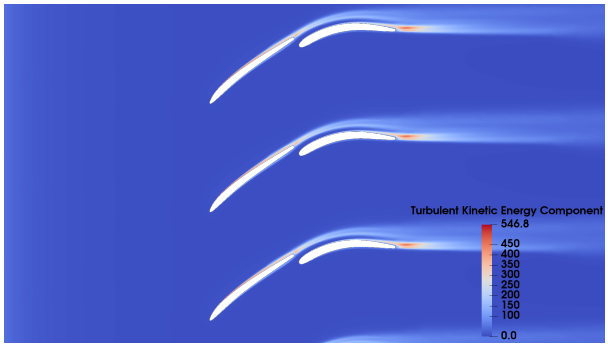

(a) Baseline at inlet flow angle of 50º

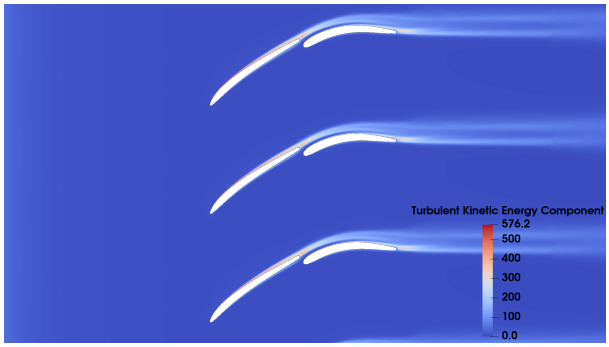

(b) Optimized at inlet flow angle of 50º

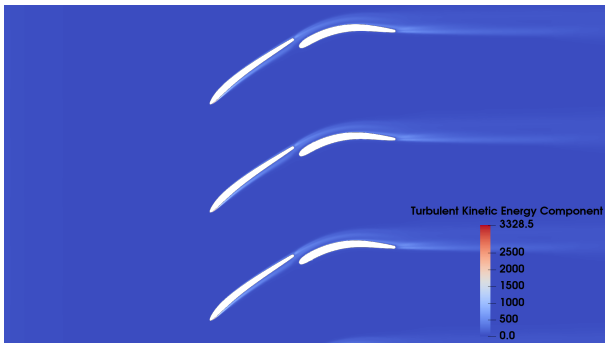

(c) Baseline at inlet flow angle of 40º

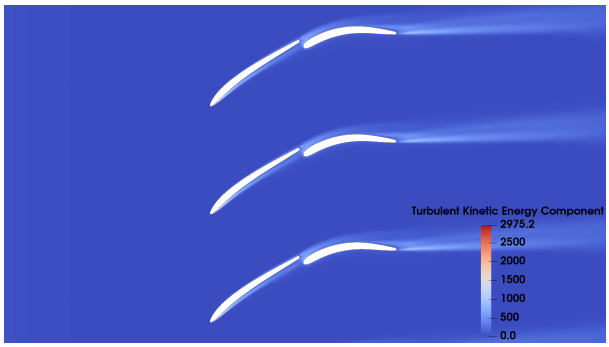

(d) Optimized at inlet flow angle of 40º

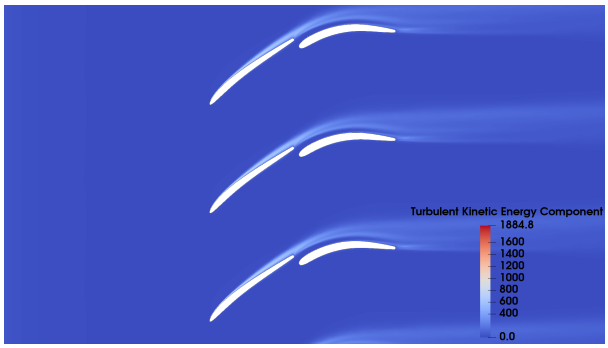

(e) Baseline at inlet flow angle of 56º

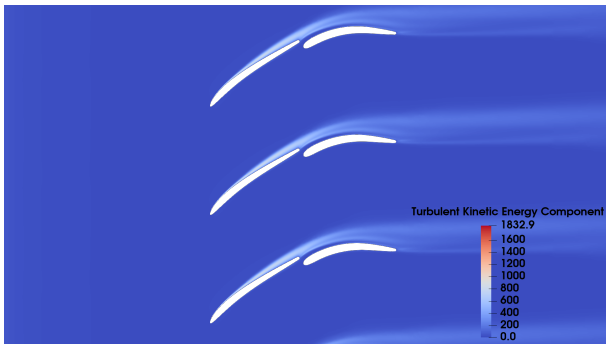

(f) Optimized at inlet flow angle of 56º

Figure 42. Comparison between the Turbulent Kinetic Energy (TKE) distributions of the flow of the baseline and the optimized configurations at on-design, high and low inlet flow angles

The ratio of turbulent to laminar viscosity is shown in Figure 43. The ratio is higher for the optimized configuration, thus explaining the deceleration of the wake.

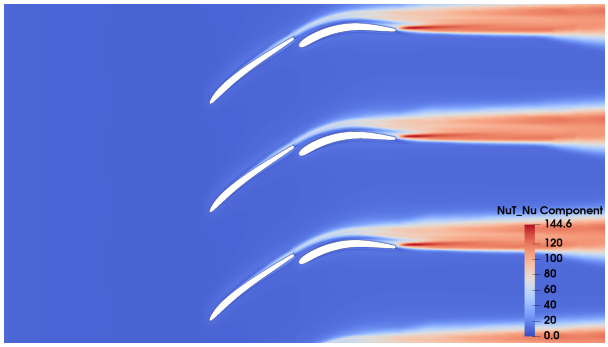

(a) Baseline at inlet flow angle of 50º

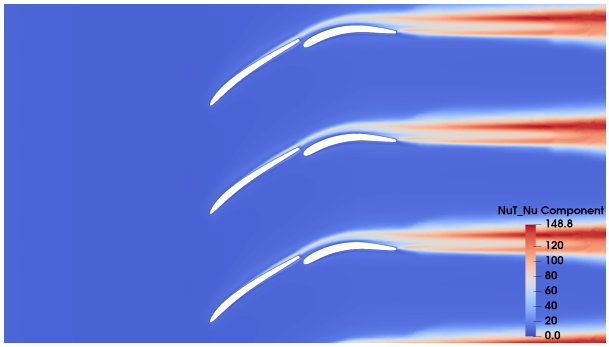

(b) Optimized at inlet flow angle of 50º

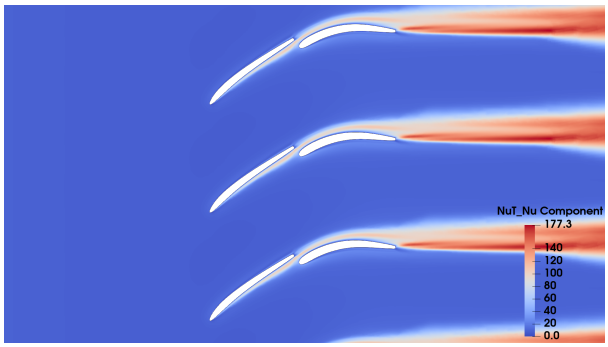

(c) Baseline at inlet flow angle of 40º

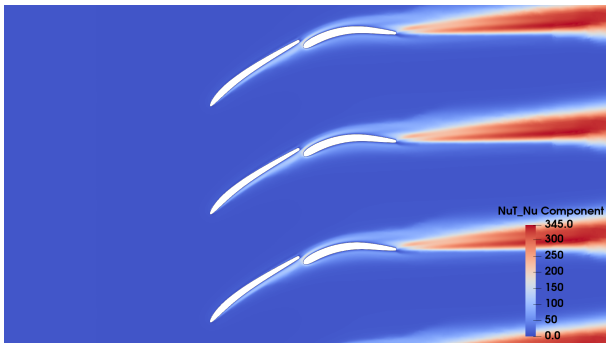

(d) Optimized at inlet flow angle of 40º

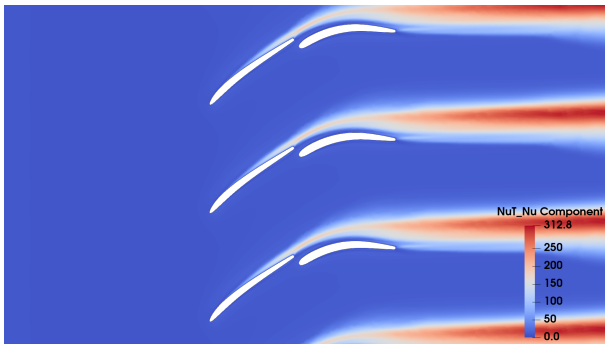

(e) Baseline at inlet flow angle of 56º

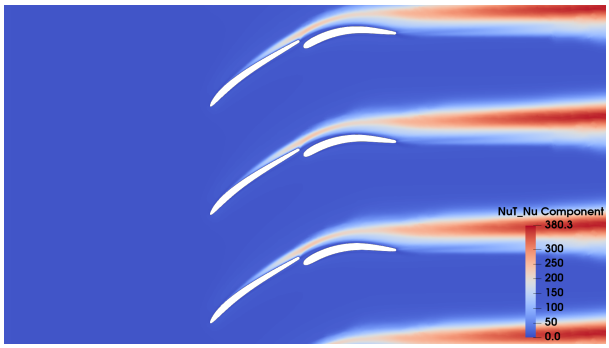

(f) Optimized at inlet flow angle of 56º

Figure 43. Comparison between the turbulent viscosity ratio distributions of the flow of the baseline and the optimized configurations at on-design, high and low inlet flow angles

6.4 Working Range Optimization

The second approach has been to improve the working range of the stage. In other words, the range of inlet flow angles where the pressure losses are smaller than two times those of the on-design configuration has been maximized. Additionally, the pressure losses of the on-design configuration have been kept within an acceptable range.

6.4.1 Optimization Consideration

The optimization process was designed to maximize the operational range while maintaining critical performance and geometric constraints:

- Primary Objective:
  - Extend the operational working range of the tandem configuration, defined as the range of inlet flow angles where the losses are within two times those of the reference inlet flow angle of 50º.
  - Maintain on-design losses within +20% of baseline performance.
- Performance Targets:
  - Evaluated performance at incremental angles beyond design condition (50°) spaced by 1º until the whole working range is captured.
- Geometric Constraints:
  - Fixed total axial tandem chord length (preserves spatial envelope and prevents excessive blade loading).
  - Fixed rear blade trailing edge position at $x = 1.51$ (maintains consistent downstream spacing).
  - Controlled exit flow angle variation: ±0.5° tolerance and ±1° critical tolerance.

The methodology proceeded through two key phases:

1. Baseline assessment at design condition (50° inlet flow angle).
2. Progressive evaluation of positive (> 50°) and negative incidence (< 50°) range in parallel.

The working range boundaries were determined when the pressure loss coefficient reached $\phi_{target} = 2\phi_{reference}$ in both positive and negative incidence directions. In case that convergence for a given inlet flow angle at any side of the polar was not reached, the previous case became the outer boundary.

In Figure 44, the polar of the baseline configuration is represented. This optimization aims to increase the working range (shaded area) while keeping the losses at the reference inlet flow angle (minimum point) within a certain margin.

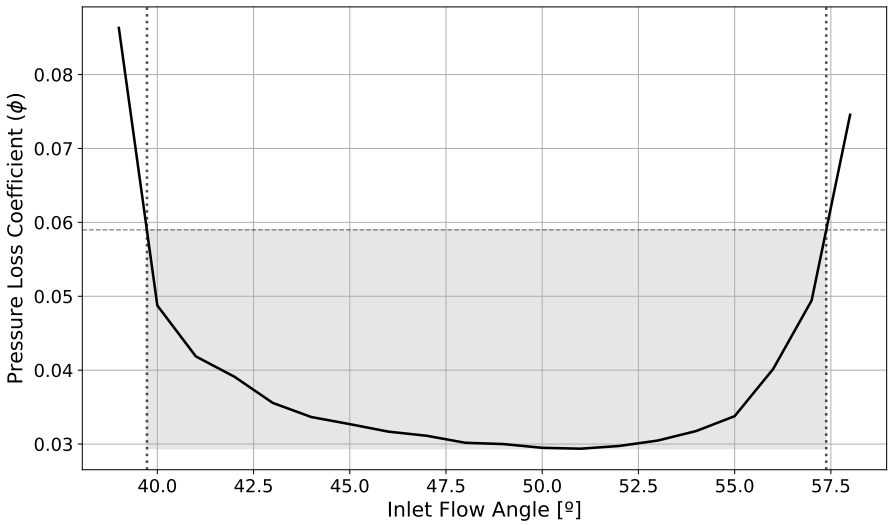

Figure 44. Objective loss coefficient polar

6.4.2 Performance Comparison

The specifications of the optimized geometry are summarized in Table VIII. The output geometry of this optimization has resulted in a tandem blade configuration which has increased both the axial and radial spacings between the blades, as can be seen reflected by the AO and PP values of the optimized configuration.

Variable	Symbol	Value	Units
Axial Overlap	AO	-4.20	%
Percentage Pitch	PP	85.00	%
Total axial chord	$C_{x,\text{total}}$	0.0294	m
Chord scaling (Front Blade)	$\text{ChordScale}_{\text{FB}}$	0.9500	–
Stagger angle delta (Front Blade)	$\Delta\beta_{\text{FB}}$	-5.000	º
LE angle delta (Front Blade)	$\Delta\theta_{\text{LE,FB}}$	0.361	º
TE angle delta (Front Blade)	$\Delta\theta_{\text{TE,FB}}$	2.500	º
Chord scaling (Rear Blade)	$\text{ChordScale}_{\text{RB}}$	0.9704	–
Stagger angle delta (Rear Blade)	$\Delta\beta_{\text{RB}}$	-0.408	º
LE angle delta (Rear Blade)	$\Delta\theta_{\text{LE,RB}}$	0.938	º
TE angle delta (Rear Blade)	$\Delta\theta_{\text{TE,RB}}$	-1.065	º

Table VIII. Geometric and design parameters used in the blade configuration (range boundaries)

The range optimization has successfully increased the working range by 17%. Conversely, there has been a trade-off with the on-design pressure losses, which have increased an 18%. The exit flow angle for the reference inlet flow angle has been kept within the critical ±1° established limit but not within the objective ±0.5°.

Parameter	Baseline	Optimized	Difference [%]	Units
Pressure Loss Coefficient (ϕ) at 50º	0.0295	0.0348	17.97	-
Exit Flow Angle	0.38	-0.71	289.47	º
Lower bound	39.73	32.80	67.45	º
Upper bound	57.38	53.45	53.25	º
Range	17.65	20.65	17.01	º

Table IX. Comparison of aerodynamic parameters between baseline and updated optimized configurations. Differences in lower and upper bounds are normalized with respect to their distance from 50º inlet flow angle.

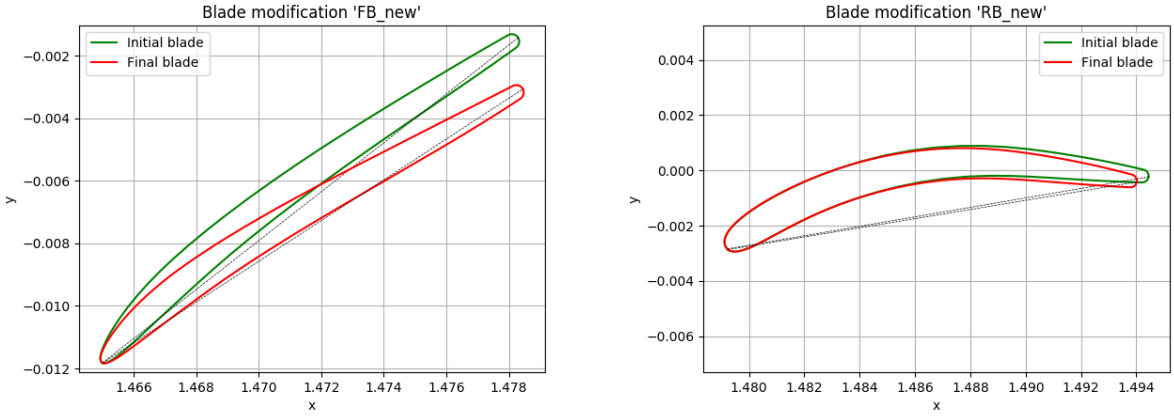

(a) FB comparison

(b) RB comparison

Figure 45. Comparison between the geometries of the baseline and optimized configurations

In Figure 46, the polars of the baseline and optimized configurations are represented. It may be noticed that the polar has shifted towards the side of negative incidence. This is a direct consequence of the optimization method used. In the optimization, the target has been to maximize the range while constraining the exit flow angle and ensuring that the center of the polar (point of minimum losses) remained within ±3° of the baseline configuration, which is 50º. However, a multi-point optimization is less unequivocal as it results in a Pareto front, which consists of all designs that are not dominated by others on all criteria, at once. Thus, the designer needs to choose a compromise. The selected way of monitoring the flow quantities has been to impose some constraints, which have been previously explained, and to define the working range as that where the losses are within two times those found at inlet flow angle of 50º. This way, the center of the polar has been virtually fixed with a certain degree of freedom at 50º.

Moreover, it can be noticed that the range of negative incidences is far greater than the range of positive incidences. This is because the flow at higher incidence is much more prone to detach. As a consequence, the optimizer has opted to choose a configuration where the physics of the flow are kept as continuous as possible while minimizing the losses at the outer side of the polar.

Nevertheless, for a compressor is more interesting to increase the upper range (right side of the polar) because it can further increase the compressor ratios as can be seen in Figure 47. Considering the obtained results, it has been deemed necessary to perform a third optimization which maximized the upper bound of the polar while keeping the previous constraints.

Even though the range optimization has been successful, the results obtained out of it are not interesting for the design of the last stage of the compressor. However, they will be presented in the section below to be later compared with the results obtained in the next optimization.

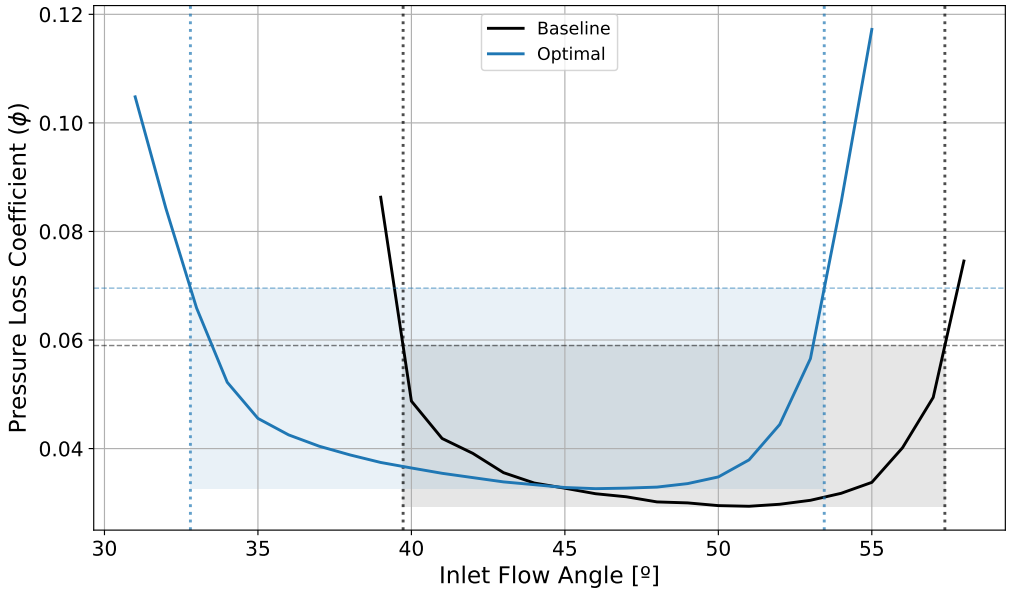

Figure 46. Comparison between the polars of the baseline and optimized configurations

In Figure 47, the pressure rise evolution of the baseline and optimized configurations are represented. The range of inlet flow angles where the pressure ratio is above 1.16 is significantly reduced for the optimized configuration.

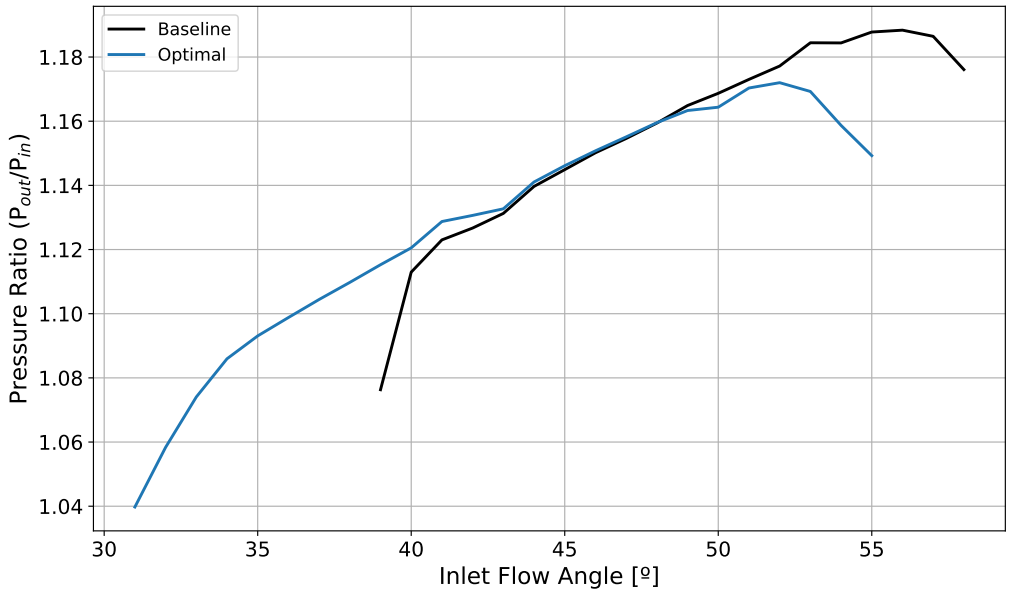

Figure 47. Comparison between the pressure ratio evolution of the baseline and optimized configurations

Finally, in Figure 48, the exit flow angle is represented in terms of the inlet flow angle. In this case, the exit flow angle of the optimized configuration has been kept within the critical ±1° for the reference inlet flow angle. However, this condition has not been satisfied for most inlet flow angles.

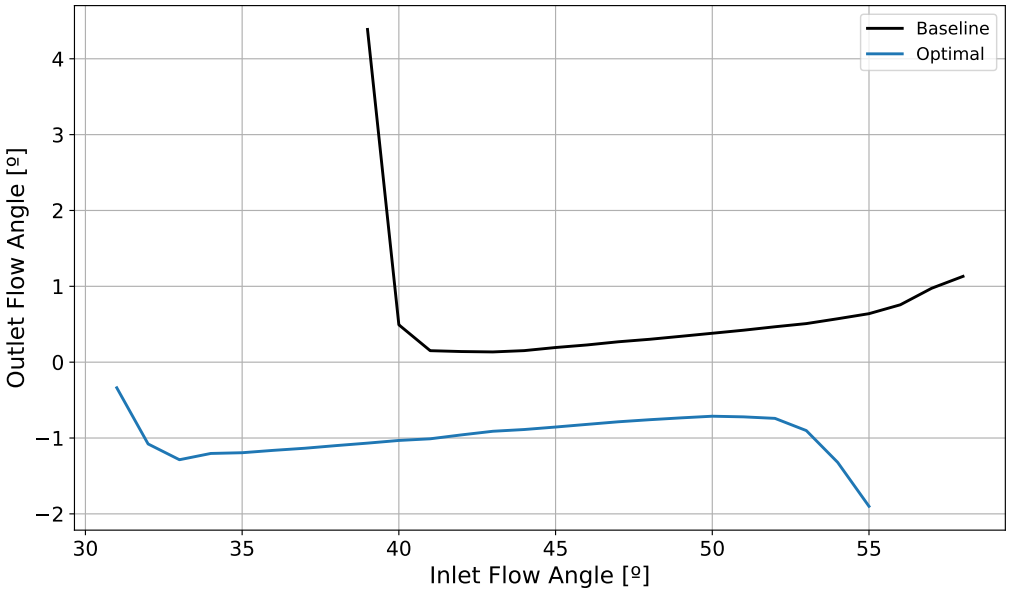

Figure 48. Comparison between the exit flow angle evolution of the baseline and optimized configurations

6.4.3 Blade Analysis

In Figure 63, the pressure coefficient over the blades is presented for both configurations. In this case, the pressure distributions of the RB or both configurations are quite similar. However, a small region near the leading edge of the FB exhibits a high loading, which may lead to flow separation. This behavior is consistent with the results found on the loss coefficient polar. The reference inlet flow angle of the optimized configuration is found at 45º, not at 50º like for the baseline configuration. Thus, there is a huge suction peak that appears at the on-design point.

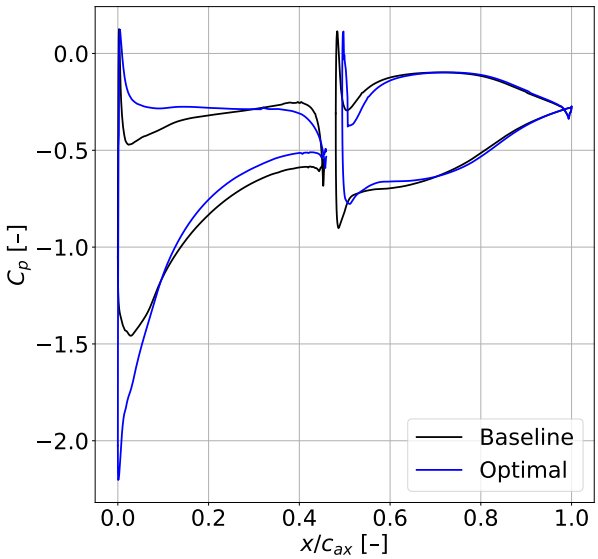

(a) Inlet flow angle of 50º

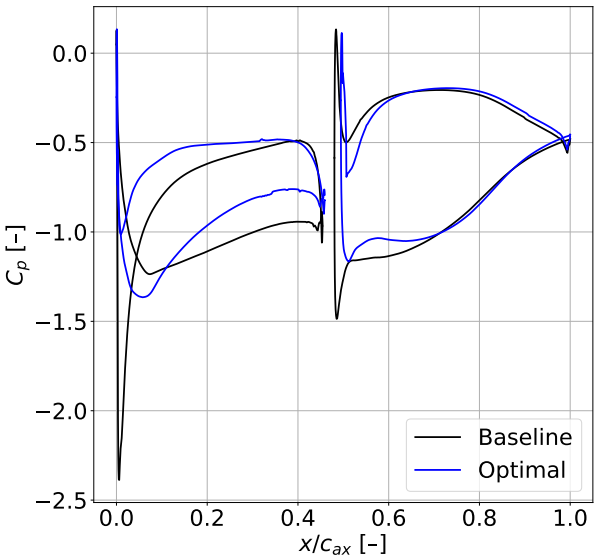

(b) Inlet flow angle of 40º

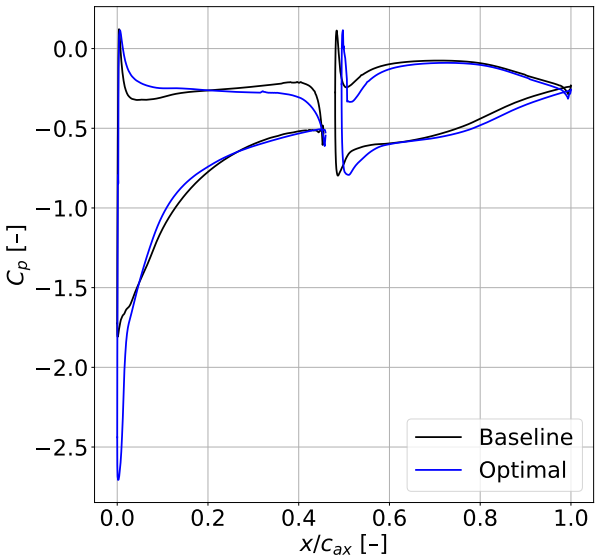

(c) Inlet flow angle of 53º

Figure 49. Comparison between the pressure coefficient distributions of the baseline and optimized configurations

6.4.4 Flow Visualization

In Figure 50, the Mach number distributions along the flow have been represented for several inlet flow angles. The wake of the optimized configuration is significantly wider, which explains the increment of the losses. Additionally, the optimized configuration is not capable of slowing the flow downstream significantly for low inlet flow angles. The flow on the FB is incapable of doing such a sharp turning and detaches for inlet flow angles of 50º and above.

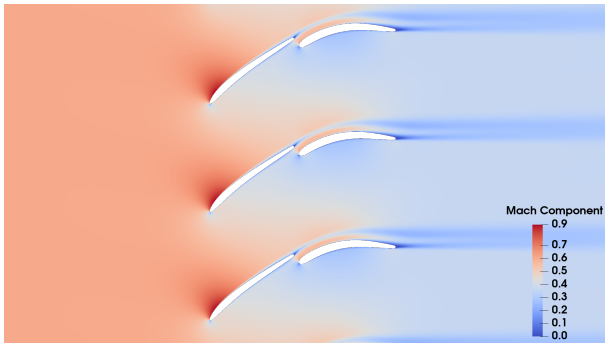

(a) Baseline at inlet flow angle of 50º

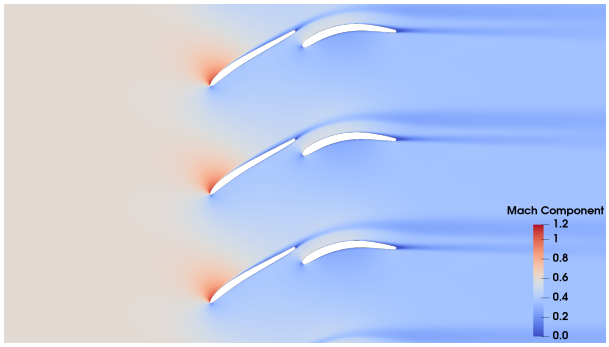

(b) Optimized at inlet flow angle of 50º

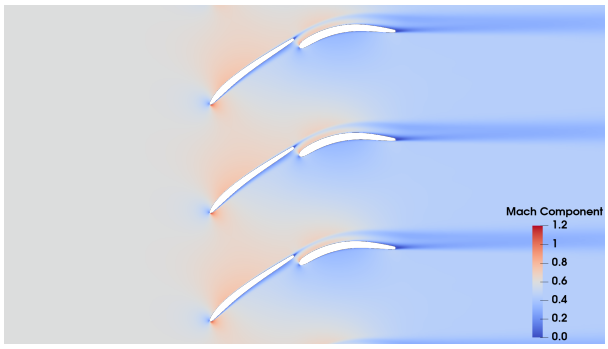

(c) Baseline at inlet flow angle of 40º

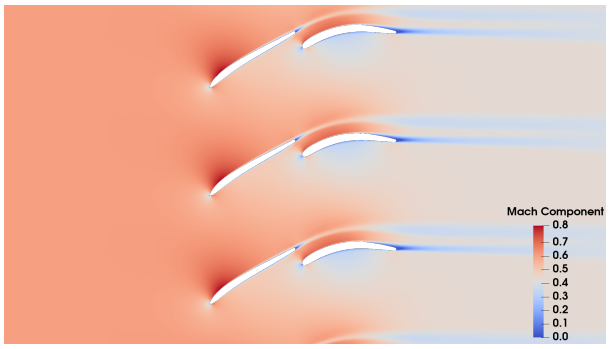

(d) Optimized at inlet flow angle of 40º

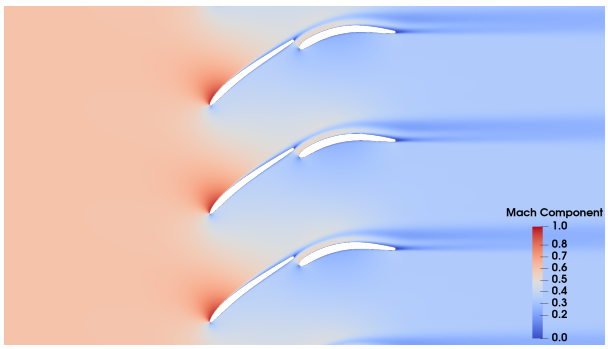

(e) Baseline at inlet flow angle of 53º

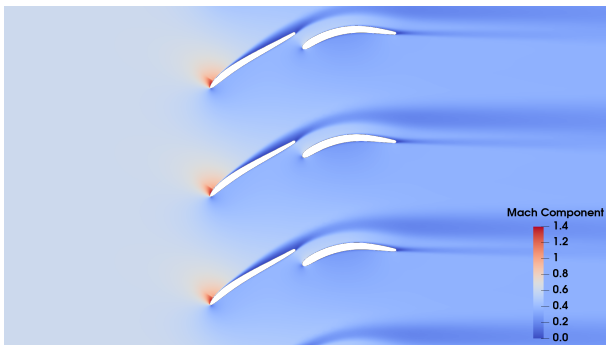

(f) Optimized at inlet flow angle of 53º

Figure 50. Comparison between the Mach distributions of the flow of the baseline and the optimized configurations at on-design, high and low inlet flow angles

In Figure 51, the Pressure distributions over the flow are represented. For low inlet flow

angles, the pressure drop of the suction side of the FB is extended to the RB. For high inlet flow angles, the zone of low pressure at the LE of the FB is reduced.

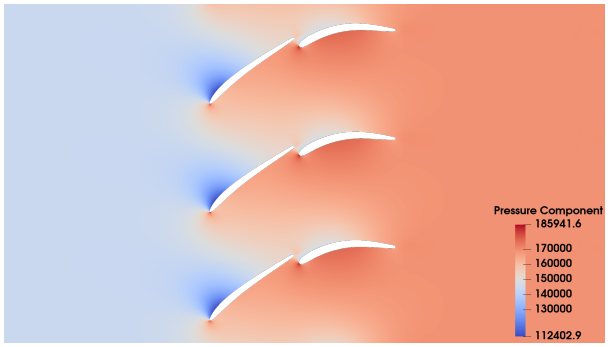

(a) Baseline at inlet flow angle of 50º

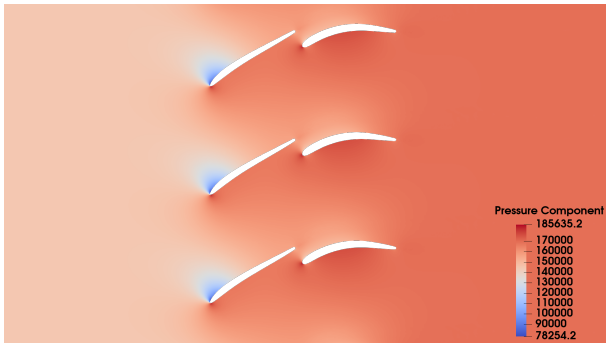

(b) Optimized at inlet flow angle of 50º

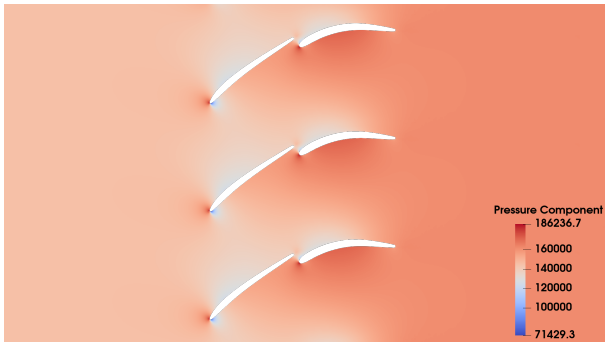

(c) Baseline at inlet flow angle of 40º

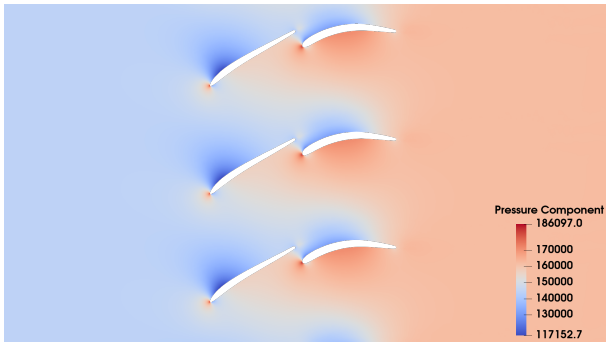

(d) Optimized at inlet flow angle of 40º

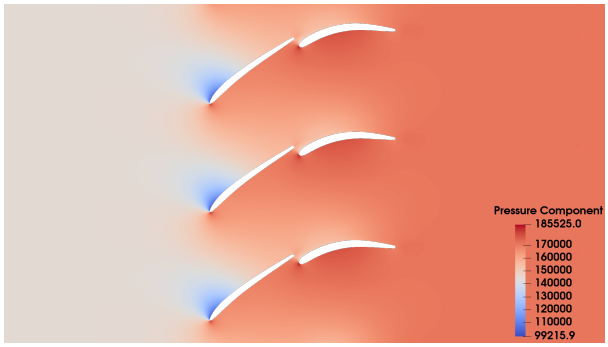

(e) Baseline at inlet flow angle of 53º

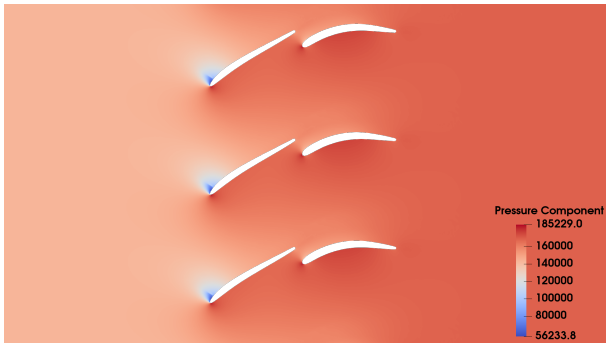

(f) Optimized at inlet flow angle of 53º

Figure 51. Comparison between the pressure distributions of the flow of the baseline and the optimized configurations at on-design, high and low inlet flow angles

In Figure 52, the evolution of flow quantities along streamlines over the flow at different inlet flow angles is represented. The optimized configuration presents a more fluctuating streamline. The general behavior of both configurations is similar and an axial flow at the exit is achieved.

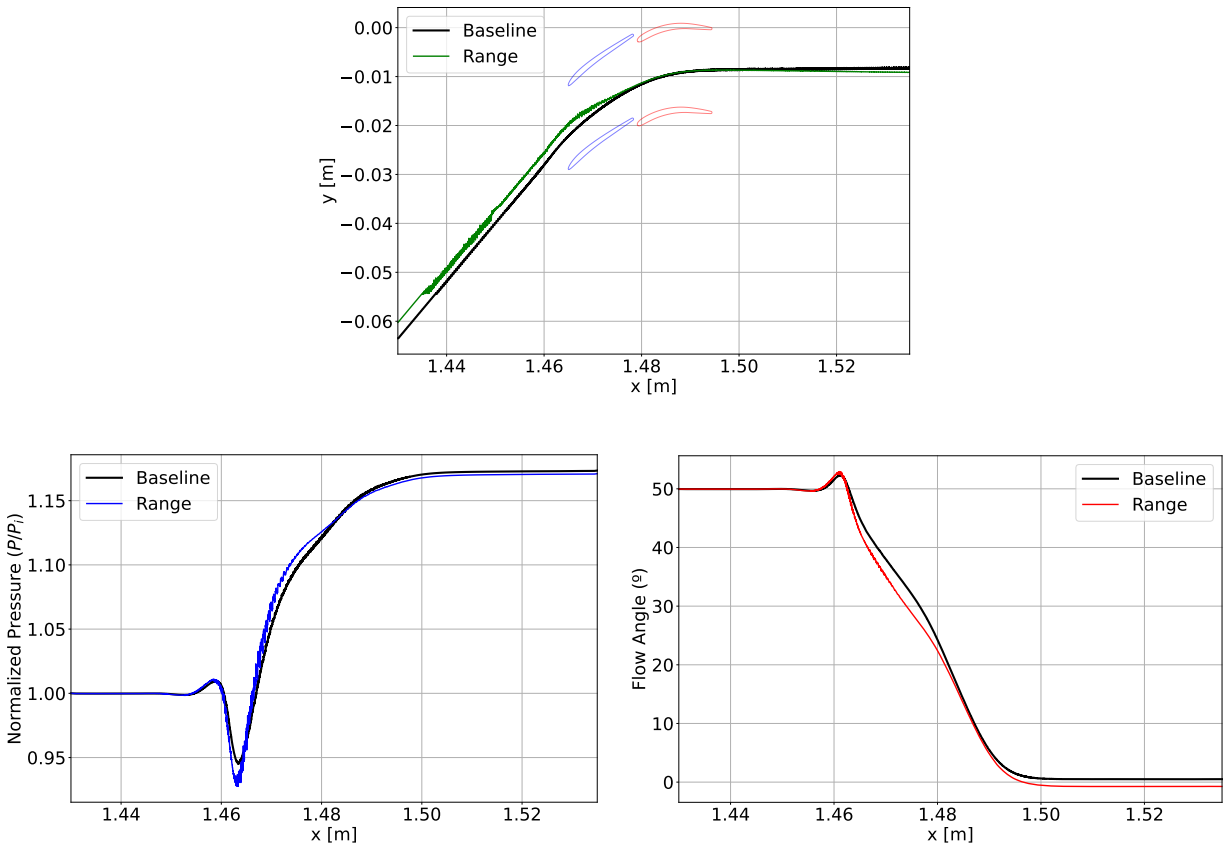

Figure 52. Comparison of the flow quantities represented over streamlines at inlet flow angle of 50º

6.4.5 Wake Analysis

In Figure 53, the pressure loss distribution at the MP2 point is presented for both configurations. A similar conclusion to which has been drawn from the previous Figure can be achieved. The optimized configuration presents wider and more separated wakes, but that are less severe too. For low inlet flow angles, the main contributor to the pressure losses is the wake of the rear blade. The inverse happens for high inlet flow angles.

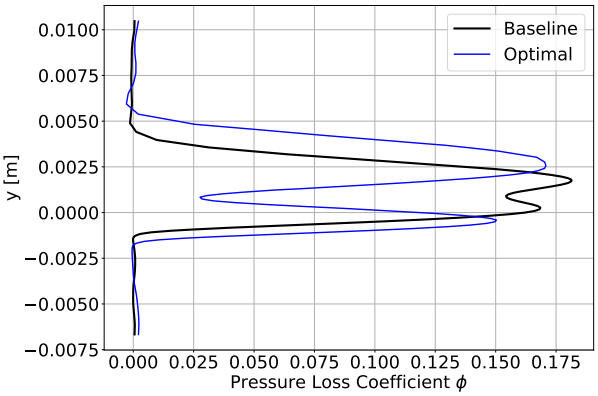

(a) Inlet flow angle of 50º

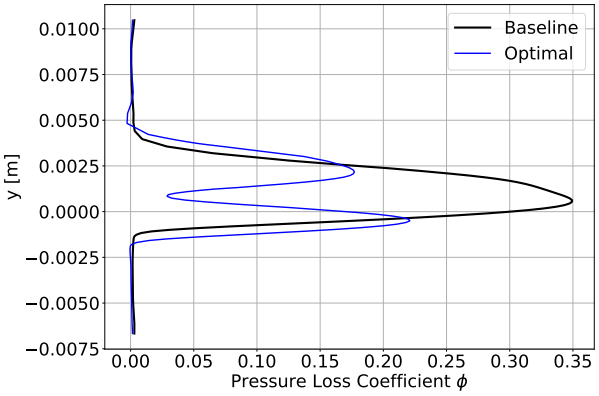

(b) Inlet flow angle of 40º

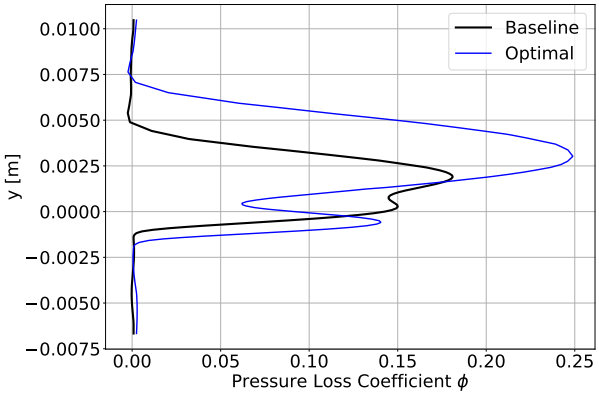

(c) Inlet flow angle of 53º

Figure 53. Comparison between the pressure loss distributions at x = 1.51 of the flow of the baseline and optimized configurations

In Figure 54, the exit flow angle distributions at the MP2 point are represented. Since the wake of the optimized configuration is less severe, the overall tendency of the optimized exit flow angle is less fluctuating than the baseline configuration across different inlet flow angles. Nevertheless, this is not the case for high inlet flow angles. This discrepancy is caused because at an inlet flow angle of 53º, the optimized configuration is almost at the outer boundary of the working range and more complex phenomena starts to appear. However, this is not the case for the baseline configuration.

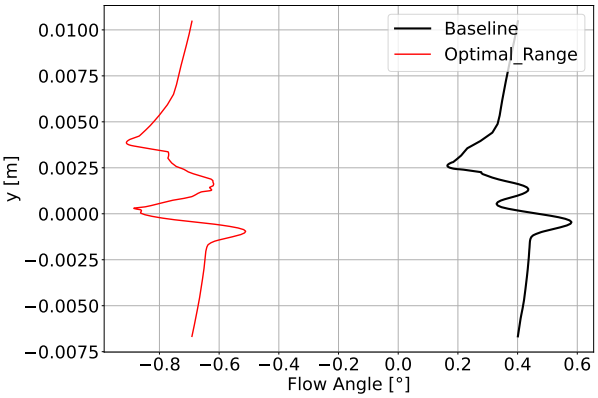

(a) Inlet flow angle of 50º

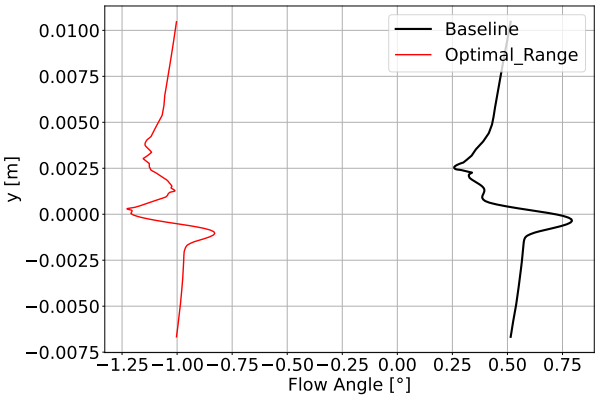

(b) Inlet flow angle of 40º

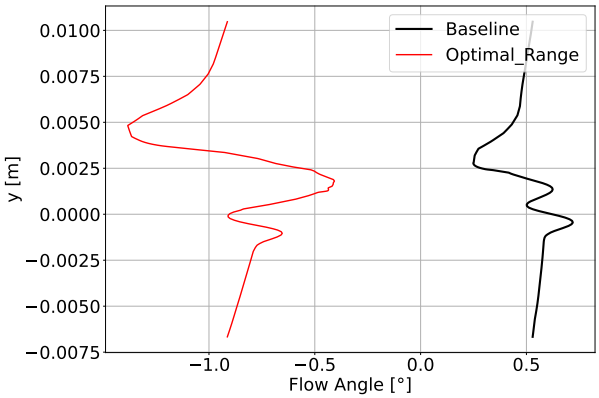

(c) Inlet flow angle of 53º

Figure 54. Comparison between the pressure loss distributions at x = 1.51 of the flow of the baseline and optimized configurations

6.4.6 Turbulence Analysis

In Figure 42 the turbulent kinetic energy of both configurations is presented. The optimized configuration presents a wider turbulent region. The high turbulent zone close to the TE of the RB that is present on the baseline configuration for an inlet flow angle of 50º is not present for the optimized one. However, a greater turbulent zone in the same location appears for the optimized configuration at low inlet flow angles.

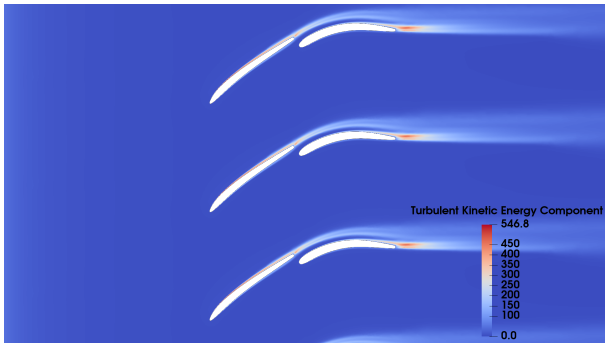

(a) Baseline at inlet flow angle of 50º

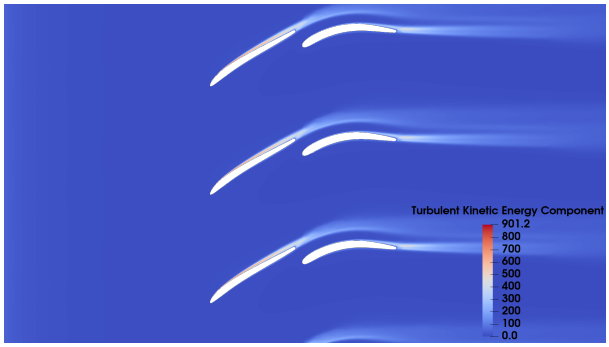

(b) Optimized at inlet flow angle of 50º

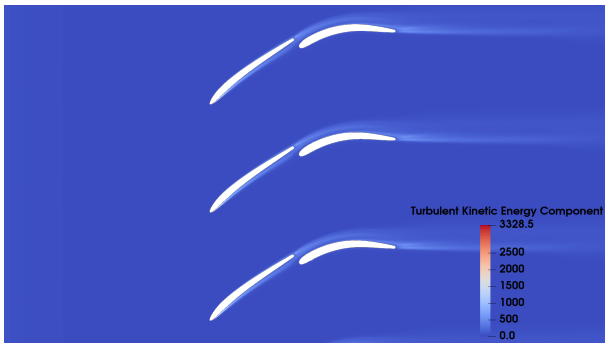

(c) Baseline at inlet flow angle of 40º

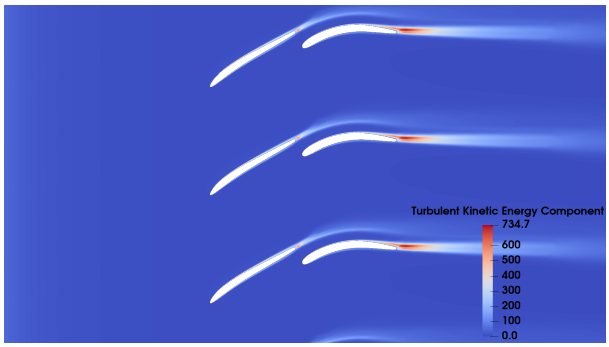

(d) Optimized at inlet flow angle of 40º

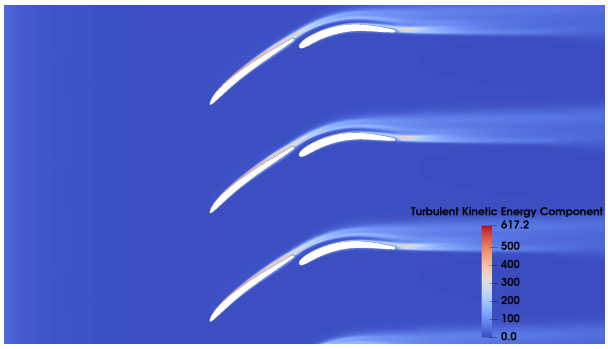

(e) Baseline at inlet flow angle of 53º

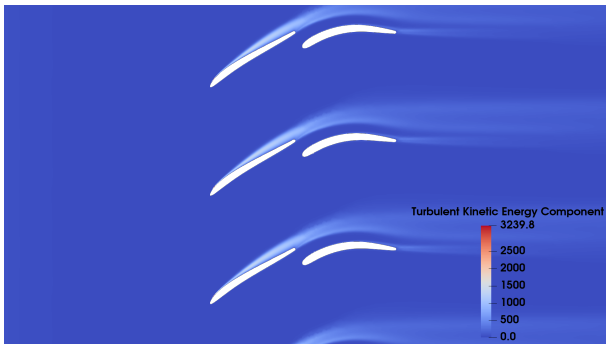

(f) Optimized at inlet flow angle of 53º

Figure 55. Comparison between the turbulent kinetic energy distributions of the flow of the baseline and the optimized configurations at on-design, high and low inlet flow angles

The ratio of turbulent viscosity to laminar viscosity is shown in Figure 56. The viscosity of the wake is similar for both configurations. Thus explaining the similar Mach magnitudes of both configurations. The optimized configuration presents a wider wake. The viscosity at high inlet flow angles is remarkably high for the optimized configuration. This may explain why the tandem blade is not capable of compressing the flow as much as the baseline configuration.

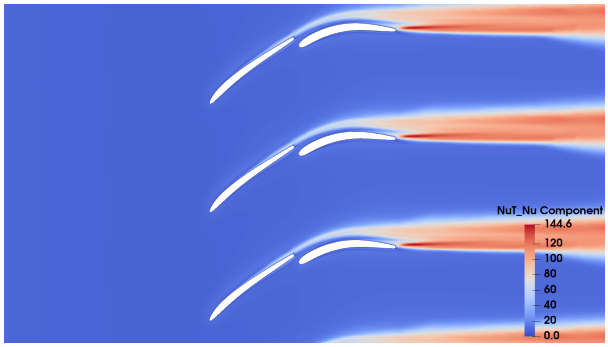

(a) Baseline at inlet flow angle of 50º

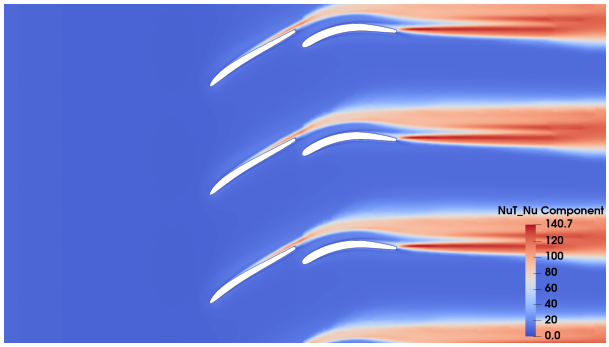

(b) Optimized at inlet flow angle of 50º

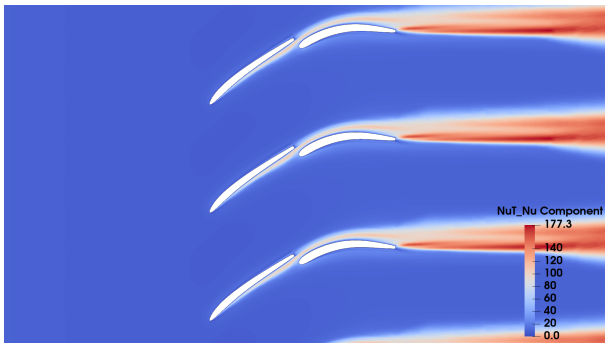

(c) Baseline at inlet flow angle of 40º

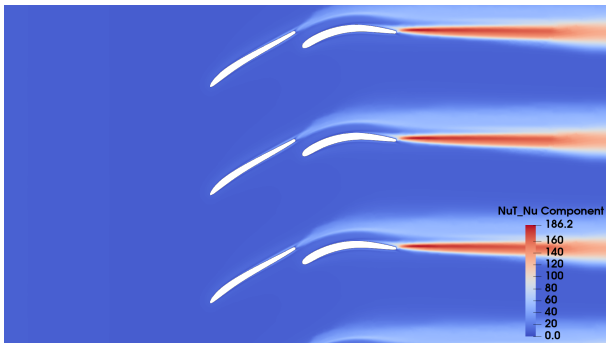

(d) Optimized at inlet flow angle of 40º

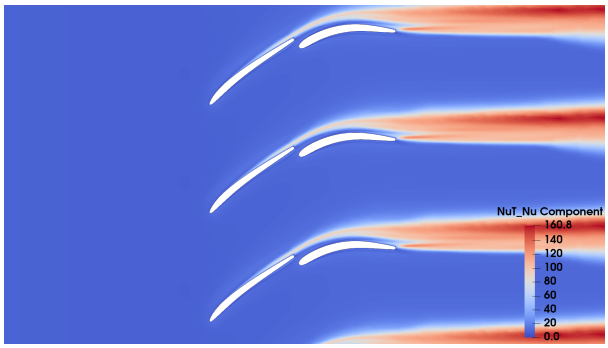

(e) Baseline at inlet flow angle of 53º

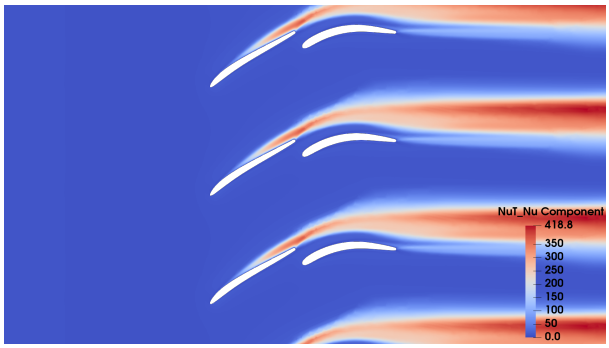

(f) Optimized at inlet flow angle of 53º

Figure 56. Comparison between the turbulent viscosity ratio distributions of the flow of the baseline and the optimized configurations at on-design, high and low inlet flow angles

6.4.7 Very Low Inlet Flow Angles

Since no data at very low inlet flow angles is available for the baseline configuration, this section shall present an overview of its influence on the flow parameters. With negative incidence, the capabilities of the tandem blade to slow down and increase the pressure downstream are reduced. Additionally, a high viscous region on the pressure side of the FB appears.

The previous study has confirmed that the second optimization has been suboptimal from a designing point of view for the OGV. Hence, reinforcing the need of the third optimization.

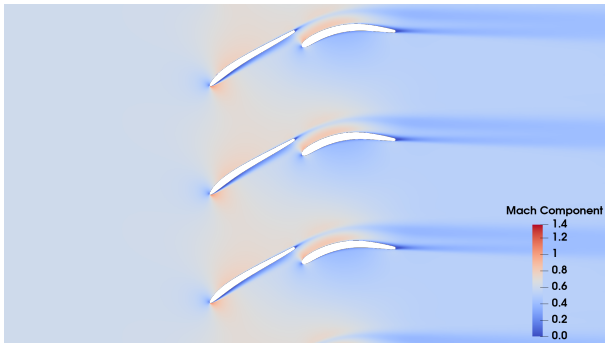

(a) Mach number distribution

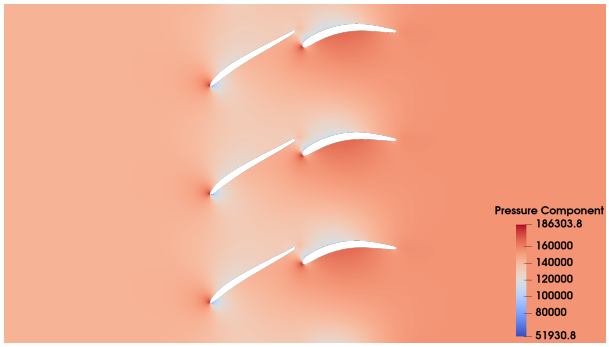

(b) Pressure distribution

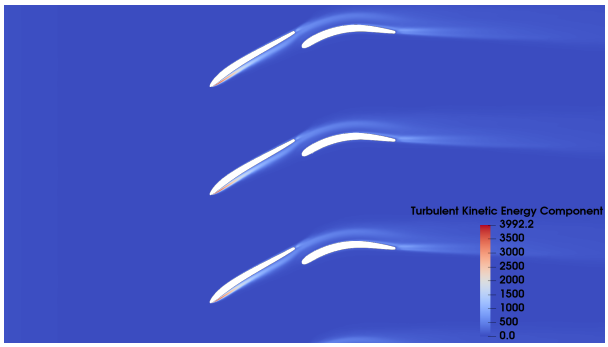

(c) Turbulent kinetic energy distribution

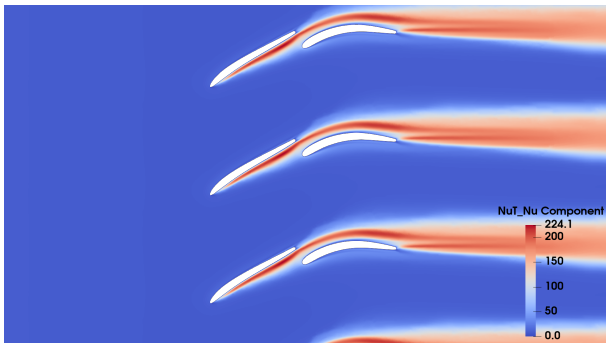

(d) Turbulent viscosity ratio distribution

Figure 57. Flow quantities distributions of the optimized configuration at inlet flow angle of 33º

6.5 Upper Bound Optimization

The third approach has been to maximize the upper bound range of the stage. As for the previous optimization, the pressure losses of the on-design configuration have been kept within an acceptable range.

6.5.1 Optimization Consideration

The optimization process was designed to maximize the operational range while maintaining critical performance and geometric constraints:

- Primary Objective:
  - Extend the upper bound working range of the tandem configuration, defined as the range between the upper boundary of the working range and the reference inlet flow angle of 50º.
  - Maintain on-design losses within +20% of baseline performance.
- Performance Targets:
  - Evaluated performance at incremental angles beyond design condition (50°) spaced by 1º until the whole working range is captured.
- Geometric Constraints:
  - Fixed total axial tandem chord length (preserves spatial envelope and prevents excessive blade loading).
  - Fixed rear blade trailing edge position at $x = 1.51$ (maintains consistent downstream spacing).
  - Controlled exit flow angle variation: ±0.5° tolerance and ±1° critical tolerance.

As for the previous optimization, the methodology proceeded through two key phases:

1. Baseline assessment at design condition (50° inlet flow angle).
2. Progressive evaluation of positive (> 50°) and negative incidence (< 50°) range in parallel.

The upper bound range boundaries were determined when the pressure loss coefficient reached $\phi_{target} = 2\phi_{reference}$ on the side of positive incidence of the polar. In case that convergence for a given inlet flow angle at any side of the polar was not reached, the previous case became the outer boundary.

In Figure 58, the polar of the baseline configuration is represented. This optimization aims to increase the upper bound of the working range (shaded area) while keeping the losses at the reference inlet flow angle (minimum point) within a certain margin.

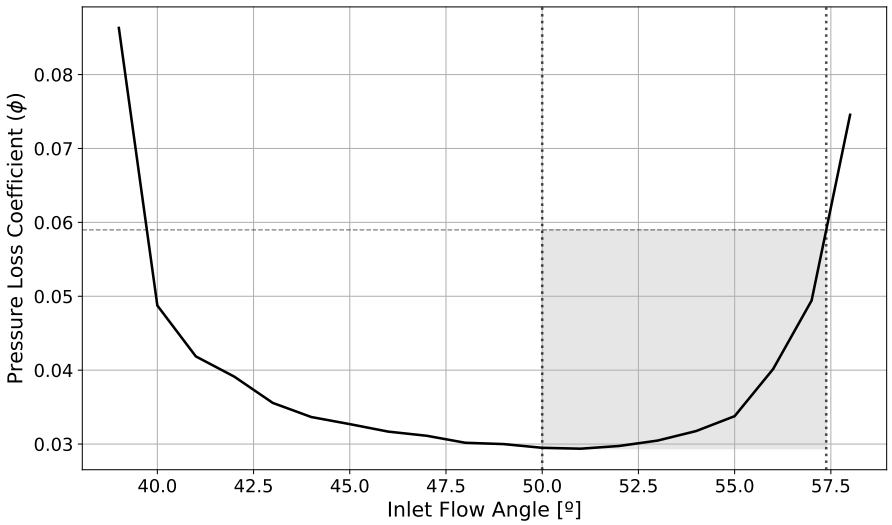

Figure 58. Objective loss coefficient polar

6.5.2 Performance Comparison

The specifications of the optimized geometry are summarized in Table VIII. To optimize the upper range of the polar, the optimization process has opted to increase the axial spacing between the blades and to slightly augment the PP when comparing it to the previous optimization.

Variable	**Symbol**	**Value**	**Units**
Axial Overlap	AO	-6.21	%
Percentage Pitch	PP	88.96	%
Total axial chord	$C_{x,\text{total}}$	0.0294	m
Chord scaling (Front Blade)	$\text{ChordScale}_{\text{FB}}$	0.9861	–
Stagger angle delta (Front Blade)	$\Delta\beta_{\text{FB}}$	2.066	º
LE angle delta (Front Blade)	$\Delta\theta_{\text{LE,FB}}$	0.944	º
TE angle delta (Front Blade)	$\Delta\theta_{\text{TE,FB}}$	2.500	º
Chord scaling (Rear Blade)	$\text{ChordScale}_{\text{RB}}$	0.9686	–
Stagger angle delta (Rear Blade)	$\Delta\beta_{\text{RB}}$	-5.000	º
LE angle delta (Rear Blade)	$\Delta\theta_{\text{LE,RB}}$	-2.500	º
TE angle delta (Rear Blade)	$\Delta\theta_{\text{TE,RB}}$	0.697	º

Table X. Geometric and design parameters used in the blade configuration (range boundaries)

The upper bound optimization has successfully risen the upper bound by 26% (2º) compared to the baseline configuration. However, the pressure losses have been increased by about 40% and the exit flow angle hasn't achieved the objective ±1°. It may be concluded that to rise substantially the range of positive incidence is a complex process that has a major impact on the performance of the tandem blade.

Parameter	**Baseline**	**Optimized**	**Difference [%]**	**Units**
Pressure Loss Coefficient (ϕ) at 50º	0.0295	0.0416	41.08	-
Exit Flow Angle	0.38	-1.36	457.89	º
Lower bound	39.73	41.78	19.96	º
Upper bound	57.38	59.29	25.89	º
Range	17.65	17.51	0.79	º

Table XI. Comparison of aerodynamic parameters between baseline and updated optimized configurations. Differences in lower and upper bounds are normalized with respect to their distance from 50º inlet flow angle.

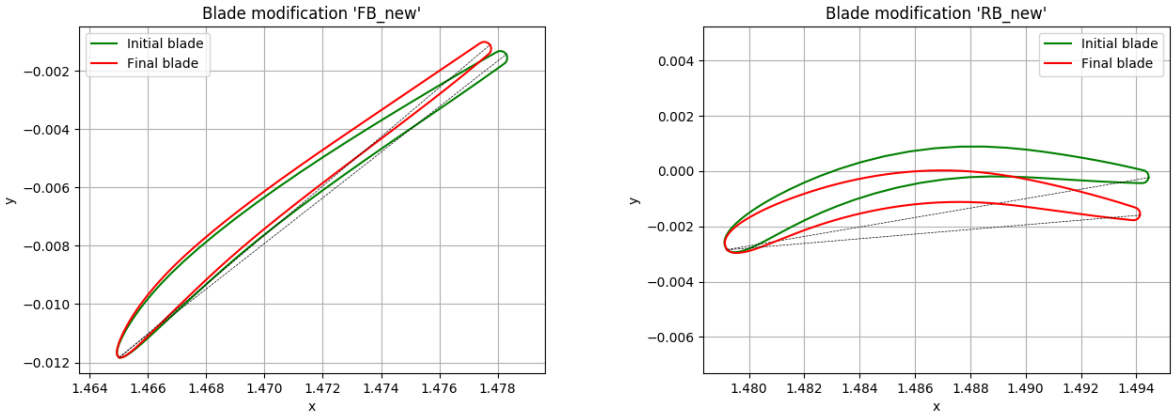

(a) FB comparison

(b) RB comparison

Figure 59. Comparison between the geometries of the baseline and optimized configurations

In Figure 60, the polars of the baseline and optimized configurations are represented. The center of the optimized configuration has been slightly shifted towards higher inlet flow angles. As it has been previously mentioned, the center of the polar has been virtually fixed by defining the working range from the reference inlet of 50º. However, a small shift has been accepted in the optimization process.

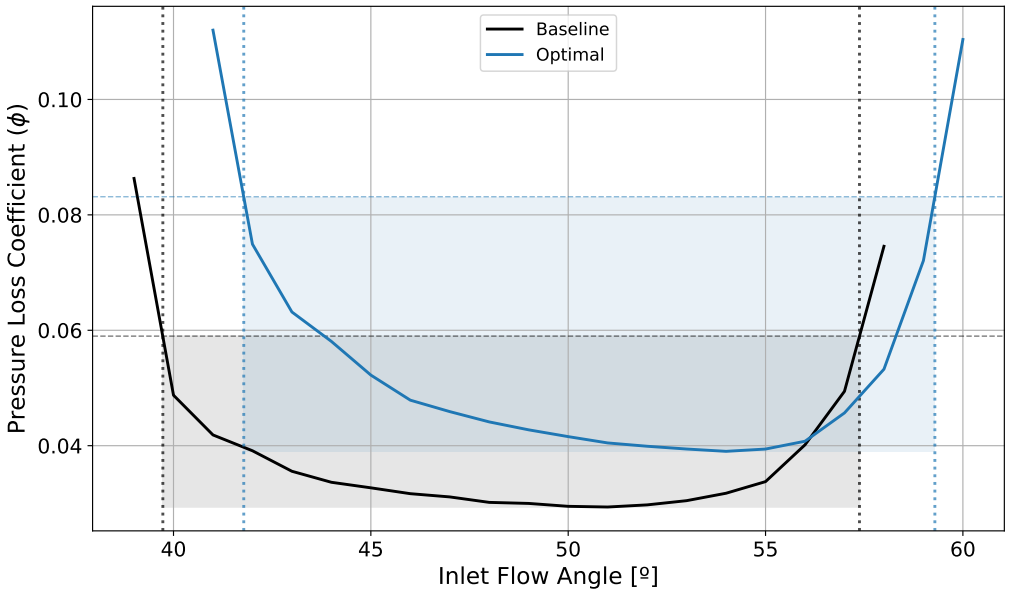

Figure 60. Comparison between the polars of the baseline and optimized configurations

In Figure 61, the pressure rise evolution of the baseline and optimized configurations are represented. The range of inlet flow angles with pressure ratios above 1.16 has been incremented. Additionally, the maximum compression of the optimized configuration has been above the baseline one.

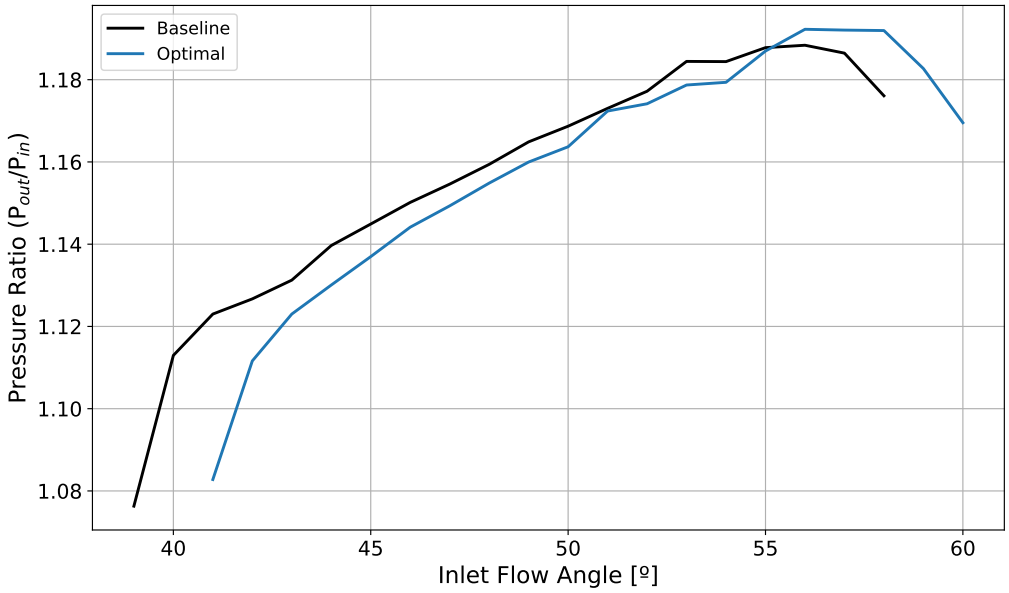

Figure 61. Comparison between the pressure ratio evolution of the baseline and optimized configurations

Finally, in Figure 62, the exit flow angle is represented in terms of the inlet flow angle. In this case, the exit flow angle of the optimized configuration has not been kept within the critical $\pm 1^{\circ}$ for the reference inlet flow angle.

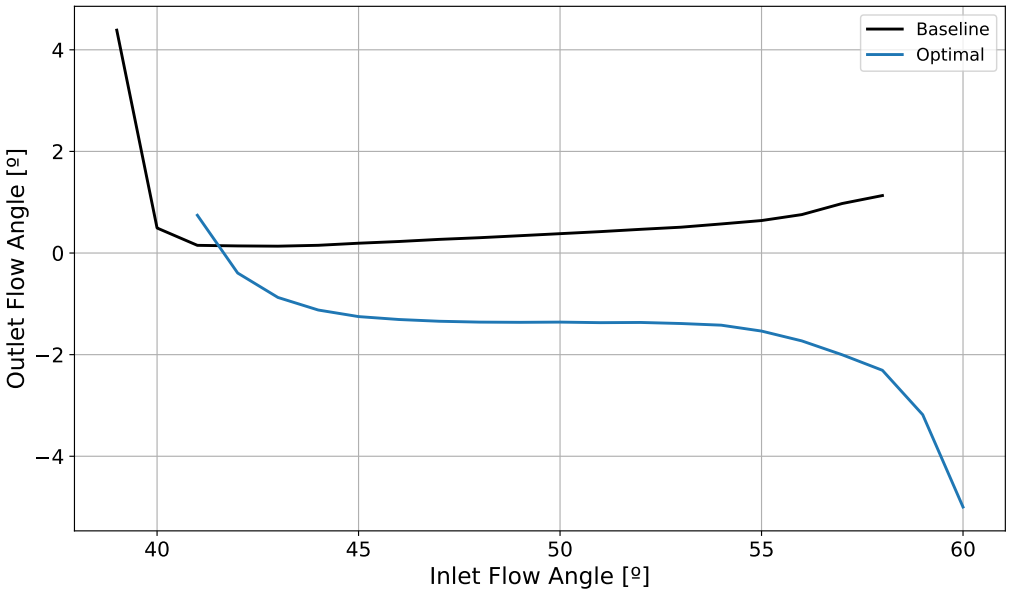

Figure 62. Comparison between the exit flow angle evolution of the baseline and optimized configurations

6.5.3 Blade Analysis

In this section, an analysis of the pressure coefficients on the surface of the blades are presented. In Figure 63, it may be appreciated that the distributions for both configurations are similar. However, high loadings are present on the LE of both blades, which may induce flow separation.

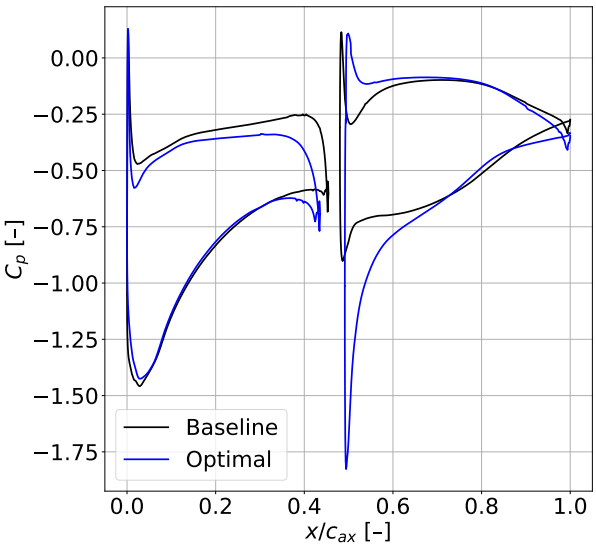

(a) Inlet flow angle of 50º

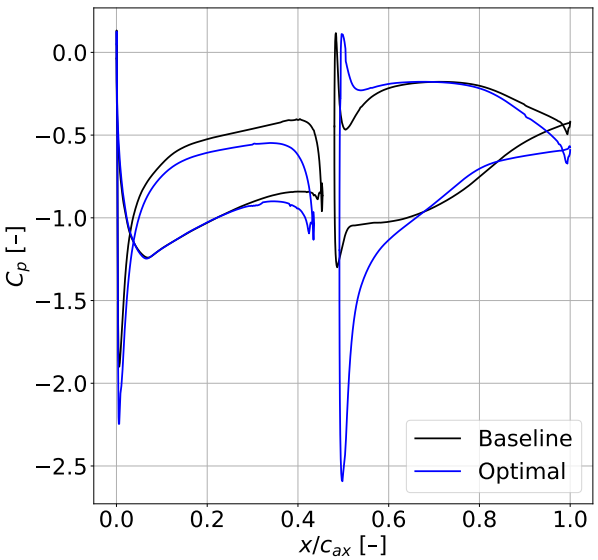

(b) Inlet flow angle of 42º

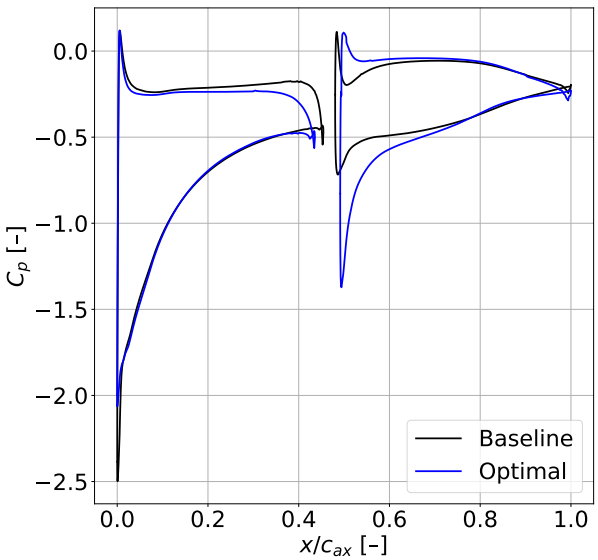

(c) Inlet flow angle of 56º

Figure 63. Comparison between the pressure coefficient distributions of the baseline and optimized configurations

6.5.4 Flow Visualization

In Figure 64 the Mach number distributions along the flow have been represented for several inlet flow angles. The wake of the optimal configuration is slightly wider. However, there is a large region at the TE of the RB where the flow is significantly slowed down. This, combined with the wider range of the wake, may cause a substantial increment of losses of this configuration.

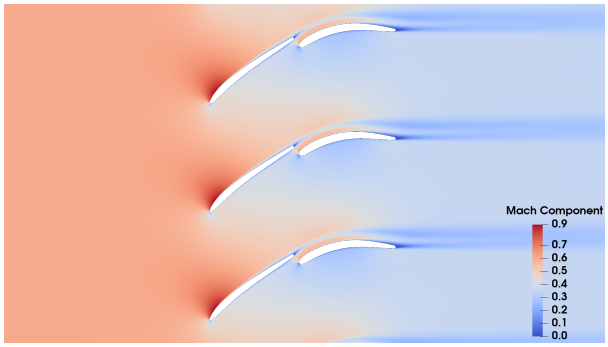

(a) Baseline at inlet flow angle of 50º

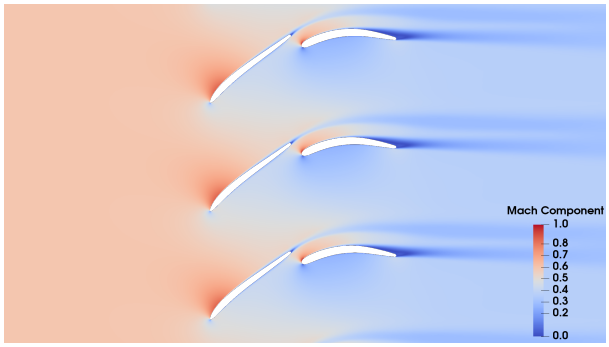

(b) Optimized at inlet flow angle of 50º

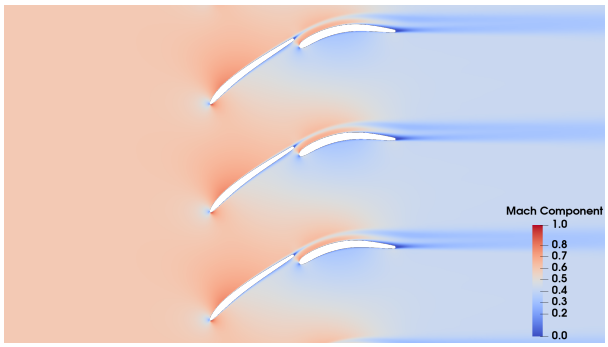

(c) Baseline at inlet flow angle of 42º

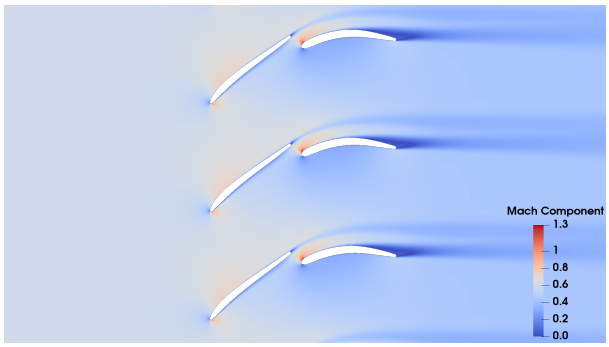

(d) Optimized at inlet flow angle of 42º

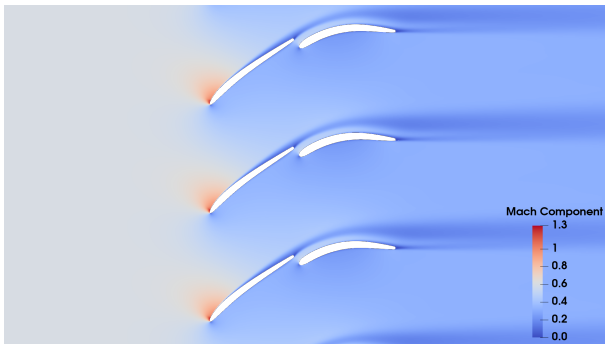

(e) Baseline at inlet flow angle of 56º

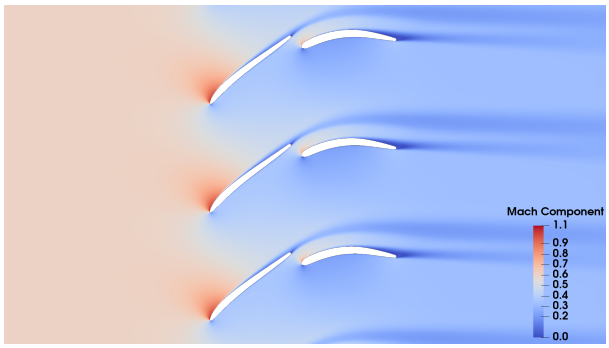

(f) Optimized at inlet flow angle of 56º

Figure 64. Comparison between the Mach distributions of the flow of the baseline and the optimized configurations at on-design, high and low inlet flow angles

In Figure 65, the Pressure distributions over the flow are represented. For inlet flow angles below 50º there is a pressure drop on the LE of both blades. Nevertheless, such drop is not present on the RB for higher inlet flow angles. As expected, the compression capabilities of both configurations are similar.

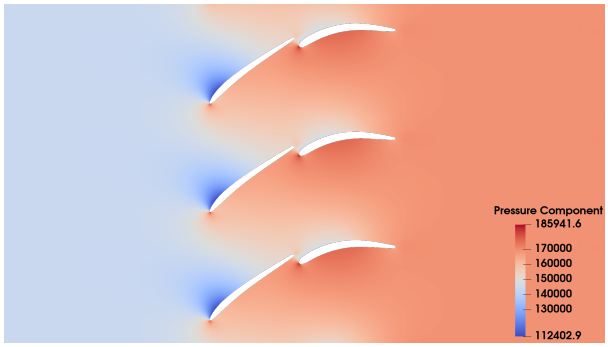

(a) Baseline at inlet flow angle of 50º

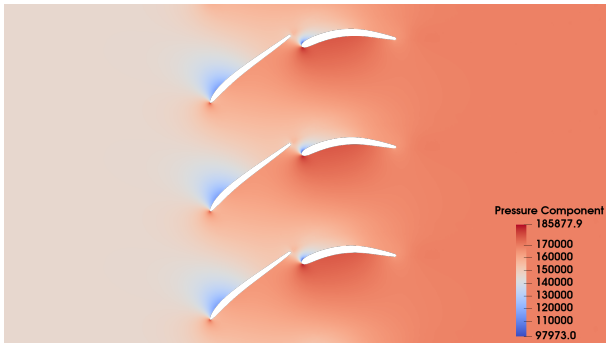

(b) Optimized at inlet flow angle of 50º

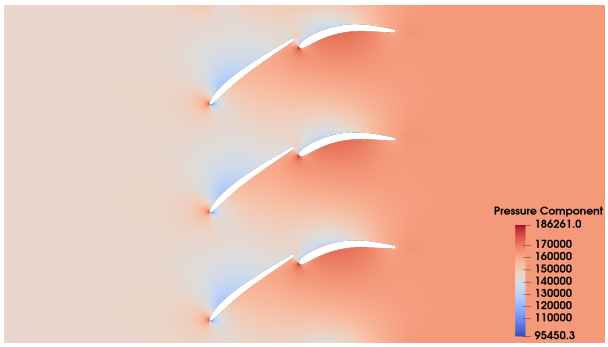

(c) Baseline at inlet flow angle of 42º

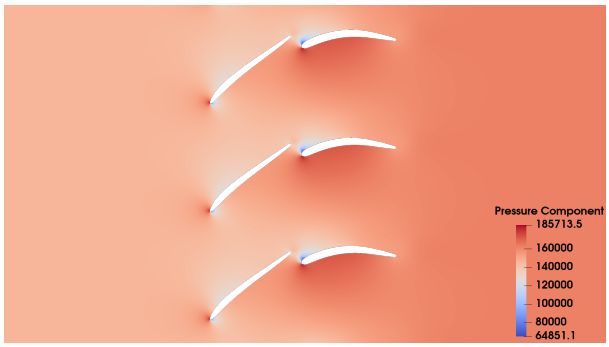

(d) Optimized at inlet flow angle of 42º

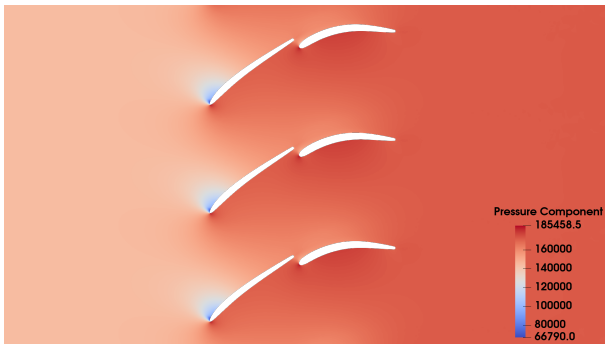

(e) Baseline at inlet flow angle of 56º

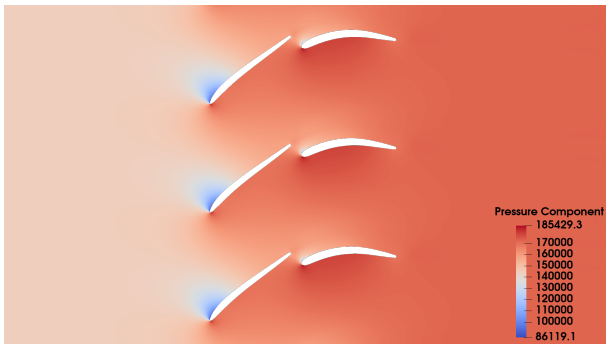

(f) Optimized at inlet flow angle of 56º

Figure 65. Comparison between the pressure distributions of the flow of the baseline and the optimized configurations at on-design, high and low inlet flow angles

In Figure 66, the evolution of flow quantities along streamlines over the flow at different inlet flow angles is represented. The pressure evolution of both configurations is similar. However, the streamline representation captures a pressure drop on the RB of the optimal configuration. Additionally, it can be seen that the exit flow angle of the optimal configuration has a slight radial component.

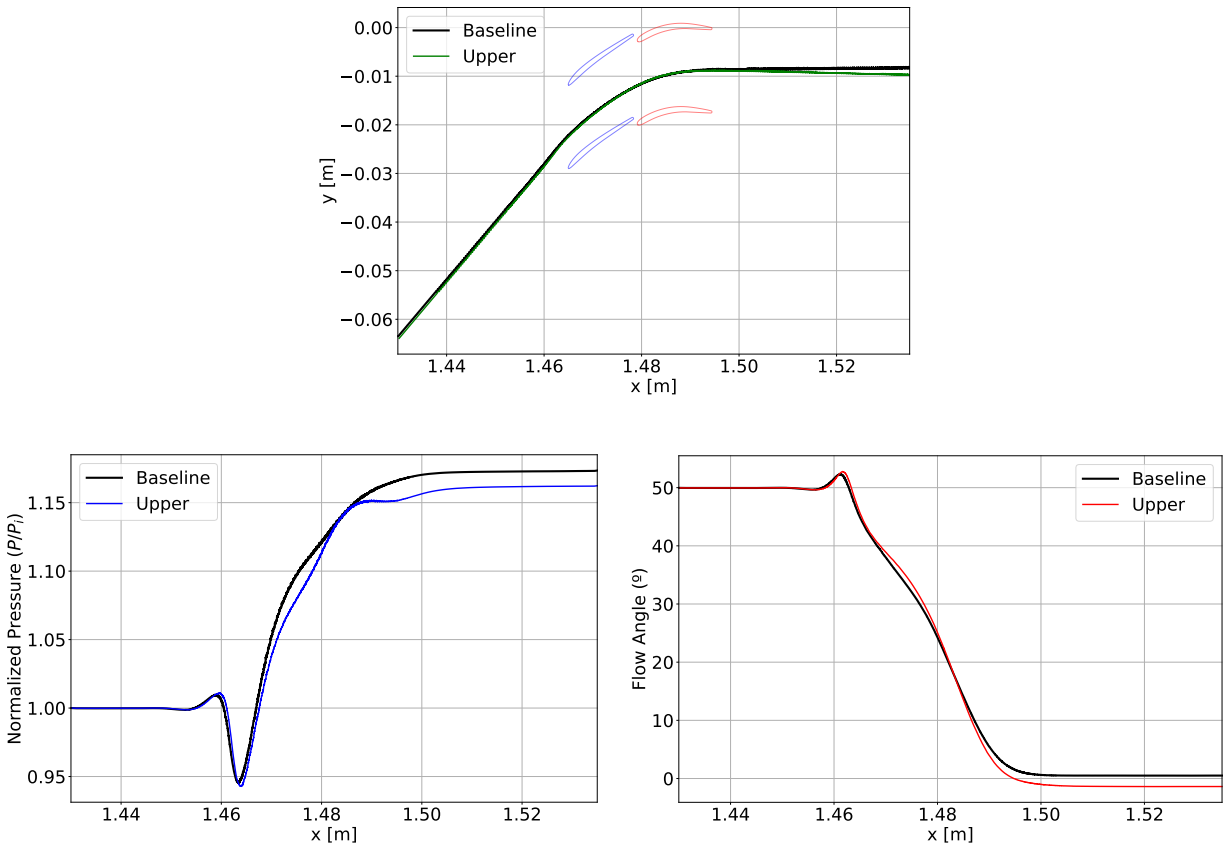

Figure 66. Comparison of the flow quantities represented over streamlines at inlet flow angle of 50º

6.5.5 Wake Analysis

In Figure 67 the pressure loss distribution at the MP2 point is presented. The losses of the wake for inlet flow angles above 50º are smaller than the baseline configuration. However, since the wake is wider, the overall losses are increased. For low inlet flow angles, the wake is smoother but the magnitude of the peak losses is significantly higher than the baseline configuration.

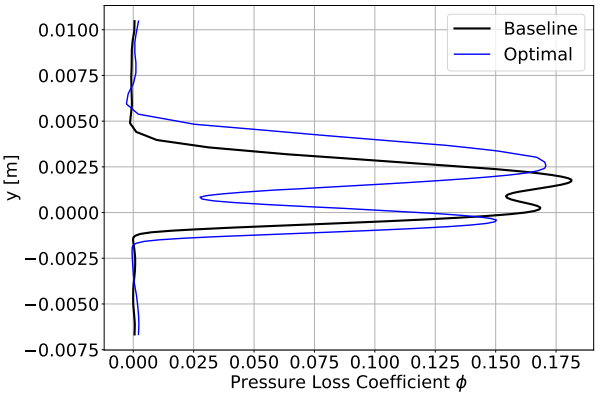

(a) Inlet flow angle of 50º

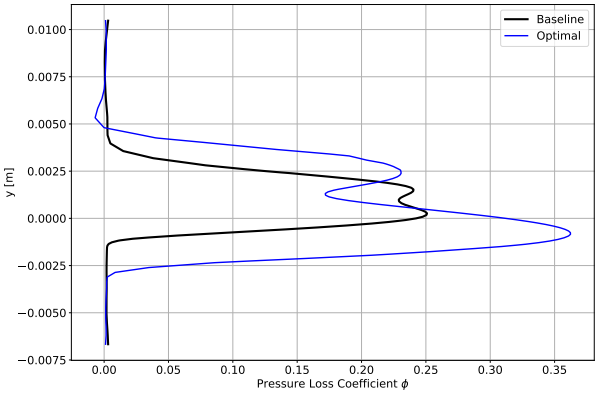

(b) Inlet flow angle of 42º

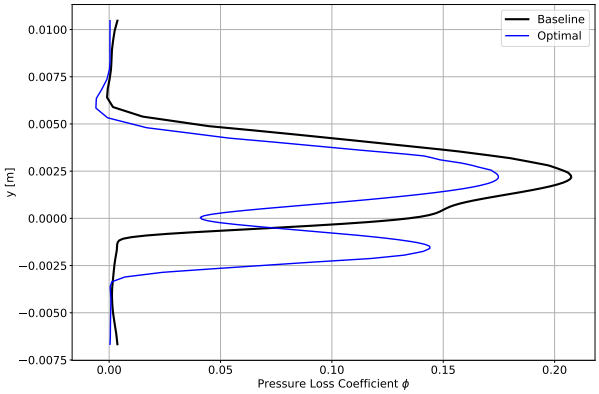

(c) Inlet flow angle of 56º

Figure 67. Comparison between the pressure loss distributions at x = 1.51 of the flow of the baseline and optimized configurations

In Figure 68 the distribution of the exit flow angle at the MP2 point is represented for both configurations. In this case, the flow hasn't been able to be kept within the ±1° range. At very low inlet flow angles, the flow distribution is very fluctuating. This behavior appears because the stage reaches stall.

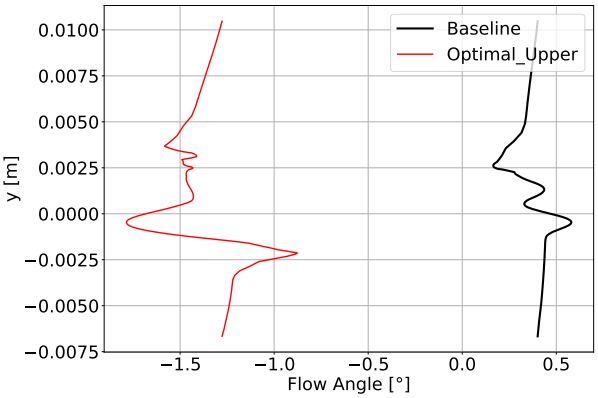

(a) Inlet flow angle of 50º

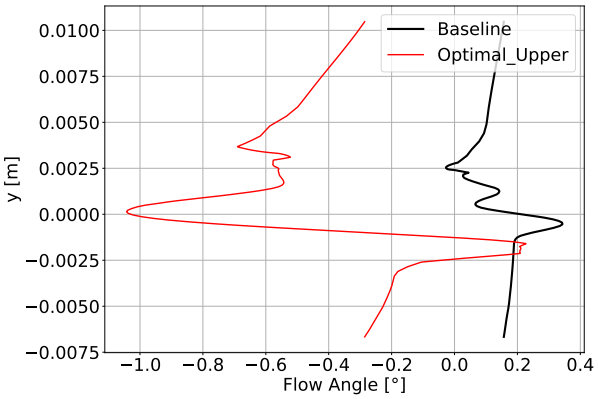

(b) Inlet flow angle of 42º

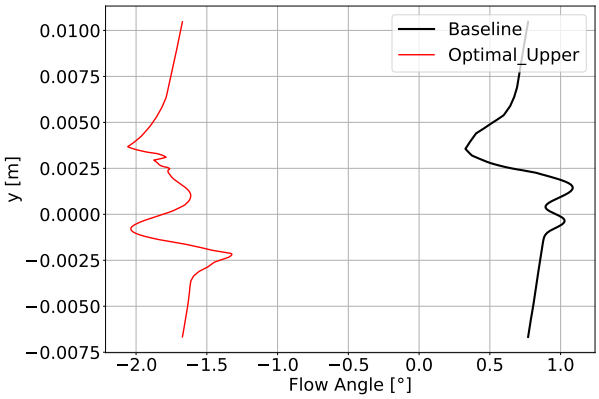

(c) Inlet flow angle of 56º

Figure 68. Comparison between the pressure loss distributions at x = 1.51 of the flow of the baseline and optimized configurations

6.5.6 Turbulence Analysis

In Figure 42 the turbulent kinetic energy of both configurations is presented. The optimal configuration presents a less turbulent wake for inlet flow angles below 50º. Regardless, the wake is still wider. A high turbulent region is present near the TE of the RB of inlet flow angles above 50º.

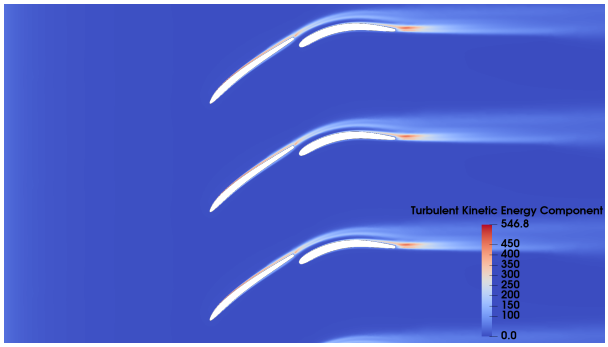

(a) Baseline at inlet flow angle of 50º

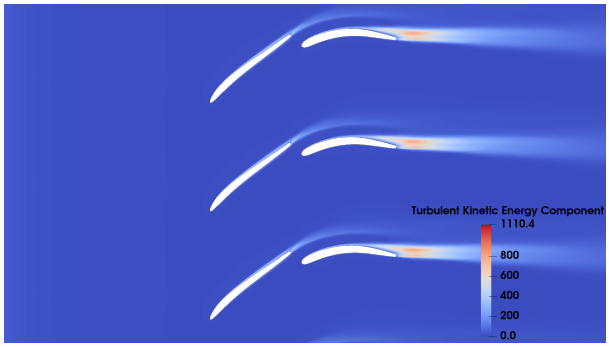

(b) Optimized at inlet flow angle of 50º

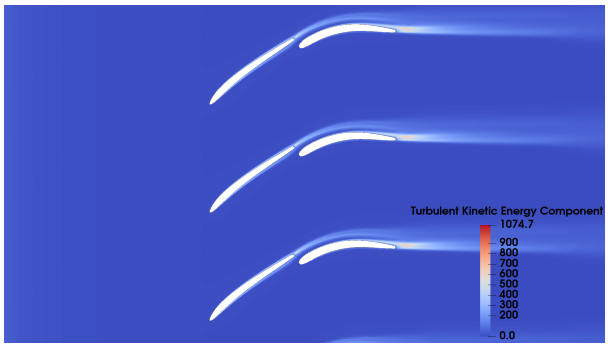

(c) Baseline at inlet flow angle of 42º

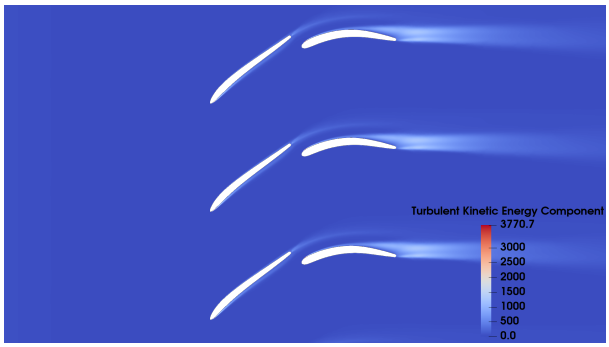

(d) Optimized at inlet flow angle of 42º

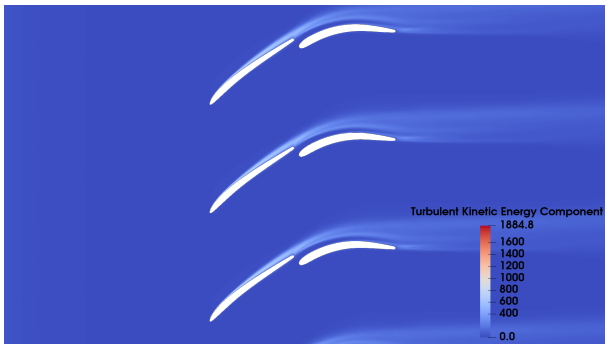

(e) Baseline at inlet flow angle of 56º

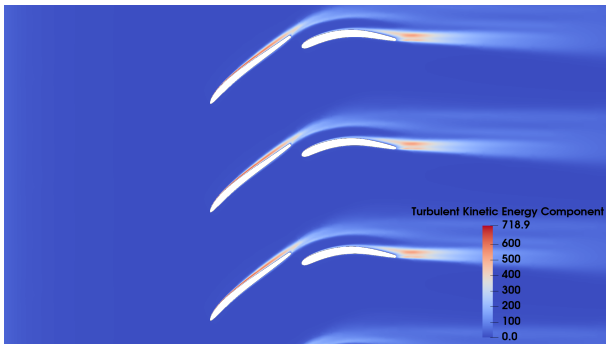

(f) Optimized at inlet flow angle of 56º

Figure 69. Comparison between the turbulent kinetic energy distributions of the flow of the baseline and the optimized configurations at on-design, high and low inlet flow angles

The ratio of turbulent viscosity to laminar viscosity is shown in Figure 70. The viscosity of the wake is less severe for high inlet flow angles, which may explain why the pressure rise of the optimal configuration for high inlet flow angles is more constant. However, for inlet flow angles of 50º and below, the viscosity of the wake is significantly higher. As a result, the flow is significantly slowed down as has been mentioned above.

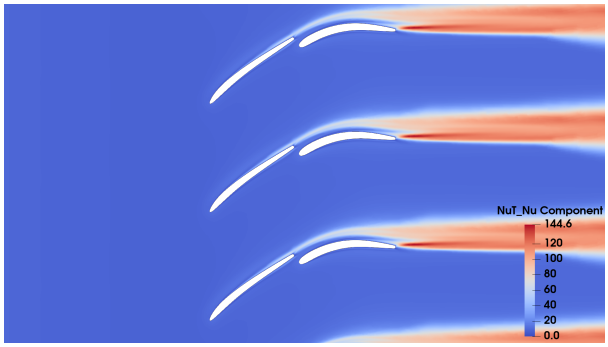

(a) Baseline at inlet flow angle of 50º

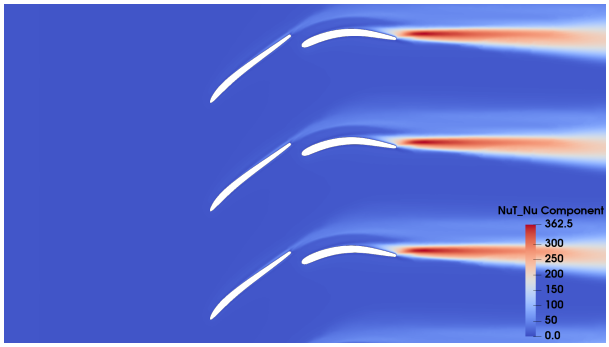

(b) Optimized at inlet flow angle of 50º

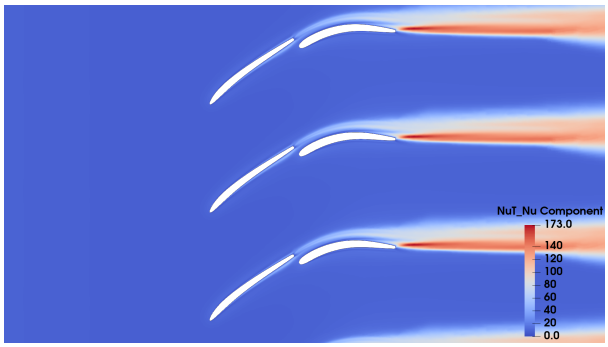

(c) Baseline at inlet flow angle of 42º

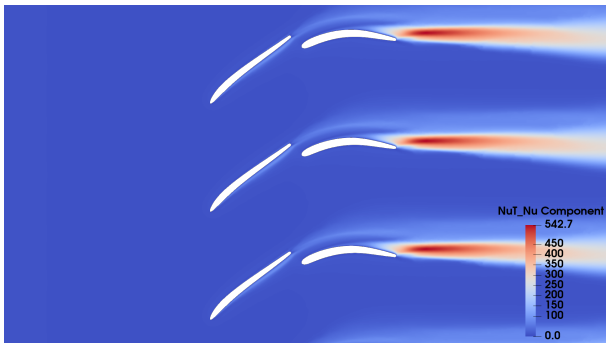

(d) Optimized at inlet flow angle of 42º

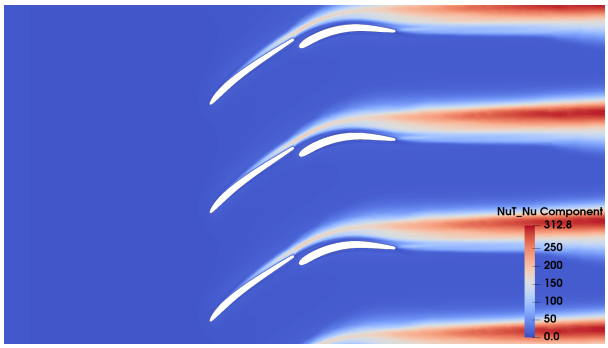

(e) Baseline at inlet flow angle of 56º

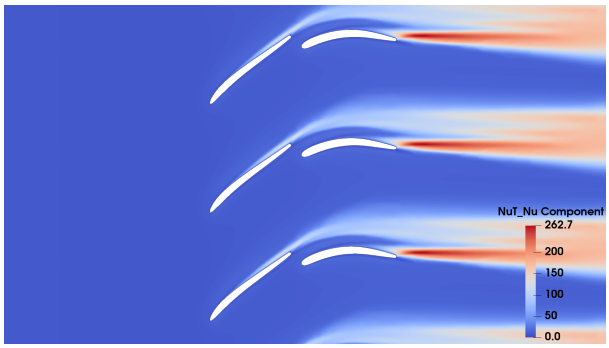

(f) Optimized at inlet flow angle of 56º

Figure 70. Comparison between the turbulent viscosity ratio distributions of the flow of the baseline and the optimized configurations at on-design, high and low inlet flow angles

6.5.7 Very High Inlet Flow Angles

Since no data at very high inlet flow angles is available for the baseline configuration, this section shall present an overview of its influence on the flow parameters.

With positive incidence, the flow detaches from the suction side of the FB and the wake's width increases considerably. The wake is highly turbulent and has a high viscosity. Which means that the flow shall be significantly slowed down.

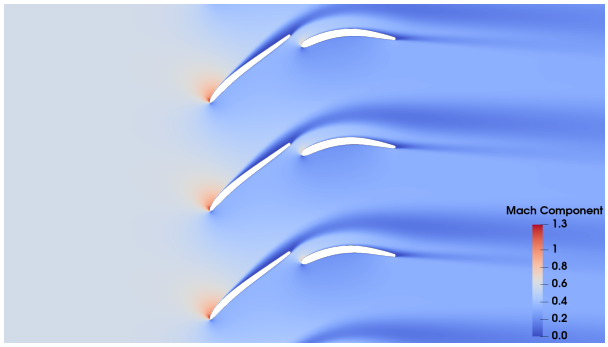

(a) Mach number distribution

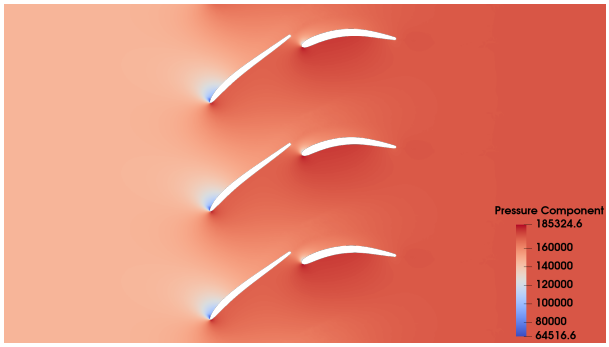

(b) Pressure distribution

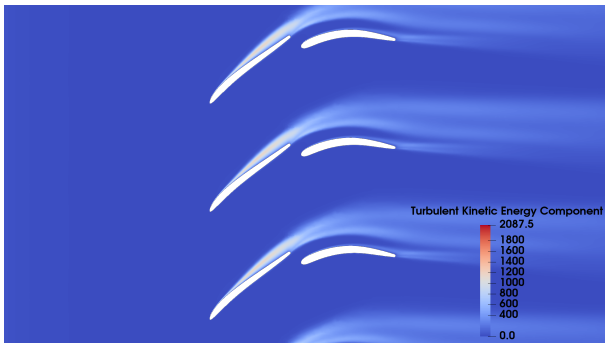

(c) Turbulent kinetic energy distribution

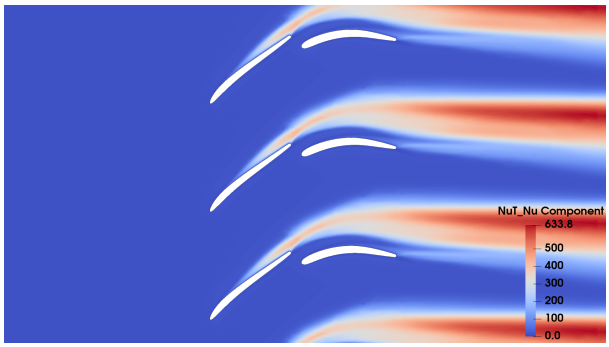

(d) Turbulent viscosity ratio distribution

Figure 71. Flow quantities distributions of the optimized configuration at inlet flow angle of 59º

7 Conclusions

By aiming to optimize the last stage of the Low Pressure Compressor (LPC), the Outlet Guide Vane (OGV), the present work has focused on studying the flow at different configurations for a tandem blade setup.

The optimization approach has used relative position and shape geometry as parameters to maximize the performance of the tandem blades.

Two optimization targets have been set: a performance optimization which minimized the on-design pressure losses for an inlet flow angle of 50º and a working range optimization which maximized the working range of the OGV. The later optimization has required a further refinement of the upper bound range due to a shift of the polar towards lower inlet flow angles. Thus, a third optimization has been required. The last optimization has maximized the upper bound range of the polar to study the flow at high inlet flow angles.

Several quantities have been monitored during the optimization process, such as the pressure loss coefficient for different inlet flow angles, the exit flow angle and the working range (defined as the range where the losses are lower than two times those of the reference angle of 50º), among others.

The outputs of the first optimization have shown that by having an axial overlap (AO) about 2% and a percentage pitch (PP) about 93%, as well as an optimized geometry that allows a sharp turning of the flow, can significantly reduce the pressure losses across the tandem stage while maintaining an axial exit flow and an acceptable working range.

Even though the second optimization has been successful, its outputs have not been interesting from the design point of the OGV because the range where high-pressure ratios are obtained has been minimized. Last but not least, the last optimization has successfully increased the upper bound of the polar by increasing the axial gap between the blades and reducing the percentage pitch to 85 - 90%, but this has come at the cost of other critical performance targets such as the pressure losses or the exit flow angle of the on-design configuration, which have increased slightly beyond the expected margins.

It's been concluded that the OGV is a complex regime with very sensitive flow, where slight variations on key parameters such as the relative position of the tandem blades and their respective shapes may cause a substantial impact on the flow.

A tool that allows to control the relative position of the tandem blades and their geometry has been developed. It is meant as a preliminary tool for the design of the OGV in 2D. Thus, it's a starting point for future implementation of 3D simulations and experimentation.

8 Future Work

The three optimizations performed in this project have not used the work of Mathias Brach and Thibaut Dupont [1]. Their work focused on a varying OGV which could rotate the FB using certain rotation points to properly align it with the flow for different inlet flow angles.

By combining the work performed in this project with theirs, a complete tool that allows to find the optimal geometry for maximizing the performance of the OGV could be obtained. Hence, a preliminary 2D optimal geometry could be achieved. This geometry would be a starting point for future 3D simulation and optimization and later testing.

A good starting point for the combined tool would be to refine the geometry that has been obtained from the performance optimization.

Additionally, it is important to note that the current work has focused on three optimization targets while monitoring some other performance quantities. However, other optimization criteria could have been selected, such as the linearity of the pressure rise or a target loading factor of 0.5, which equally distributed the load between both blades. Alternatively, the load on the rear blade could be set to be the higher one because it is shielded from varying inlet flow angle conditions thanks to the boundary layer of the front blade.

Finally, some refinements could be implemented on the automatic meshing process as well as on the tracking of the CFL number to ensure a more consistent output of the results.

9 Appendix

9.1 Front Blade Shape Modification

The effect of altering the defining parameters of the geometry on the monitored parameters is shown in the following Figures. It may be appreciated that the initial considered range for the parameters is too large, thus not many conclusions may be drawn from the results.

In Figure 72, the effect of the chord scale on the flow physics is shown.

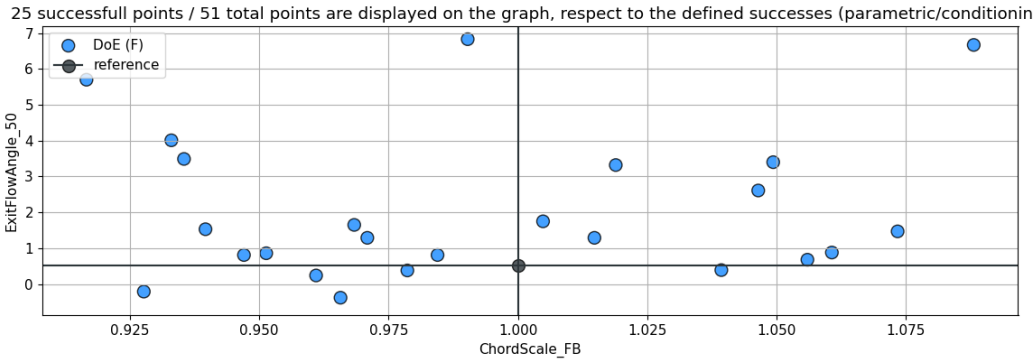

(a) Exit Flow Angle in terms of FB chord scale

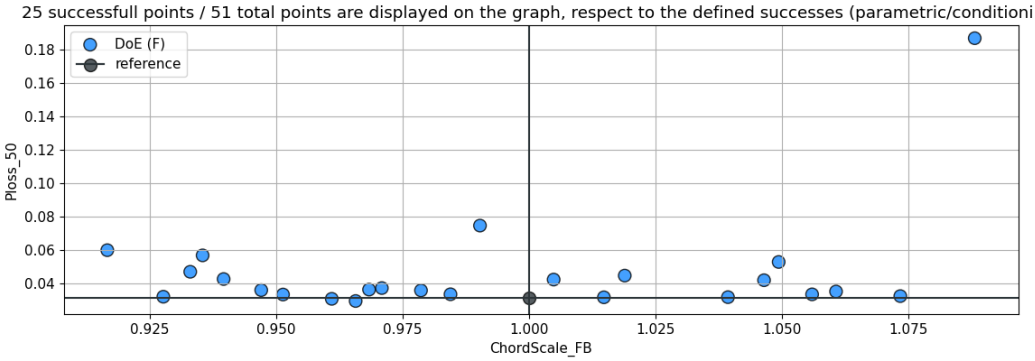

(b) ϕ in terms of FB chord scale

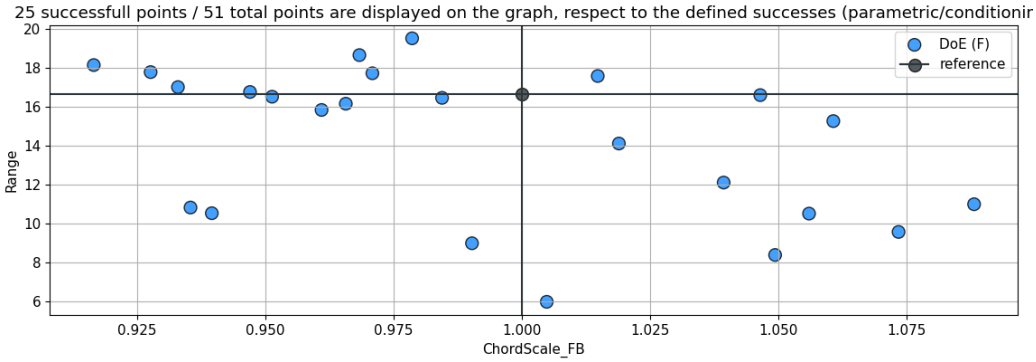

(c) Range in terms of FB chord scale

Figure 72. Effect of chord scale on flow physics

In Figure 73, the effect of the stagger angle on the flow physics is shown.

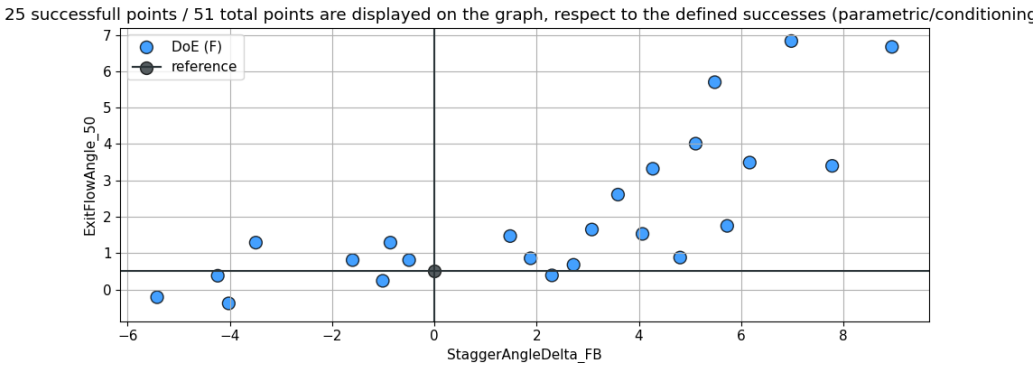

(a) Exit Flow Angle in terms of FB stagger deflection

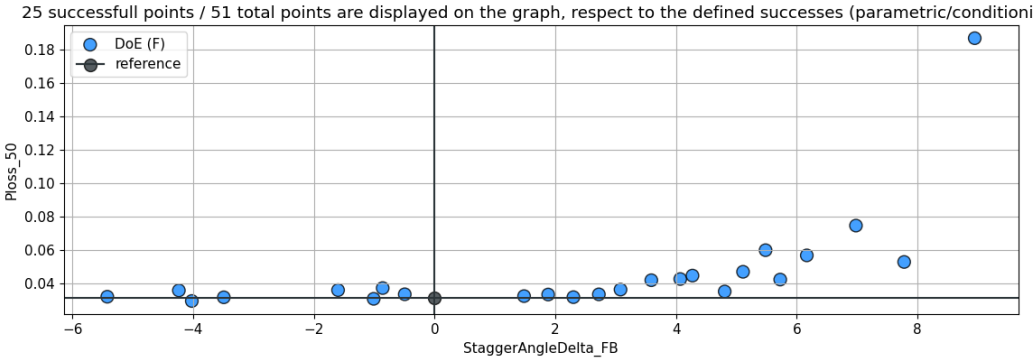

(b) ϕ in terms of FB stagger deflection

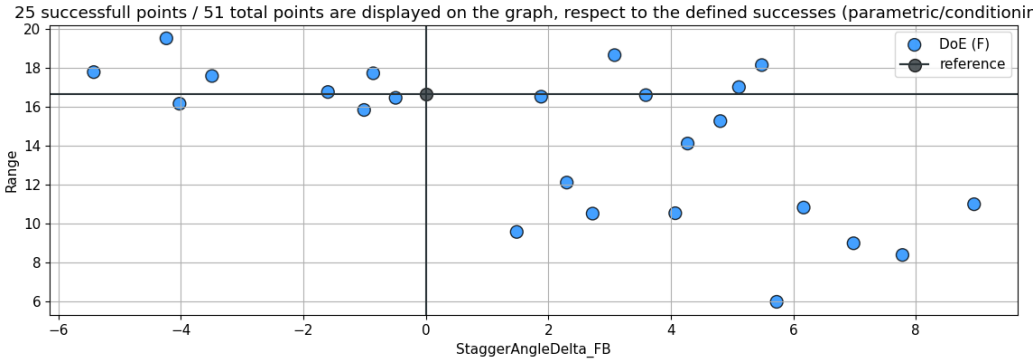

(c) Range in terms of FB stagger deflection

Figure 73. Effect of stagger deflection on flow physics

In Figure 74, the effect of the LE's angle deflection on the flow physics is shown.

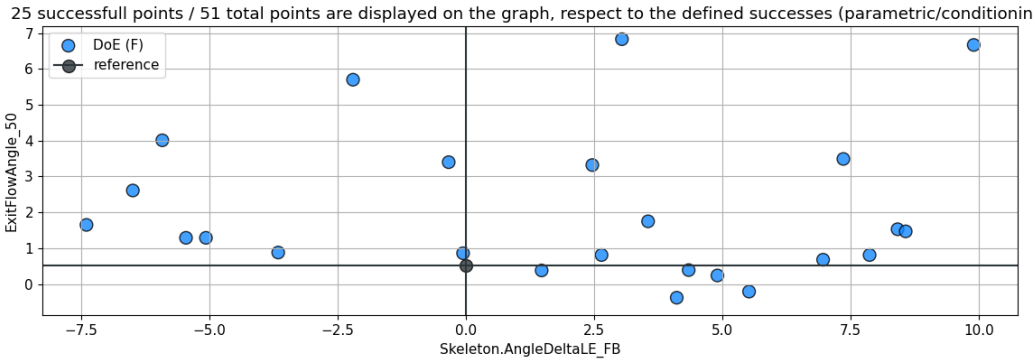

(a) Exit Flow Angle in terms of LE angle deflection

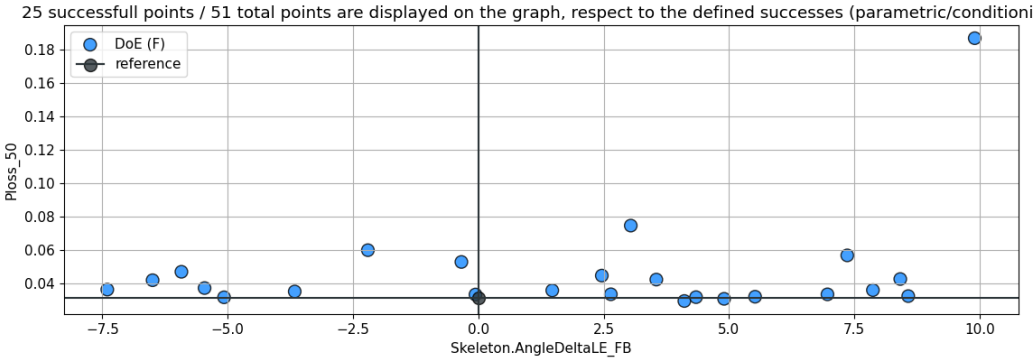

(b) ϕ in terms of LE angle deflection

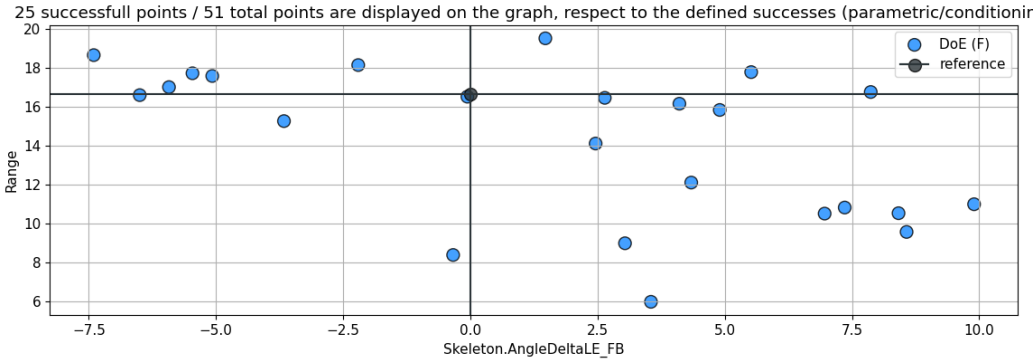

(c) Range in terms of LE angle deflection

Figure 74. Effect of LE angle deflection on flow physics

In Figure 75, the effect of the TE's angle deflection on the flow physics is shown.

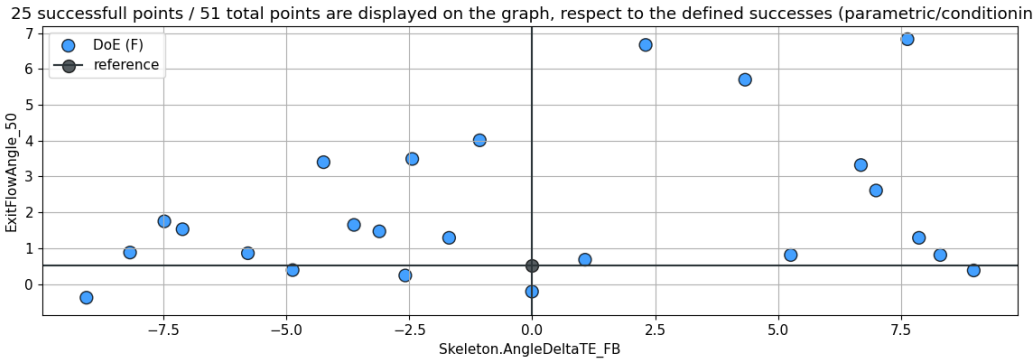

(a) Exit Flow Angle in terms of TE angle deflection

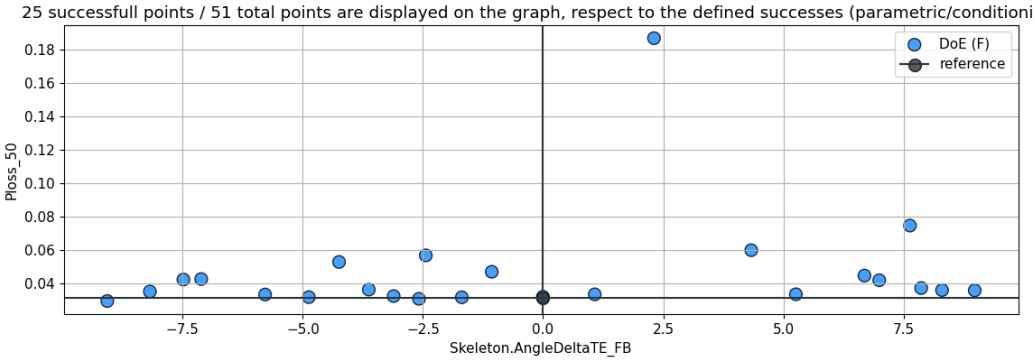

(b) ϕ in terms of TE angle deflection

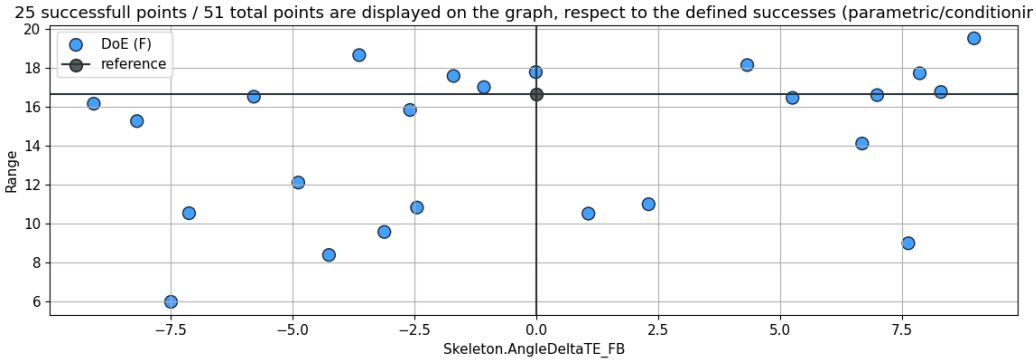

(c) Range in terms of TE angle deflection

Figure 75. Effect of TE angle deflection on flow physics

9.2 Rear Blade Shape Modification

In this section, an analysis similar to that which has been conducted on the FB is presented.

In Figure 76, it may be appreciated that even with a shift of 30% of the blade's thickness, the geometry does not vary that much. A similar conclusion may be drawn from the maximum thickness analysis. From Figure 77 it may be concluded that these parameters don't have a major influence on the physics of the flow. Thus, they have been ruled out as defining parameters of the optimization chain.

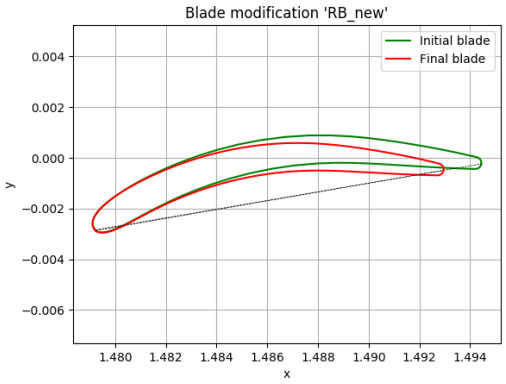

(a) RB comparison with -10% Chord Length

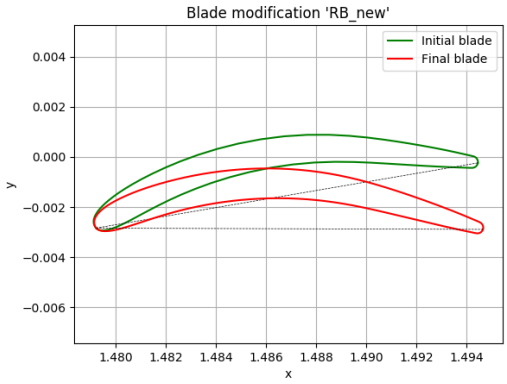

(b) RB comparison with -10º Stagger Angle

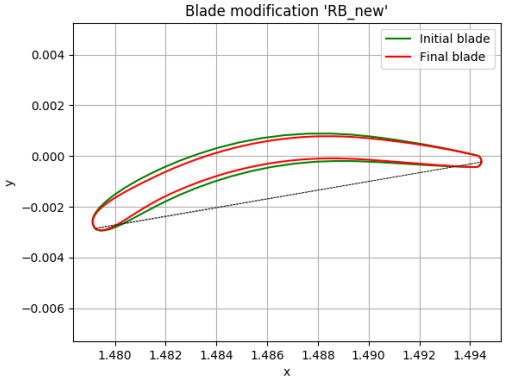

(c) RB comparison with -30% Thickness

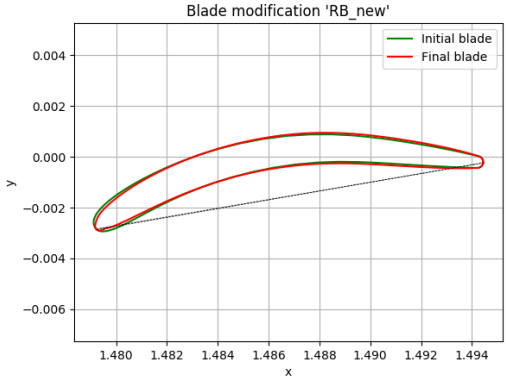

(d) RB comparison with +30% Thickness Shift

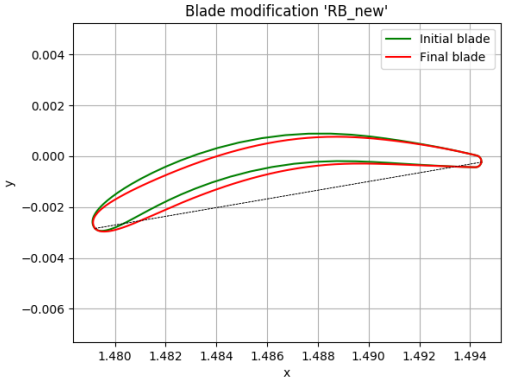

(e) RB comparison with -10º Metal Angle at LE

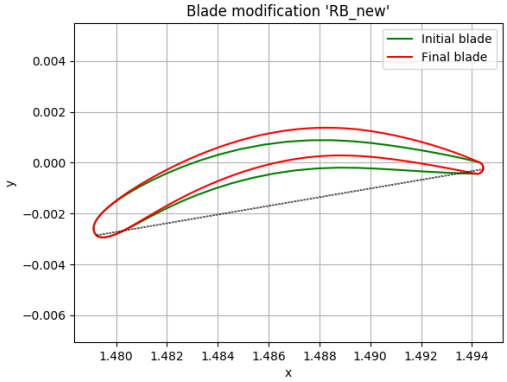

(f) RB comparison with -10º Metal Angle at TE

Figure 76. Rear Blade Shape modifications

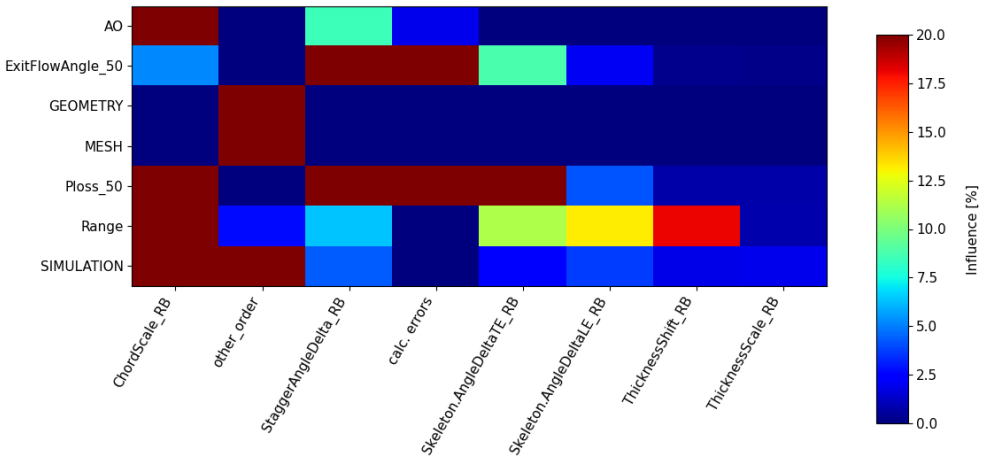

Figure 77. Global Sensitivity Analysis on Rear Blade

The effect of altering the defining parameters of the geometry on the monitored parameters is shown in the following Figures. It may be appreciated that the initial considered range for the parameters is too large, thus not many conclusions may be drawn from the results.

In Figure 78, the effect of the chord scale on the flow physics is shown.

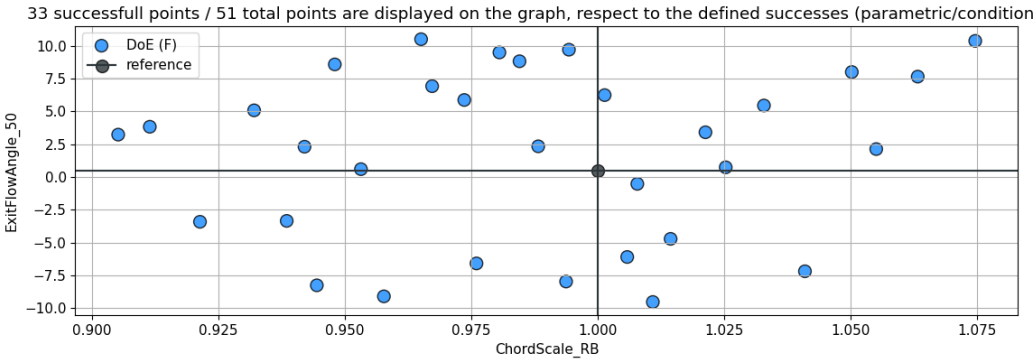

(a) Exit Flow Angle in terms of RB chord scale

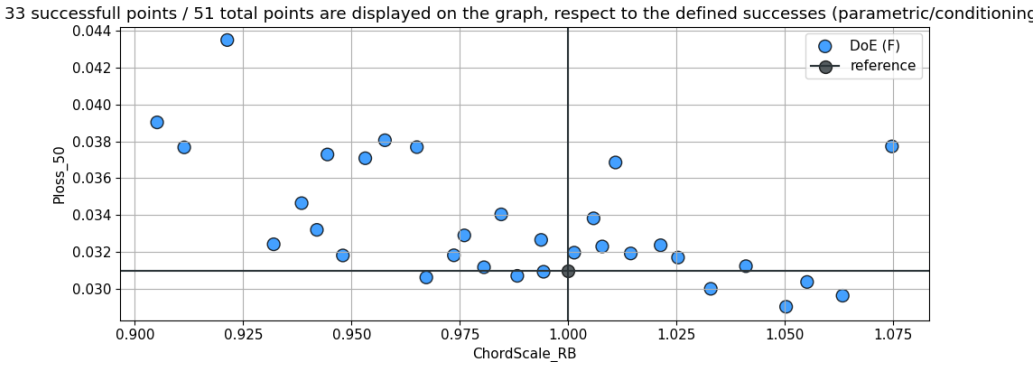

(b) ϕ in terms of RB chord scale

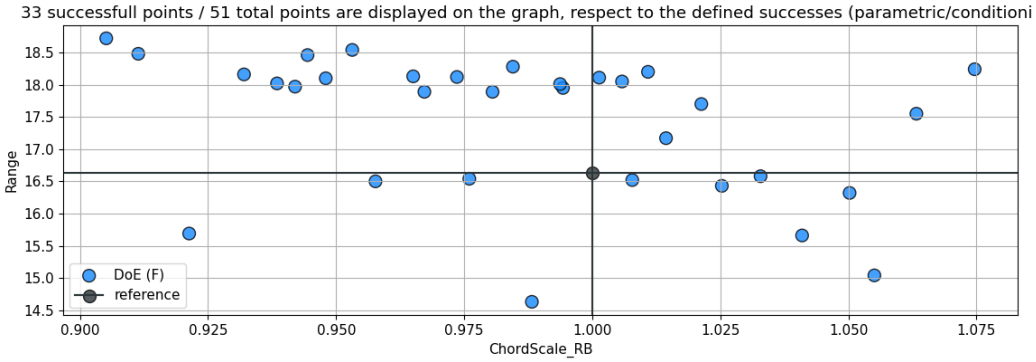

(c) Range in terms of RB chord scale

Figure 78. Effect of chord scale on flow physics

In Figure 79, the effect of the stagger angle on the flow physics is shown.

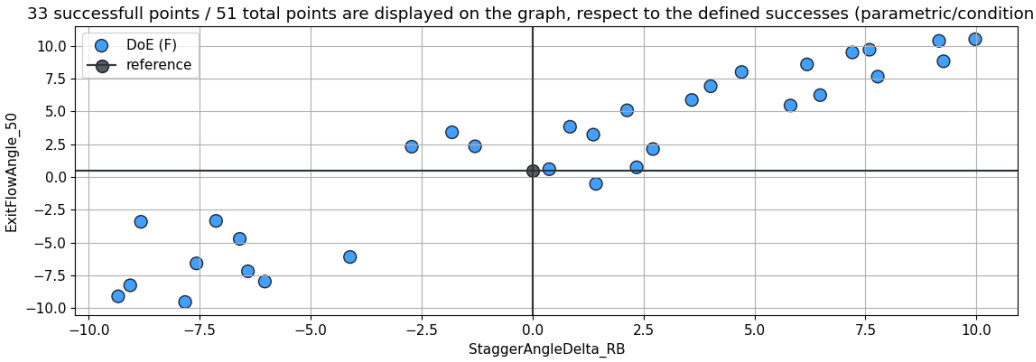

(a) Exit Flow Angle in terms of RB stagger deflection

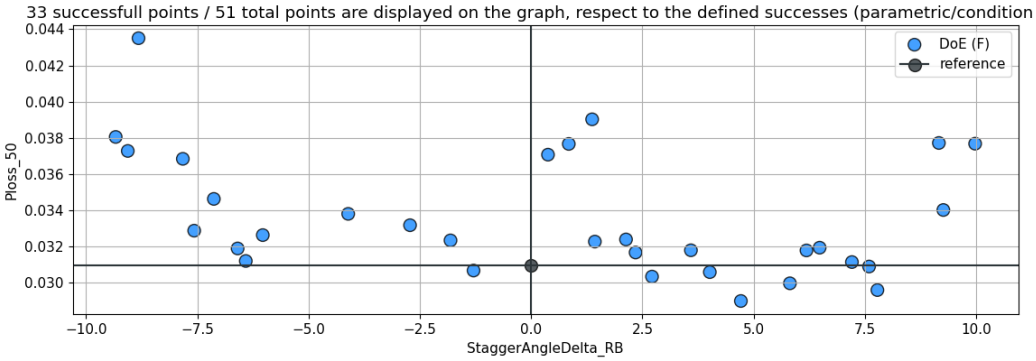

(b) ϕ in terms of RB stagger deflection

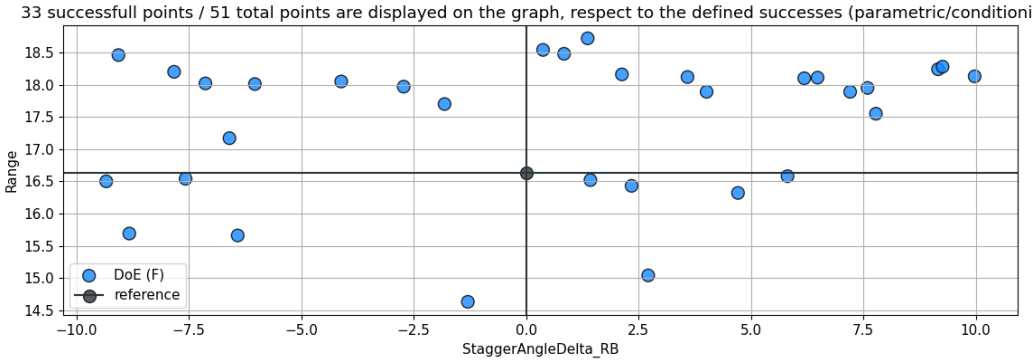

(c) Range in terms of RB stagger deflection

Figure 79. Effect of stagger deflection on flow physics

In Figure 80, the effect of the LE's angle deflection on the flow physics is shown.

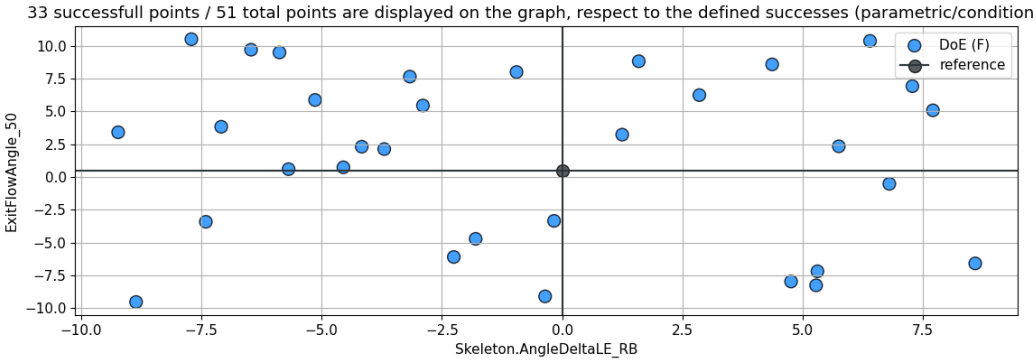

(a) Exit Flow Angle in terms of LE angle deflection

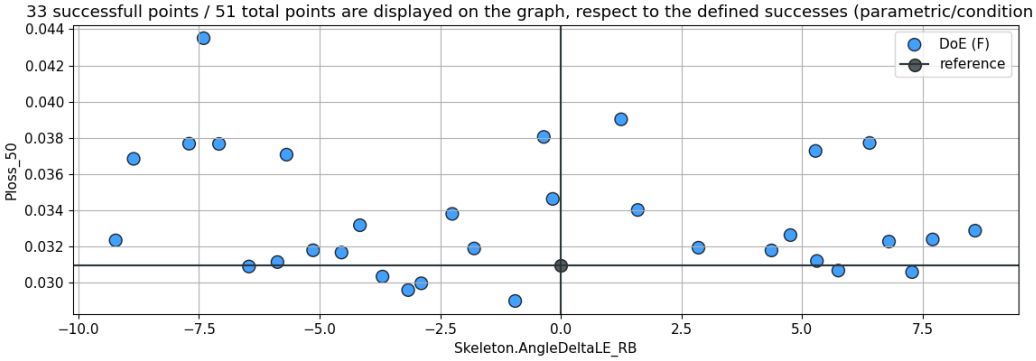

(b) ϕ in terms of LE angle deflection

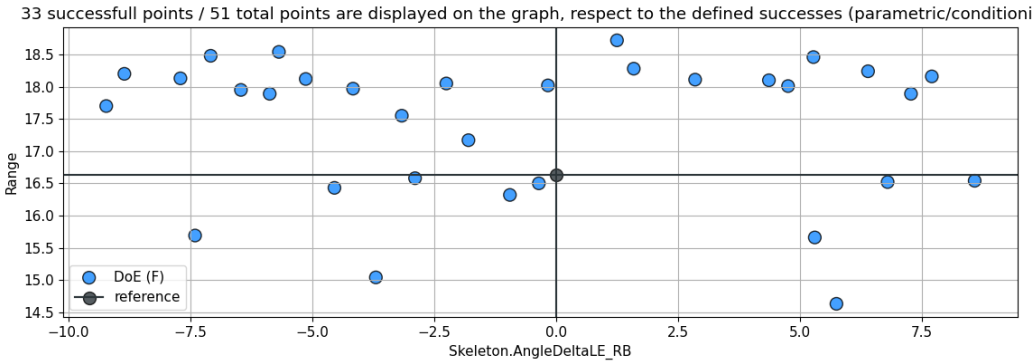

(c) Range in terms of TE angle deflection

Figure 80. Effect of LE angle deflection on flow physics

In Figure 81, the effect of the TE's angle deflection on the flow physics is shown.

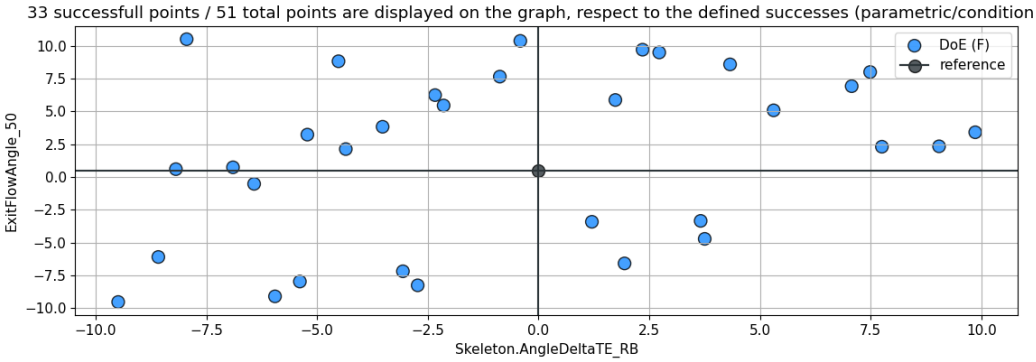

(a) Exit Flow Angle in terms of TE angle deflection

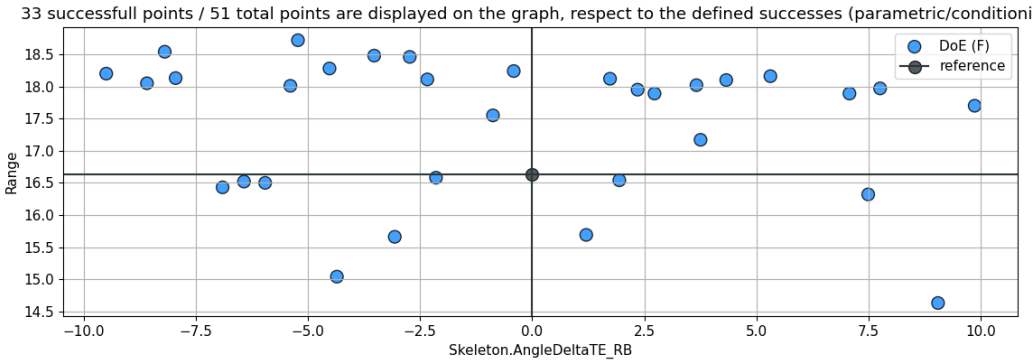

(b) ϕ in terms of TE angle deflection

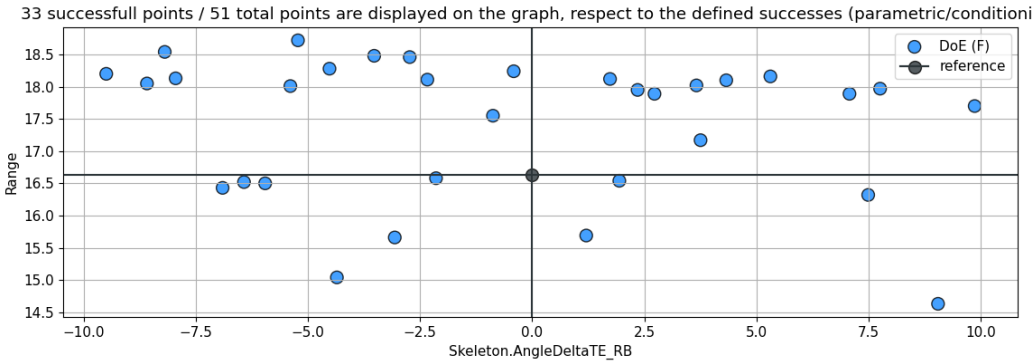

(c) Range in terms of TE angle deflection

Figure 81. Effect of TE angle deflection on flow physics

9.3 Performance Optimization

The results of the first optimization are presented in this section.

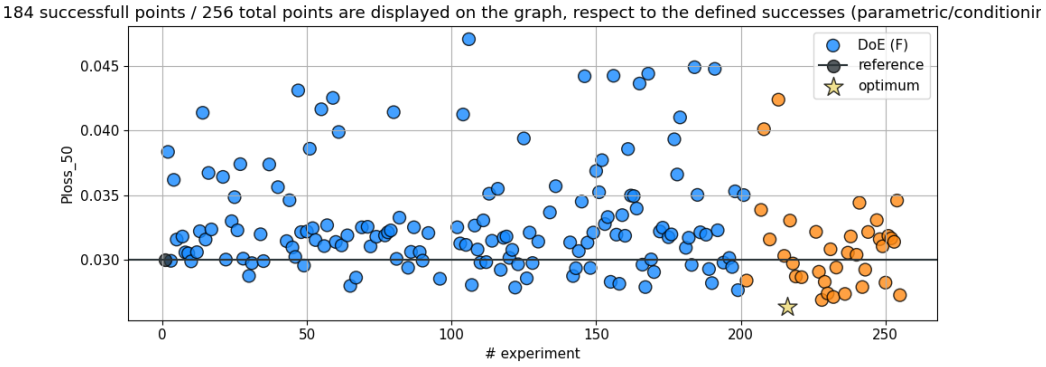

(a) Pressure losses

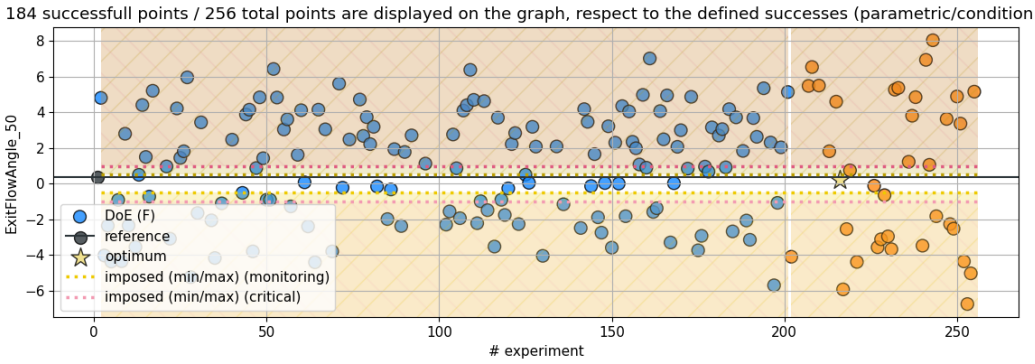

(b) Exit flow angle

Figure 82. Performance of flow quantities of the test cases

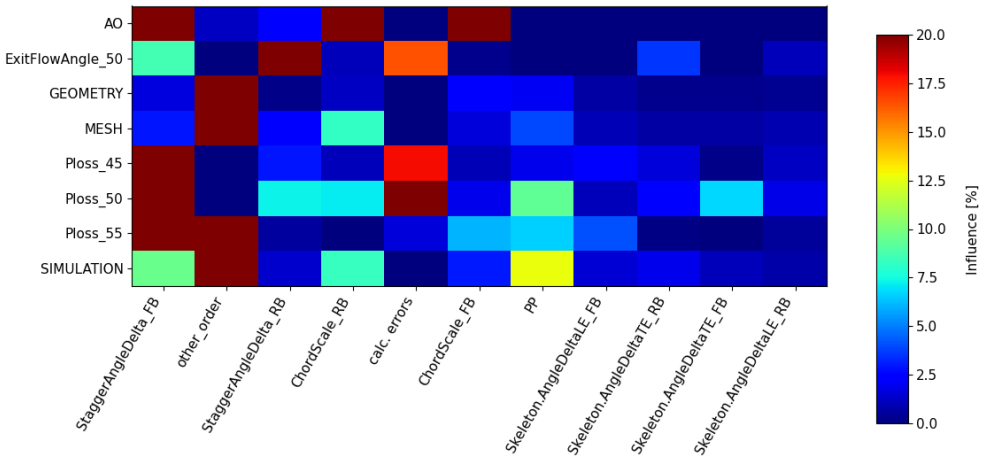

Figure 83. Global Sensitivity Analysis of the optimization

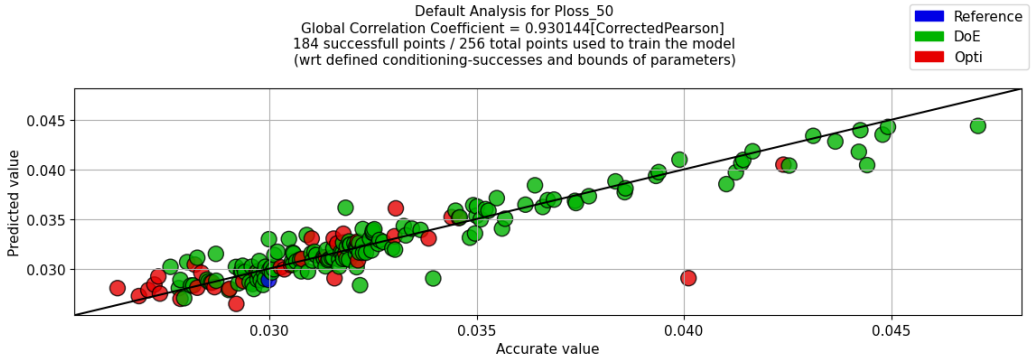

(a) Pressure losses

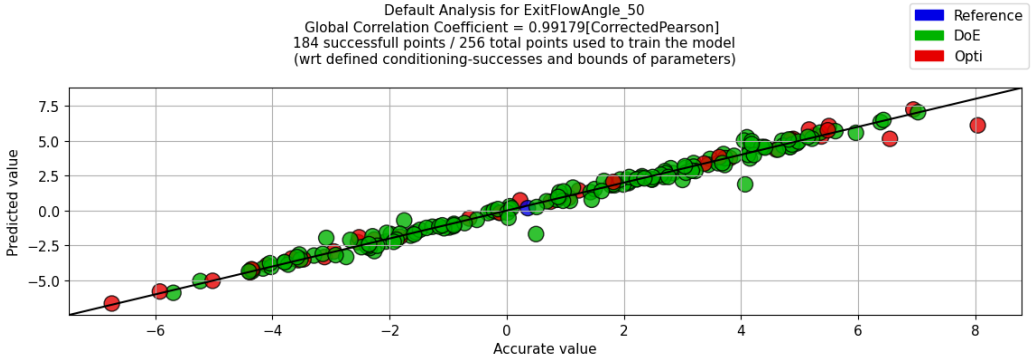

(b) Exit flow angle

Figure 84. Model quality of flow quantities of the test cases

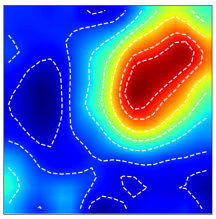

(a) Pressure losses

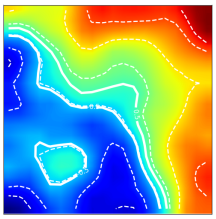

(b) Exit flow angle

Figure 85. Sensitivity of model for flow responses of the test cases

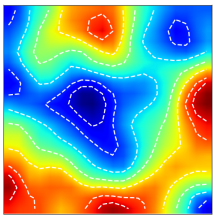

(a) Chordscale FB

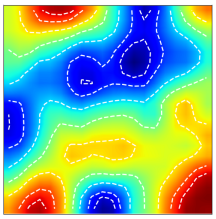

(b) Chordscale RB

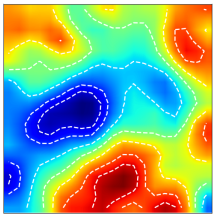

(c) LE FB

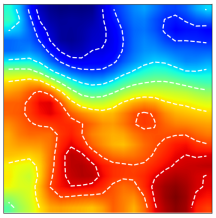

(d) LE RB

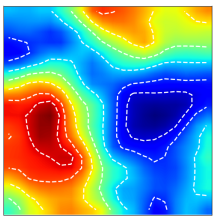

(e) PP

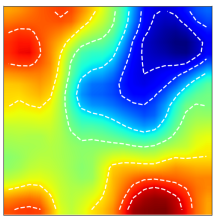

(f) AO

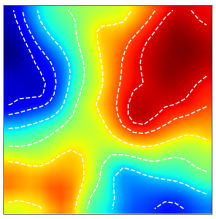

(g) Stagger FB

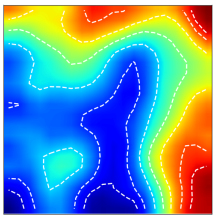

(h) Stagger RB

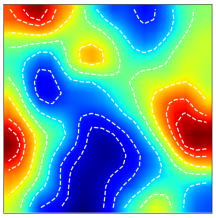

(i) TE FB

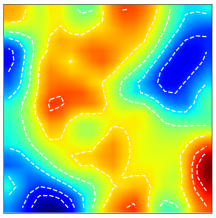

(j) TE RB

Figure 86. Sensitivity of model for flow inputs of the test cases

9.4 Range Optimization

The results of the second optimization are presented in this section.

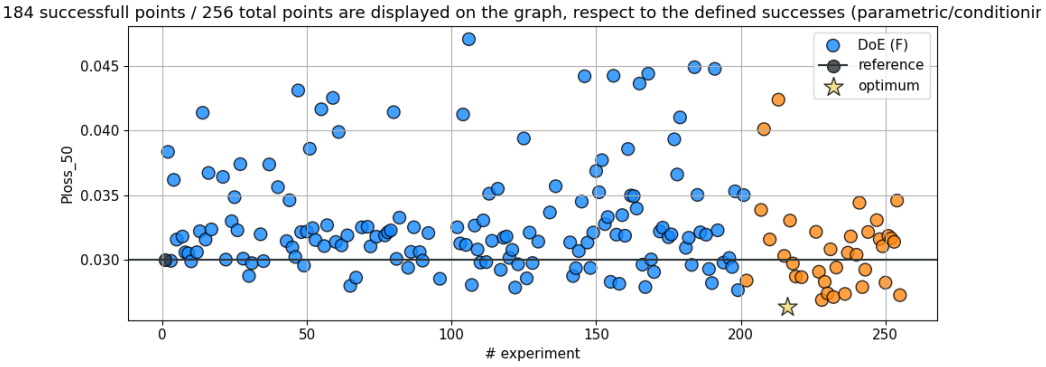

(a) Pressure losses

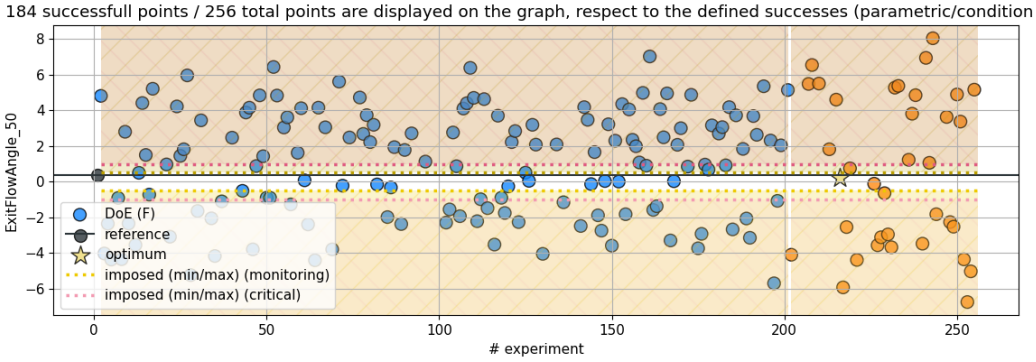

(b) Exit flow angle

Figure 87. Performance of flow quantities of the test cases

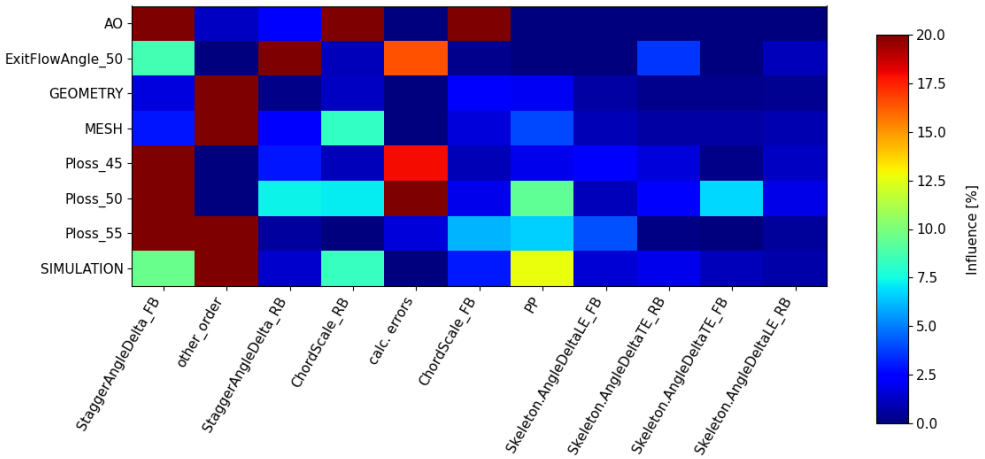

Figure 88. Global Sensitivity Analysis of the optimization

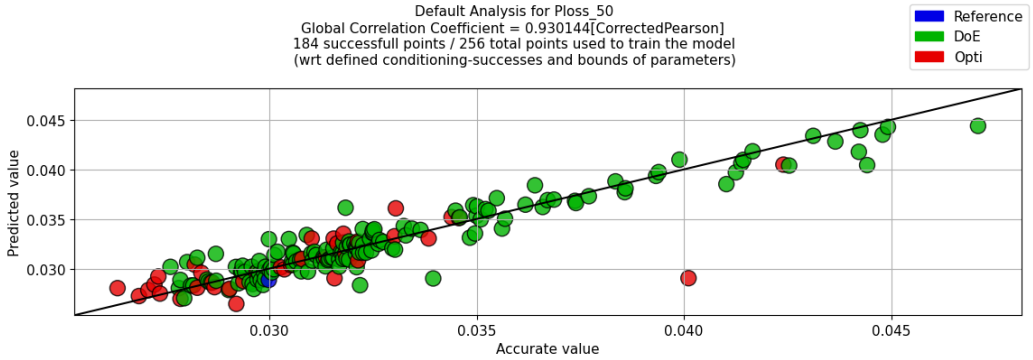

(a) Pressure losses

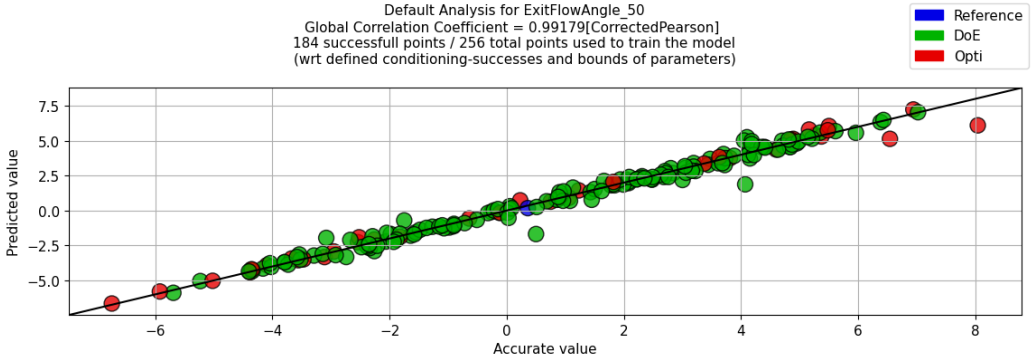

(b) Exit flow angle

Figure 89. Model quality of flow quantities of the test cases

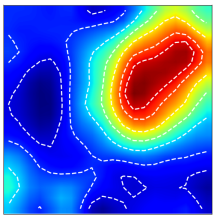

(a) Pressure losses

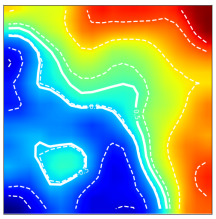

(b) Exit flow angle

Figure 90. Sensitivity of model for flow responses of the test cases

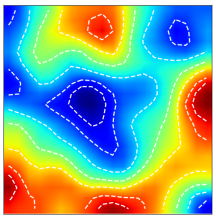

(a) Chordscale FB

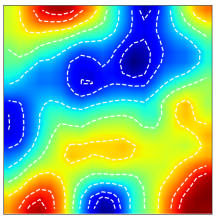

(b) Chordscale RB

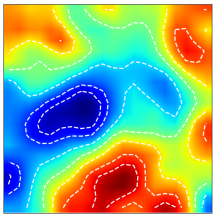

(c) LE FB

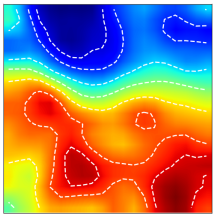

(d) LE RB

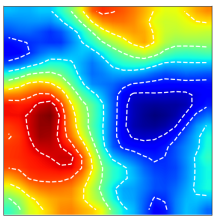

(e) PP

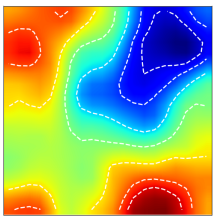

(f) AO

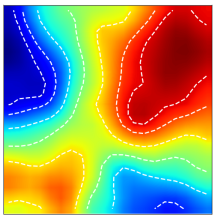

(g) Stagger FB

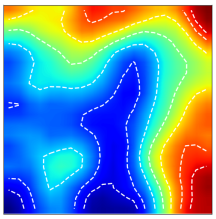

(h) Stagger RB

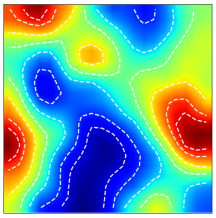

(i) TE FB

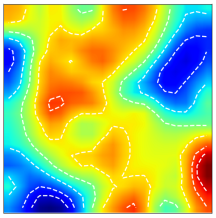

(j) TE RB

Figure 91. Sensitivity of model for flow inputs of the test cases

9.5 Upper Bound Optimization

The results of the last optimization are presented in this section.

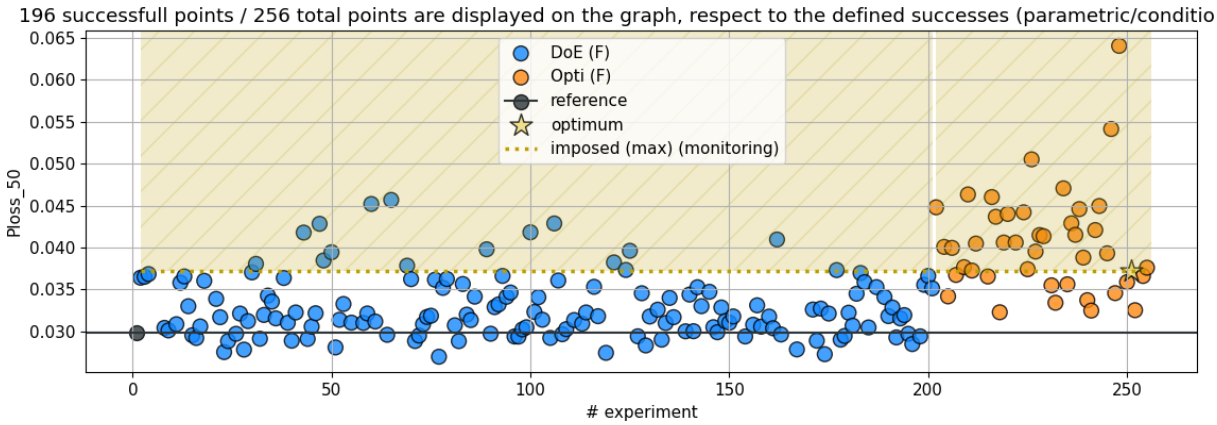

Figure 92. Pressure losses of the test cases

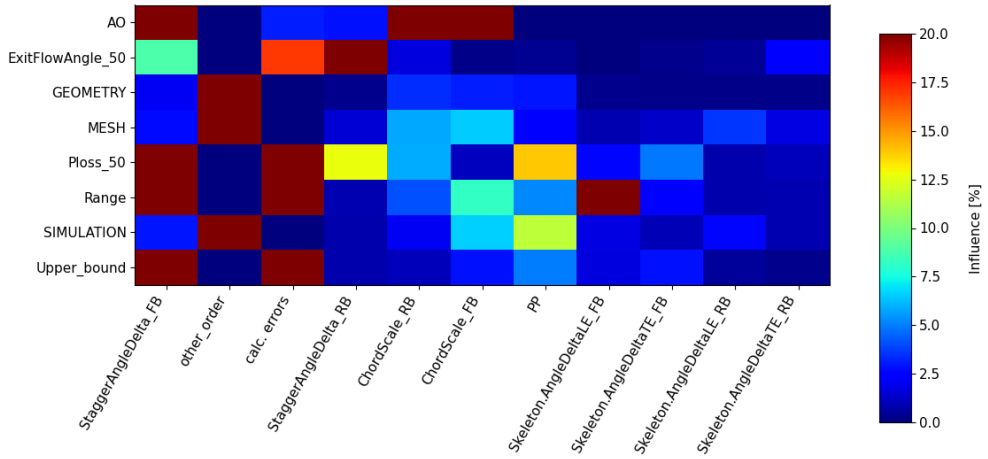

Figure 93. Global Sensitivity Analysis of the optimization

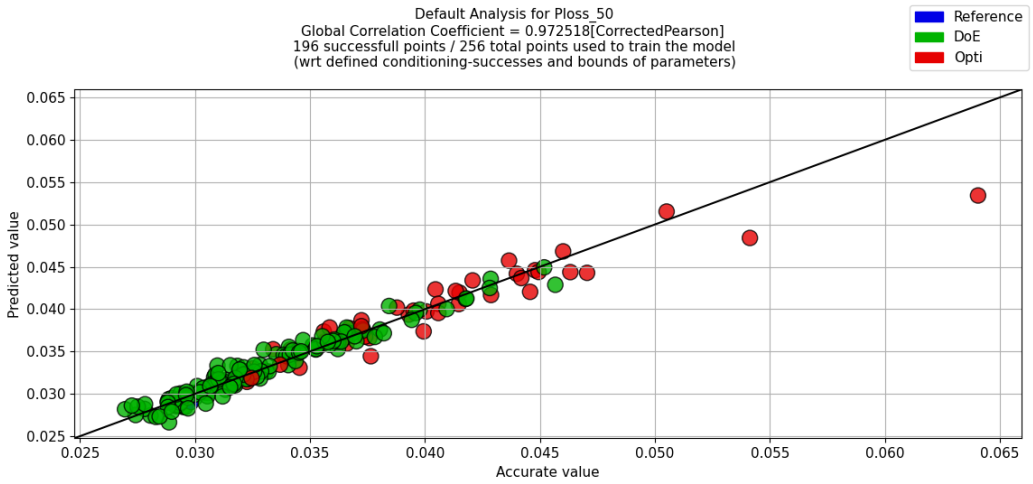

(a) Pressure losses

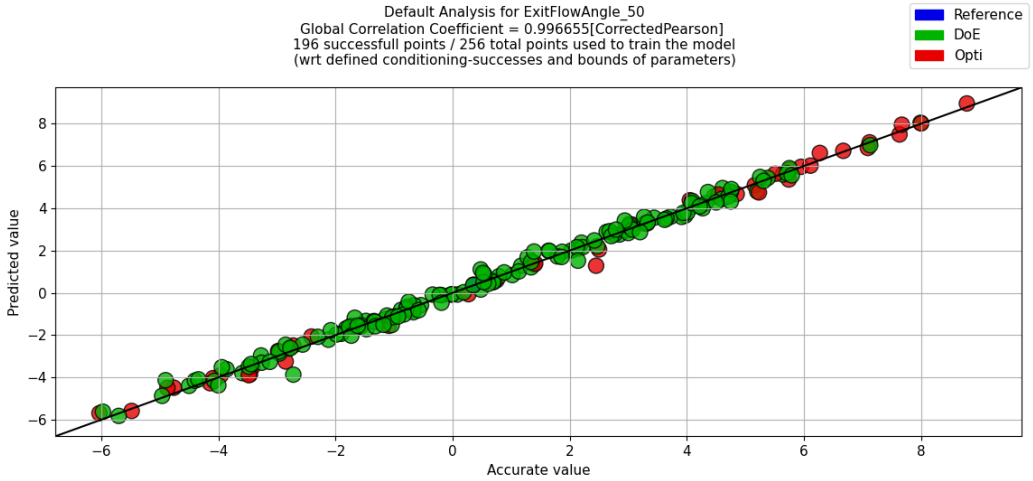

(b) Exit flow angle

Figure 94. Model quality of flow quantities of the test cases

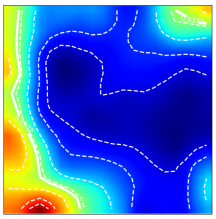

(a) Pressure losses

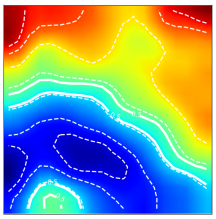

(b) Exit flow angle

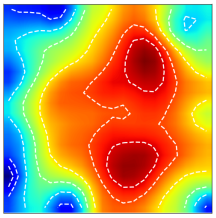

(c) Pressure losses

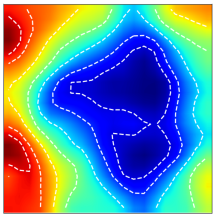

(d) Exit flow angle

Figure 95. Sensitivity of model for flow responses of the test cases

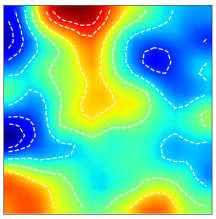

(a) Chordscale FB

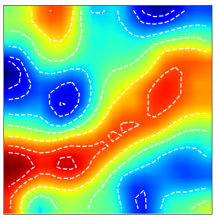

(b) Chordscale RB

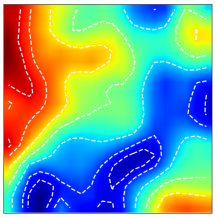

(c) LE FB

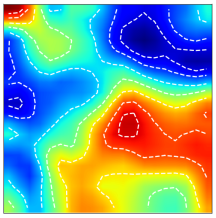

(d) LE RB

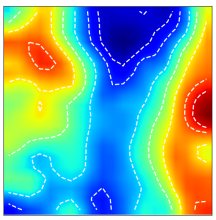

(e) PP

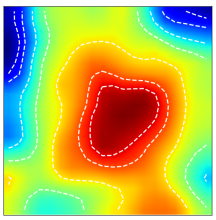

(f) AO

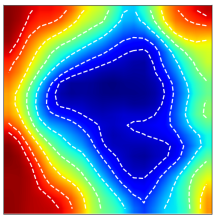

(g) Stagger FB

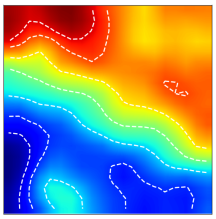

(h) Stagger RB

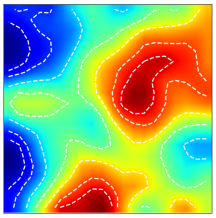

(i) TE FB

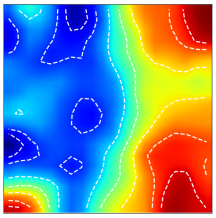

(j) TE RB

Figure 96. Sensitivity of model for flow inputs of the test cases

References

[1] Brach, M. (2024). *Numerical investigation of a variable tandem outlet guide vane in a low pressure compressor cascade* [Master's thesis, University of Liège].

[2] Ritchie, H. (2024). What share of global co2 emissions come from aviation? *Our World in Data*. https://ourworldindata.org/global-aviation-emissions

[3] Brinkle, C. (2024). Aerospace sustainability: Benefits, challenges, and examples. *Thomas Publishing Company*. https://www.thomasnet.com/insights/aerospace-sustainability/

[4] PACE. (2023). A guide to the paris agreement for the aviation sector. *PACE*. https://www.pace-esg.com/academy/a-guide-to-the-paris-agreement-for-the-aviation-sector/

[5] Schlaps, R., & Shahpar, S. (2014). Automatic three-dimensional optimisation of a modern tandem compressor vane. *Proceedings of ASME Turbo Expo 2014: Turbine Technical Conference and Exposition*. https://doi.org/10.13140/2.1.2633.6007

[6] Hergt, A., & Siller, U. (2016). About subsonic compressor tandem aerodynamics - a fundamental study. *16th International Symposium on Transport Phenomena and Dynamics of Rotating Machinery*. https://hal.science/hal-01884245v1

[7] Singh, A., & Mistry, C. S. (2024). Investigations on design space for highly loaded tandem bladed axial flow rotor- novel stator for low-speed compressor research facility. *Journal of Applied Fluid Mechanics*, *17*(10), 2245–2265. https://doi.org/10.47176/jafm.17.10.2521

[8] Liu, B., Zhang, C., An, G., Fu, D., & Yu, X. (2022). Using tandem blades to break loading limit of highly loaded axial compressors. *Chinese Journal of Aeronautics*, *35*(4), 165–175. https://doi.org/10.1016/j.cja.2021.07.031

[9] Leishman, J. G. (2022). Introduction to aerospace flight vehicles. *Embry-Riddle Aeronautical University*. https://doi.org/10.15394/eaglepub.2022.1066.n33

[10] Mattingly, J. D. (2006). *Elements of propulsion: Gas turbines and rockets* (2nd ed.). American Institute of Aeronautics; Astronautics, Inc.

[11] Hillewaert, K. (2025). *Aerospace propulsion - theory*. University of Liège.

[12] Schluer, C., Böhle, M., & Cagna, M. (2009). Numerical investigation of the secondary flows and losses in a high-turning tandem compressor cascade. *European Turbomachinery Conference*, *8*. https://www.researchgate.net/publication/281281861_Numerical_Investigation_of_the_Secondary_Flows_and_Losses_in_a_High-Turning_Tandem_Compressor_Cascade

[13] Online, C. (2007). Isentropic mach number. *CFD Online*. https://cfd-online.com/Wiki/Isentropic_Mach_number

[14] Hirsch, C. (2007). *Numerical computation of internal and external flows* (2nd ed., Vol. 1). Elsevier.

[15] Center, L. R. (2024). The menter shear stress transport turbulence model. *NASA*. https://turbmodels.larc.nasa.gov/sst.html

[16] Molland, A. F., & Turnock, S. R. (2007). Marine rudders and control surfaces. *Butterworth Heinemann*, 21–56. https://doi.org/10.1016/B978-075066944-3/50006-8

[17] Ting, D. S.-K. (2016). Basics of engineering turbulence. *Academic Press*, 119–138. https://doi.org/10.1016/B978-0-12-803970-0.00006-4

[18] Center, G. R. (2025). Reynolds number. *NASA*. https://www.grc.nasa.gov/www/k-12/airplane/reynolds.html

[19] Murad, J. (2018). What is y+ (yplus)? *SimScale*. https://www.simscale.com/forum/t/what-is-y-yplus/82394

[20] Engineering, A. (2016). Boundary layer separation and pressure drag. *AeroSpace Engineering*. https://aerospaceengineeringblog.com/boundary-layer-separation-and-pressure-drag/

[21] Sharma, D. M., & Poddar, K. (2010). Investigations on quasi-steady characteristics for an airfoil oscillating at low reduced frequencies. *International Journal of Aerospace Engineering*, 1687–5966. https://doi.org/10.1155/2010/940528

[22] Cenaero. (2025). High performance computing at cenaero. https://www.cenaero.be

[23] Han, Z.-H., & Zhang, K.-s. (2012). Surrogate-based optimization. *ResearchGate*. https://doi.org/10.5772/36125

[24] Foundation, P. S. (2025). Python. https://www.python.org

[25] GeeksforGeeks. (2025a). Bash scripting – introduction to bash and bash scripting. *GeeksforGeeks*. https://www.geeksforgeeks.org/bash-scripting-introduction-to-bash-and-bash-scripting/

[26] SU2. (2025). Su2: Multiphysics simulation and design software 2025. https://su2code.github.io

[27] Geuzaine, C., & Remacle, J.-F. (2024). Gmsh: A three-dimensional finite element mesh generator with built-in pre- and post-processing facilities. https://gmsh.info

[28] Kitware. (2024). Paraview. https://www.paraview.org

[29] Lintermann, A. (2020). Computational meshing for cfd simulations. *Springer Nature Singapore*. https://doi.org/10.1007/978-981-15-6716-2_6

[30] SimScale. (2024). Mesh quality. *SimScale*. https://www.simscale.com/docs/simulation-setup/meshing/mesh-quality/

[31] GeeksforGeeks. (2025b). Secant method of numerical analysis. *GeeksforGeeks*. https://www.geeksforgeeks.org/secant-method-of-numerical-analysis/

[32] Frey, C., Ashcroft, G., Muller, M., & Wellner, J. (2022). Analysis of turbomachinery averaging techniques. *Proceedings of ASME Turbo Expo 2022*. https://elib.dlr.de/189615/1/v10ct32a039-gt2022-82959.pdf